



Exploração das Membranas Fetais para Aplicações de Engenharia dos Tecidos

BÁRBARA MATOS MACEDO

dezembro de 2022

isep

Instituto Superior de
Engenharia do Porto



Departamento de
Física

Instituto Superior de Engenharia do Porto

P.PORTO

Exploring Fetal Membranes for Tissue Engineering Applications

Bárbara Matos Macedo

Biomedical Engineer from Instituto Superior de Engenharia do Porto

Degree in Biomedical Engineering

“Dissertation presented at the Instituto Superior de Engenharia do Porto to obtain a
Master’s degree in Biomedical Engineering”

Advisor: Cristina Ribeiro

November 2021/22

*“If you can't explain it to a six year old, you don't understand it
yourself.”*

Albert Einstein

Acknowledgments

I would like to thank, first of all, to the Instituto Superior de Engenharia do Porto, and the professors I met on my way, for all the training I received during my degree and master's degree in Biomedical Engineering.

To the Doctor Cristina Ribeiro for the opportunity to carry out this project with her and for the help and support she gave me during this project.

To Institute for Research & Innovation in Health (i3S), for allowing me to carry out this project and providing the necessary conditions and mechanisms for concluding it with success.

To Dr. Cláudia Machado from Histology and Electron Microscopy i3S Scientific Platform for the assistance in the histological analysis of the fetal membranes.

To Dr. Ricardo Silva from Biointerfaces and Nanotechnology i3S Scientific Platform for the assistance in the Zeta Potential and Rheological analysis,

To Eng. Manuela Brás from Bioimaging i3S Scientific Platform for the assistance with the AFM technique.

To Eng. Paula Venda from the Chemistry Department of ISEP for the assistance with the DSC/TGA analysis.

To all the people of the Microenvironment for New Therapies group who helped me whenever I needed.

And last, but not least, to my family, boyfriend, and friends, for all the support and patience they gave me during this great opportunity.

To all, thank you very much.

Resumo

As membranas fetais têm vindo a ganhar destaque na medicina regenerativa devido à sua hipó-imunogenicidade, funções anti-inflamatórias e biocompatibilidade. Estes interessantes materiais naturais, podem ser utilizados como matriz extracelular, uma vez que são ricos em fatores de crescimento e proteínas. A membrana fetal é composta pela membrana coriônica, a camada externa, e pela membrana amniótica, a camada interna, ambas derivadas de tecido extraembrionário. Existe uma terceira camada entre essas duas, a camada esponjosa, cujas características ainda não foram significativamente exploradas.

A descclularização de tecidos e órgãos é uma plataforma tecnológica de sucesso para a criação de materiais de suporte (*scaffolding*). Tem sido sugerido que o sucesso desses materiais após a implantação, é devido aos sinais moleculares fornecidos pelos componentes restantes da matriz extracelular (ECM) apresentados às células *in vivo*, à medida que estas repovoam a superfície dos *scaffolds* descclularizados. Existem vários protocolos descritos na literatura para descclularização de tecidos, sendo que alguns usam compostos tóxicos e de tal forma agressivos que eliminam componentes da membrana que são essenciais para a engenharia de tecidos e aplicações regenerativas.

No decorrer deste trabalho, foi testado um protocolo de descclularização otimizado a partir de um outro já utilizado no grupo. As membranas fetais resultantes foram caracterizadas morfológica e quimicamente através de diferentes técnicas, nomeadamente histologia, espectroscopia de infravermelho com transformada de Fourier (FTIR), calorimetria diferencial de varrimento e termogravimetria (DSC/TGA). A possibilidade de usar a camada esponjosa das membranas fetais como um *scaffold* à base de hidrogel também foi explorada. Para isso, as suas características foram avaliadas usando FTIR, microscopia confocal Raman, microscopia de força atômica (AFM) e testes reológico. O potencial zeta foi também determinado bem como a taxa de hidratação desta membrana.

Os resultados obtidos mostraram que embora o novo protocolo de descclularização tenha eliminado completamente as células da membrana amniótica, algumas células permaneceram na membrana coriônica. Verificou-se também tratar-se de

um protocolo menos agressivo, mantendo a estrutura e composição das membranas descelularizadas mais próxima das membranas nativas.

O presente trabalho permitiu também um avanço na caracterização da camada esponjosa, ainda pouco explorada, tendo em vista a sua possível utilização como um novo hidrogel potencialmente muito interessante para aplicação em medicina regenerativa.

Palavras-chave: Membranas fetais, membrana amniótica, membrana coriônica, camada esponjosa, descelularização, *scaffolds*, hidrogéis.

Abstract

Fetal membranes have been gaining attention for regenerative medicine due to their hypoimmunogenicity, anti-inflammatory functions and biocompatibility. These interesting natural materials can be used as an extracellular matrix once they are rich in growth factors and proteins. The fetal membrane is composed of the chorionic membrane, the outer layer, and the amniotic membrane, the inner layer, both deriving from extra-embryonic tissue. There is a third layer between these two, the spongy layer, which characteristics have not been significantly explored yet.

Decellularization of tissues and organs is a successful platform technology for creating scaffolding materials. It has been suggested that the success of these materials upon implantation is due to the molecular signals provided by the remaining extracellular matrix (ECM) components presented to probing cells *in vivo* as they repopulate the surface. There are several protocols described in the literature for tissue decellularization but some use toxic compounds and are so aggressive, that eliminate membrane components that are essential for tissue engineering and regenerative applications.

In the course of this work, an improved decellularization protocol was tested. The resultant fetal membranes, were morphologically and chemically characterized using different techniques namely histology, Fourier transform infrared spectroscopy (FTIR), differential scanning calorimetry and thermogravimetry (DSC/TGA). The possibility of using the spongy layer as an hydrogel based scaffold was also explored. For this, its characteristics were determined using FTIR, confocal Raman microscopy, atomic force microscopy (AFM), zeta potential and rheological tests. Also, the water swelling ratio of this layer was determined.

The results obtained showed that although the new decellularization protocol completely eliminated cells of the amniotic membrane, some cells remained in the chorionic membrane. It was also verified to be a less aggressive protocol, keeping the structure and composition of the decellularized membranes closer to the native membranes.

The present work also allowed for a breakthrough in the characterization of the spongy layer, still little explored, in view of its possible use as a potentially very

interesting new hydrogel/scaffold for application in regenerative medicine.

Keywords: Fetal membranes, amniotic membrane, chorionic membrane, spongy layer, decellularization, scaffolds, hydrogels.

Index

| | |
|--|------|
| ACKNOWLEDGMENTS | III |
| RESUMO..... | V |
| ABSTRACT | VII |
| INDEX..... | IX |
| FIGURES LIST | XIII |
| TABLES LIST | XVI |
| ABBREVIATIONS LIST..... | XVII |
| 1. INTRODUCTION | 3 |
| 1.1. HOST INSTITUTION..... | 3 |
| 1.2. MOTIVATION AND OBJECTIVES..... | 3 |
| 1.3. DISSERTATION STRUCTURE | 4 |
| 1.4. STATE OF THE ART | 4 |
| 1.4.1. <i>Tissue Engineering</i> | 4 |
| 1.4.2. <i>Hydrogels</i> | 6 |
| 1.4.3. <i>Placenta</i> | 10 |
| 1.4.4. <i>Amniotic Membrane</i> | 12 |
| Amniotic mesenchymal stem cells | 14 |
| Amniotic epithelial cells | 14 |
| Amniotic membrane properties | 15 |
| Applications of AM in regenerative engineering | 17 |
| 1.4.5. <i>Chorionic Membrane</i> | 19 |
| Chorionic membrane properties | 20 |
| Applications of CM in regenerative engineering..... | 22 |
| 1.4.6. <i>Spongy Layer</i> | 24 |
| Applications of mucins in regenerative engineering | 25 |
| 1.4.7. <i>Composition of ECM in each layer of the placenta</i> | 27 |
| 1.5. DECELLULARIZATION PROTOCOLS..... | 28 |

| | | |
|--------|--|----|
| 1.6. | CHARACTERIZATION TECHNIQUES | 34 |
| 1.6.1. | <i>FTIR spectroscopy</i> | 34 |
| 1.6.2. | <i>Differential Scanning Calorimetry/ Thermogravimetry</i> | 36 |
| 1.6.3. | <i>Confocal Raman Microscopy</i> | 36 |
| 1.6.4. | <i>Atomic Force Microscopy</i> | 37 |
| 1.6.5. | <i>Zeta Potential</i> | 39 |
| 1.6.6. | <i>Rheology tests</i> | 39 |
| 2. | MATERIALS AND METHODS | 43 |
| 2.1. | MEMBRANE’S OBTAINING PROCESS | 43 |
| 2.2. | DECELLULARIZATION METHOD..... | 43 |
| 2.3. | MEMBRANE’S LYOPHILIZATION METHOD | 44 |
| 2.4. | MEMBRANE’S STAINING METHODS | 45 |
| 2.4.1. | <i>H&E staining protocol</i> | 45 |
| 2.4.2. | <i>PSR-AB staining protocol</i> | 46 |
| 2.5. | MEMBRANE’S CHARACTERIZATION METHODS | 47 |
| 2.5.1. | <i>Histological analysis</i> | 47 |
| 2.5.2. | <i>FTIR spectroscopy</i> | 47 |
| 2.5.3. | <i>Differential Scanning Calorimetry and Thermogravimetric Analysis</i> | 48 |
| 2.5.4. | <i>Confocal Raman</i> | 48 |
| 2.5.5. | <i>Atomic Force Microscopy</i> | 50 |
| 2.5.6. | <i>Swelling ratio evaluation</i> | 50 |
| 2.5.7. | <i>Zeta Potential</i> | 51 |
| 2.5.8. | <i>Rheological Tests</i> | 51 |
| 3. | RESULTS AND DISCUSSION..... | 55 |
| 3.1. | MEMBRANE’S DECELLULARIZATION RESULTS | 55 |
| 3.1.1. | <i>Histological analysis</i> | 55 |
| | Histological analysis of Amniotic Membrane | 55 |
| | Histological analysis of Chorionic Membrane | 56 |
| | Histological analysis of Spongy layer | 58 |

| | |
|---|-----|
| 3.1.2. <i>FTIR spectroscopy</i> | 59 |
| FTIR spectroscopy of Amniotic Membrane | 60 |
| FTIR spectroscopy of Chorionic Membrane | 65 |
| FTIR spectroscopy of Spongy Layer | 69 |
| 3.1.3. <i>Differential Scanning Calorimetry</i> | 71 |
| DSC/TGA of Amniotic Membrane | 71 |
| DSC/TGA of Chorionic Membrane..... | 73 |
| DSC/TGA of Spongy Layer | 75 |
| 3.1.4. <i>Confocal Raman</i> | 76 |
| 3.1.5. <i>Atomic Force Microscopy</i> | 78 |
| 3.1.6. <i>Swelling ratio evaluation</i> | 81 |
| 3.1.7. <i>Zeta Potential</i> | 81 |
| 3.1.8. <i>Rheological Tests</i> | 82 |
| 4. FINAL CONSIDERATIONS..... | 89 |
| 4.1. GENERAL DISCUSSION..... | 89 |
| 4.2. FUTURE WORK..... | 92 |
| REFERENCES | 93 |
| ANNEX A | 111 |
| ANNEX B..... | 113 |
| ANNEX C..... | 117 |
| ANNEX D | 123 |
| ANNEX E..... | 126 |

Figures List

| | |
|---|----|
| Figure 1.1 – Tissue engineering triad [5]. | 4 |
| Figure 1.2 – Constitution of the human placenta [26]. | 11 |
| Figure 1.3 – Histological structure of human amniotic membrane [32]. | 13 |
| Figure 1.4 – Timeline of AM applications. | 18 |
| Figure 1.5 – Human chorionic membrane: a) schematic image; b) histological image [41]. | 20 |
| Figure 1.6 – Timeline of CM applications. | 24 |
| Figure 1.7 – Timeline of mucin applications. | 27 |
| Figure 2.1 – Thermal analyzer NETZSCH STA 449F3. | 48 |
| Figure 2.2 – Confocal Raman Microscopy: a) Setup of a Confocal Raman Microscope [93]; b) Confocal Raman Microscope LabRAM HR 800. | 49 |
| Figure 2.3 – Zeta Potential: a) Graphical illustration of zeta potential value [137]; b) Electrokinetic analyzer Anton Paar GmbH. | 51 |
| Figure 2.4 – Kinexus Pro rheometer. | 52 |
| Figure 3.1 – FTIR spectra of native membranes. | 60 |
| Figure 3.2 – FTIR spectra of amniotic membrane: AM Native; Amniotic membrane decellularized using improved protocol; Amniotic membrane decellularized using base protocol. | 60 |
| Figure 3.3 – Computational fitting of the amide I FTIR spectroscopy absorption band: a) AM Native; b) AM. DC. Base Protocol; c) AM. DC. Improved protocol. | 64 |
| Figure 3.4 – FTIR spectra of chorionic membrane: CM Native; Chorionic membrane decellularized by improved protocol; Chorionic membrane decellularized by base protocol. | 65 |
| Figure 3.5 – Computational fitting of the amide I FTIR spectroscopy absorption band: a) CM Native; b) CM. DC. Base Protocol; c) CM. DC. Improved protocol. | 68 |
| Figure 3.6 – FTIR spectra of spongy layer: SL Native; spongy layer decellularized by base protocol. | 69 |
| Figure 3.7 – Computational fitting of the amide I FTIR spectroscopy absorption band: a) SL Native; b) SL. DC. Base Protocol. | 71 |

| | |
|---|----|
| Figure 3.8 – Confocal Raman spectra of Native Spongy Layer and Spongy Layer decellularized by base protocol. | 77 |
| Figure 3.9 – AFM 3D and 2D images of the Spongy Layer topography: native membrane (a and b) and decellularized by the base protocol (c and d)..... | 79 |
| Figure 3.10 – Graph of Amplitude Sweep comparing 3 samples of the Native Spongy Layer..... | 83 |
| Figure 3.11 – Graph of Frequency Sweep comparing 2 samples of the Native Spongy Layer..... | 84 |
| Figure 3.12 – Graph of Amplitude Sweep comparing 3 samples of the Decellularized Spongy Layer. | 85 |
| Figure 3.13 – Graph of Frequency Sweep comparing 2 samples of the Decellularized Spongy Layer. | 86 |

Tables List

| | |
|---|-----|
| Table 1.1 – Summary of <i>ECM Composition</i> on each layer of placenta..... | 28 |
| Table 1.2 – Comparison between decellularization protocols. | 29 |
| Table 3.1 – Micrographic images of stained Amniotic membranes. | 55 |
| Table 3.2 – Micrographic images of stained Chorionic membranes. | 57 |
| Table 3.3 – Micrographic images of stained Spongy Layer membrane. | 58 |
| Table 3.4 – Assignment of each peak in the FTIR spectrum of Native Amniotic Membrane..... | 63 |
| Table 3.5 – Characteristic protein secondary structure amide I bands of Amniotic Membranes. | 65 |
| Table 3.6 – Assignment of each peak in the FTIR spectrum of Native Chorionic Membrane..... | 66 |
| Table 3.7 – Characteristic protein secondary structure amide I bands of Chorionic Membrane..... | 68 |
| Table 3.8 – Assignment of each peak in the FTIR graph of Native Spongy Layer..... | 70 |
| Table 3.9 – Characteristic protein secondary structure amide I bands of Spongy Layer membrane..... | 71 |
| Table 3.10 – Thermograms of AM obtained through two different protocols. . | 72 |
| Table 3.11 – Thermograms of CM obtained through two different protocols... | 74 |
| Table 3.12 – Thermograms of SL obtained through two different protocols. ... | 75 |
| Table 3.13 – Assignment of each peak in the Confocal Raman graph of Native Spongy Layer..... | 77 |
| Table 3.14 – Parameters of the surface roughness of the analyzed samples. | 80 |
| Table 3.15 – Swelling ratio of Spongy layer. | 81 |
| Table 3.16 – Zeta Potential of Spongy Layer. | 81 |
| Table B.0.1 – Microscopy images of stained amniotic membranes. | 113 |
| Table B.0.2 – Microscopy images of stained chorionic membrane..... | 114 |
| Table B.0.3 – Microscopy images of stained spongy layer. | 115 |
| Table C.0.1 – FTIR spectra of the fetal membranes..... | 117 |
| Table E.0.1 – AFM images of Spongy Layer topography..... | 126 |

Abbreviations List

- AECs – Amniotic epithelial cells
- AFM – Atomic Force Microscopy
- AM – Amniotic Membrane
- AMSCs – Amniotic mesenchymal stem cells
- APCs – Antigen presenting cells
- ATR – Attenuated Total Reflection
- bFGF – Basic fibroblast growth factor
- CDKs – Cyclin-dependent kinases
- CHSJ – Centro Hospitalar S. João
- CM – Chorionic Membrane
- DC – Decellularized
- dH₂O – Distilled water
- DMSO – Dimethyl sulfoxide
- DNA – Deoxyribonucleic acid
- DSC – Differential Exploratory Calorimetry
- ECM – Extracellular matrix
- EGF – Epidermal growth factor
- EtOH – Ethanol
- FTIR – Fourier transform infrared spectroscopy
- GAG's – Glycosaminoglycans
- HA – Hydroxyapatite
- hCG – Human chorionic gonadotropin
- HGF – Hepatocyte growth factor

HLA – Human leukocyte antigen

IDO – Indoleamine-2,3-dioxygenase

IGF-1 – Insulin-like Growth Factor 1

IL-1 – Interleukin 1

IL-10 – Interleukin 10

IL-11 – Interleukin 11

IL-6 – Interleukin 6

IL-8 – Interleukin 8

INEB – Instituto Nacional de Engenharia Biomédica

INP – Interpenetrating

ISEP – Instituto Superior de Engenharia do Porto

MHC1 – Major histocompatibility complex class I

MSCs – Mesenchymal stem cells

NK – Natural killer

PBS – Phosphate buffered saline

PDGF – Platelet-derived growth factor

PDGF-BB – Platelet derived growth factor BB

PEDF – Pigment epithelium-derived factor

PFA – Paraformaldehyde

PGA – Polyglycolic acid

PIGF – Placental growth factor

PLGA – Poly-dl-lactic-co-glycolic acid

PLLA – Poly-l-lactic acid

PS – Polystyrene

SDS – Sodium dodecyl sulfate

SL – Spongy Layer

TCP – Tricalcium phosphate

TE – Tissue Engineering

TGA – Thermogravimetric

TGF- β – Transforming growth factor beta

TGF- β 1 – Transforming growth factor beta 1

TIMP-1 – Tissue inhibitor of metalloproteinase 1

TIMP-2 – Tissue inhibitor of metalloproteinase 2

TIMP-3 – Tissue inhibitor of metalloproteinase 3

TIMP-4 – Tissue inhibitor of metalloproteinase 4

VEGF – Vascular endothelial growth factor

VM – Virtual Membrane

CHAPTER 1 – INTRODUCTION

1. Introduction

1.1. Host institution

This research work, from the curricular unit Thesis of the Master's Degree in Biomedical Engineering, was developed at Instituto Nacional de Engenharia Biomédica/Instituto de Investigação e Inovação em Saúde (INEB/i3S), on the Microenvironments for New Therapies group. The i3S Association merges three institutes (INEB, IBMC, Ipatimup) and researchers from several schools of the UPorto, thus consolidating an extensive collaboration between all institutions spanning many years. The transdisciplinary character of i3S is achieved through Integrative Research Programs and by promoting projects addressing questions that require participation of basic and applied sciences.

1.2. Motivation and Objectives

Decellularized (DC) extracellular matrices (ECM) scaffolds can be successfully used in a variety of different applications namely, the generation of ECM hydrogels, the recellularization of acellular organs as well as applications in tissue engineering and regenerative medicine. The decellularization methods used vary as widely as the tissues and organs of interest and the efficiency of cell removal is dependent on the origin of the tissue and the specific physical, chemical, and enzymatic methods that are used. Each of these treatments affect the biochemical composition, tissue ultrastructure, and mechanical behavior of the remaining ECM scaffold, which in turn, affect the host response to the material. One of the major objectives of the present work was to evaluate the efficacy of an optimized decellularization protocol developed in our group, minimizing the use of toxic compounds.

The placenta is made up of the amniotic membrane and the chorionic membrane [1], and joining these two membranes is spongy layer (SL), that is part of the amniotic membrane [1]–[3]. Spongy layer is normally discarded in fetal membranes preparation although it presents a very interesting composition. Another main motivation of this work was to characterize and explore the potential of this type of matrix in the creation of scaffolds and hydrogels for regenerative engineering.

Different techniques were used throughout this work namely histology, Fourier transform infrared spectroscopy (FTIR), differential scanning calorimetry and thermogravimetry (DSC/TGA), confocal Raman, atomic force microscopy (AFM) and zeta potential tests. Rheology studies were also performed in order to mechanically characterize the spongy layer.

1.3. Dissertation Structure

This report is compartmentalized in 4 chapters. The first chapter, Introduction, describes the main motivations and objectives behind the choice and realization of the chosen theme, presents the state of the art of the thematic and addresses the characterization techniques used throughout the work. In the second chapter, the materials and methods used are described. In the third chapter, the results obtained are described and discussed. In the last chapter, chapter 4, the most relevant conclusions are highlighted as well as the perspectives of future work.

1.4. State of The Art

1.4.1. Tissue Engineering

Tissue engineering (TE) has been defined as an interdisciplinary field that applies the principles of engineering and the life sciences toward the development of biological substitutes that restore, maintain, or improve tissue function [4]. Cells, scaffolds and growth-stimulating signals are generally referred to as the tissue engineering triad, the key components of engineered tissues **Figure 1.1**.

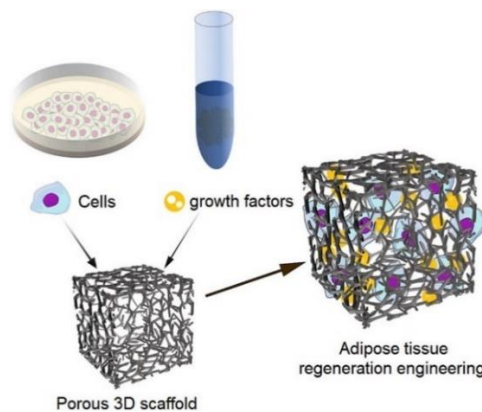


Figure 1.1 – Tissue engineering triad [5].

Intuitively, the best scaffold for an engineered tissue should be the extra cellular matrix of the target tissue in its native state. Nevertheless, the multiple functions, the complex composition and the dynamic nature of ECM in native tissues make it difficult to mimic exactly. Therefore, contemporary concept of scaffolding in tissue engineering is to mimic the functions of native ECM, at least partially.

Scaffolds need to have certain characteristics, according to the type of tissue that were designed for. Therefore, a scaffold must be [6]–[8]:

- **Biocompatible** – allowing cells to interact with it in a positive way, increase their adhesion, growth, proliferation, and differentiation. It cannot be toxic to the tissue where it will be implanted, being the immune response of the body the minimal as possible.
- **Biodegradable** – body cells must, over time, replace the scaffold, and create their own ECM, so the degradation rate of the scaffold must be compatible with the rate of new tissue formation.

It should also present:

- **Adequate mechanical properties** – it must be able to mimic the mechanical properties of the tissue it is replacing, having to maintain the structure of the tissue until it regenerates completely.
- **Adequate architecture** – it must be sufficiently porous, allowing the entry of cells and the penetration of the necessary nutrients, and the porous must have a certain size, which will vary according to the tissue, allowing arterial revascularization.

In order for the scaffold to adapt to the tissue for which it was designed, it is essential to choose the type of biomaterial that will be used for its creation [7]. Natural and synthetic scaffolds have different physical and chemical characteristics [6].

Many types of biomaterials can be used to make porous scaffolds for tissue engineering provided that a fabrication technology compatible with the biomaterial properties is available.

Typically, scaffolds are created using three types of biomaterials, which have both advantages and disadvantages [7]:

- **Ceramics** – the most used ceramic biomaterials are Hydroxyapatite (HA) and Tricalcium Phosphate (TCP). These types of biomaterials have the advantages of being bioactive, having high rigidity, a hard and brittle surface and low elasticity. However, they have limited applicability due to their fragility and complexity in its modeling.
- **Synthetic polymers** – the most used are polystyrene (PS), Poly-l-lactic acid (PLLA), Polyglycolic acid (PGA) and Poly-dl-lactic-co-glycolic acid (PLGA). These types of biomaterials present the advantage that they can be created with desired characteristics. However, there is a risk that the organism will reject this type of biomaterial, as they have a reduced bioactivity, and the production of carbon dioxide when degraded, will cause the pH drop in the surrounding tissues which may result in their necrosis.
- **Natural polymers** – such as collagen, proteoglycans, chitosan, and alginate. These biomaterials are bioactive, promote good cell growth and adhesion, and they are biodegradable. However, they present poor mechanical properties, when it comes to orthopedic applications where load support is required. Additionally, their structures are not completely reproducible and homogeneous.

Nowadays, scaffolds based on decellularized organs and tissues are being quite explored. This type of biomaterial has the same advantages as natural polymers, but to avoid them from being rejected, triggering an immune response by the organism where they will be implanted, it is necessary that they go through a decellularization process, eliminating all types of cellular and nuclear material [9].

1.4.2. Hydrogels

The hydrogel concept first emerged in 1960, with a publication of a research paper by Wichterle and Lim [10], [11] and since then this concept has remained unchanged [11]. Hydrogels are materials constituted by a hydrophilic three-dimensional polymeric

network [10]–[13], natural or synthetic [12]. Due to their composition, hydrogels are materials that have the ability to absorb large amounts of water within their structure [10], [12], [13] preserving their original shape and without dissolving [13]. The ability to retain aqueous liquids in its three-dimensional structure can exceed 1000% of its dry weight [10]. Hydrogels can be created *in situ* or *in vitro* and can be injectable or implantable [11].

Hydrogels can be classified according to their generation or according to their characteristics. Within the classification of hydrogels according to their generation we have [11]:

- **First generation hydrogels** – first generation hydrogels are formed by simple polymeric networks that were achieved through the formation of chemical bonds. These were created to be used in drug delivery or in ophthalmology;
- **Second generation hydrogels** – emerged approximately in the seventies, with the establishment of ionic and hydrophobic interactions (physical interactions). They are distinguished from the first generation by responding to specific chemical, physical or biochemical stimuli. The fact that they respond to stimuli makes them more beneficial, as they can be used in a very particular place where the release of a drug or formation of a gel may be necessary;
- **Third-generation hydrogels** – around 1990, third-generation hydrogels appeared, achieved through distinct physical interactions, such as the generation of metal-ligand coordination complexes and creation of inclusion complexes, supramolecular chemistry. These were created to improve the degradation, mechanical and thermal properties, in addition to the eventuality of their formation *in situ*.

Based on their characteristics, we can classify hydrogels according to their structure, degradability, source, ionic charge, response to stimuli, type of crosslinking and polymeric composition. Of these, the most significant classifications are the last three mentioned [11]. They can be classified according to:

- **Their polymeric composition** – in this classification are included homopolymeric, copolymeric, interpenetrating (INP) polymeric network and semi-INP hydrogels. Homopolymers are made up of a polymeric network composed of a single type of hydrophilic monomer. Copolymeric are made up of more than one type of monomer, with at least one hydrophilic component, and are arranged randomly, in blocks or alternating. The INP polymer network is composed of the combination of two or more polymers, its formation occurs by crosslinking one polymer to another that is already crosslinked, noting that each network consists of a single species of polymer. Finally, in the semi-INP polymer network, its composition is the same as the INP polymer network, but one of the polymers that constitutes it is crosslinked while the other is linear [10], [11].
- **Type of crosslinking** – hydrogel chains are formed through crosslinking, covalent bonds, which, depending on the crosslinking type, can be divided into chemical or permanent hydrogels and physical or reversible hydrogels. Chemical hydrogels are formed through chemical bonds, covalent bonds. Physical hydrogens are formed through physical interactions such as hydrogen bonds, Van der Waals interactions, hydrophobic interactions, creation of metal-ligand coordination complexes, ionic bonds and generation of inclusion complexes (supramolecular chemistry) and electrostatic interactions [10]–[13].
- **Their response to stimuli** – these are characterized by undergoing transformations in response to changes in the environment where they are, therefore, they respond to stimuli, which can be chemical (appearance of specific molecules or the variation of their concentration and temperature), physical (presence of magnetic or electric field, light and pressure) or biochemical (existence of enzymes or antigens). Through these changes in their environment, hydrogels respond through changes in the structure of their network, level of water retention or resistance [11].

We can also classify hydrogels according to the nature of their monomers [14] as natural, synthetic and hybrid [14], [15]:

- **Natural hydrogels** – they are made up of natural polymers. This type of polymer has the main advantage of its similarity with the organic constituents [11], [14], so that when they are recognized by the cells of the host organism, resulting in positive cell interactions [11]. Their main disadvantage are being difficult to control their properties, they can potentially trigger an immune response and the fact that their composition can vary from between different batches [14];
- **Synthetic hydrogels** – they are made up of synthetic polymers, with the great advantage of being obtained through controllable chemical processes [11], allowing large-scale production with a high degree of uniformity between batches. They also allow the modeling of some desirable characteristics, such as the mechanical properties of the network formed or the degradability of the product, according to the function for which it was created [11], [14];
- **Hybrid hydrogels** – are made up of a combination of natural polymers with synthetic polymers [16] resulting in mixed properties such as greater hydrophilicity of the chains and greater strength of the material [17].

Hydrogels exhibit a high interest as biomaterials [12], due to their porous structure, similarity of their physical properties to those of living tissues, such as low surface tension, high water content and elastic and soft consistency [10], [12]. These characteristics make hydrogels an ideal environment for cellular growth and adhesion, in addition to their porous structure enabling the vascularization of new tissues [10].

In light of what was mentioned in the previous paragraph, hydrogels have helped progress in a variety of medical applications, such as scaffolds to be used in tissue engineering [10], [12], hemodialysis membranes, vascular grafts [12], controlled drug delivery systems [10]–[12], manufacture of contact lenses [11], [12] and wound dressings and protein fixation [12]. Hydrogels, due to their flexibility, biocompatibility and similarity to extracellular matrix, are a good medium for the delivery and culture of fibroblasts and keratinocytes [2].

Studies have been done on the creation of hydrogels derived from amniotic membranes (AM). Hydrogels produced with AM have the ability to preserve normal cell adhesion, proliferation and migration [2]. The formation of hydrogels with physiological and mechanical properties related to cell culture can be obtained through the digestion of decellularized tissues, such as an example the amniotic membrane (amnion), with pepsin [18]. A bioactive hydrogel with ECM of the amnion was created to be used in cell delivery and tissue engineering [2]. Ryzhuk *et al.* produced a hydrogel made of decellularized amnion suitable for culturing commonly used cell lines, C2C12 and SH-SY5Y, as well as for culturing placenta-derived mesenchymal stem cells (MSCs) and bone marrow-derived MSCs [19]. Murphy *et al.* created a hydrogel of hyaluronic acid combined with AM, which had growth factors and cell-derived cytokines in its composition. The dermal keratinocytes and fibroblasts present in the hydrogel made it possible to accelerate re-epithelialization and wound healing procedures, with aesthetic results, and greater cell viability and proliferation [2], [20].

Despite the several existing studies of the use of the amniotic membrane in clinical applications, the chorionic membrane (chorion) has only recently begun to be studied for its possible use in clinical applications [21]. Francis *et al.* (2017) demonstrated, through animal studies, that a hydrogel produced with human chorion was able to reduce scarring after myocardial ischemia and also showed, in *in vitro* studies, that they produce beneficial effects on stem cells, cardiomyocytes and endothelial cells [22].

1.4.3. Placenta

The human placenta, formed from the trophoblast and extraembryonic mesoderm during the development of the embryo [23], is an embryonic attachment that plays an essential and irreplaceable role in the development of the fetus during the gestation period. It is through this structure that the physiological exchanges of nutrients, gases and metabolites take place between the fetus and the mother during its development [23], [24], also having the function of producing hormones, such as progesterone, estrogen, human

chorionic thyrotropin, human chorionic gonadotropin (hCG), human chorionic corticotropin and even human placental lactogen and enzymes [25].

This specific organ of the gestation period is fully formed at the end of the fourth month of gestation [23], it has a round or ovulated configuration, with a weight that can vary from 300 to 600 g, a thickness that varies from 1.5 to 3 cm and a diameter of 15 to 20 cm [23]–[25].

The placenta, **Figure 1.2**, is made up of different types of membranes, among them we have the amniotic membrane and the chorionic membrane [1] that constitute the fetal portion and still a maternal portion, constituted by the basal decidua [23], [24]. The amniotic membrane is the innermost membrane, which delimits the place where the fetus develops in contact with the amniotic fluid. The chorionic membrane, the outermost membrane, is attached to the amniotic membrane. The junction of these two membranes, form the chorioamniotic membrane [25] or chorionic plate [23].

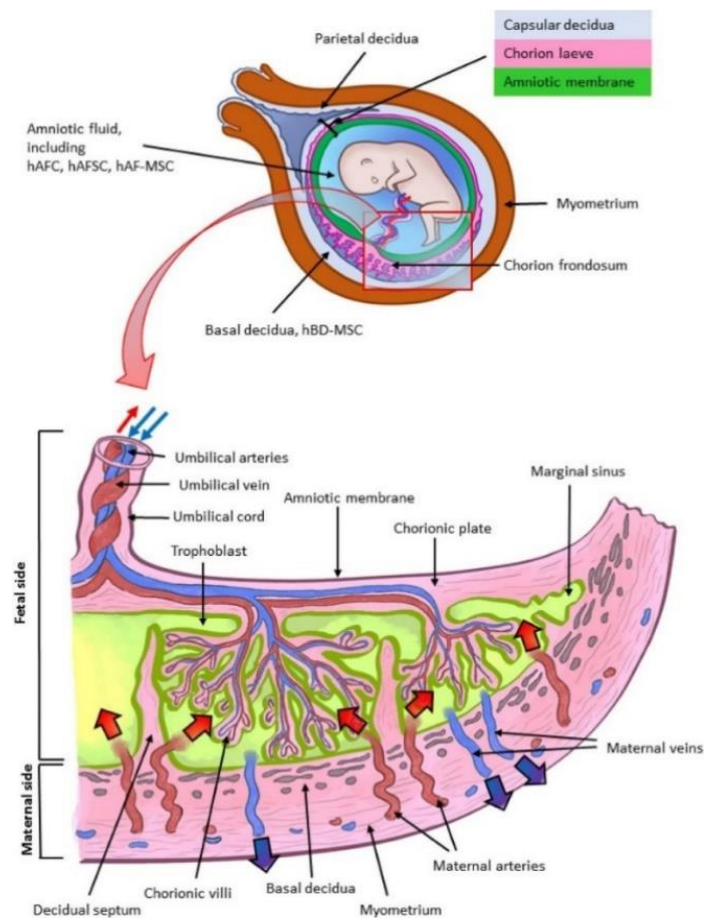


Figure 1.2 – Constitution of the human placenta [26].

In addition to the amnion and chorion, the umbilical cord is also derived from the fetal portion. The membranes that constitute the fetal portion have been subject to rigorous investigation as they are potential source of MSCs, which can be used in clinical applications [3]. The placenta presents in its extracellular matrix components such as collagen types I and IV, fibrillin, laminin and fibronectin [24], which are the basis for the production of scaffolds [6], [27].

The amniotic and chorionic membranes, present the essential properties to be used in the production of natural scaffolds. Therefore, they are one of the most commonly used biomaterials and allografts in regenerative medicine and tissue engineering [28]. Because they are considered biological waste, which are rejected at birth, their use in tissue engineering and regenerative medicine is ethically acceptable. It is also a material that is easy to obtain, with authorization from the parents for its use, and with practically unlimited availability [29].

1.4.4. Amniotic Membrane

As mentioned previously, the AM is the layer of the placenta that is closest to the fetus, surrounding the fetus during its development. Between the fetus and the AM is the amniotic fluid [2], [3], [24], [30], [31] which plays a preponderant role on the protection of the fetus and helps on its nourish through diffusion [2], [3]. AM is a thin tissue from the trophoblast [3], which appears between the 7th and 8th day after fertilization [24]. Its thickness can vary from 0.02 mm to 0.5 mm thick, depending on the amount of mucins and amniotic fluid present [24], [30].

The amnion is a thin, translucent membrane made up by 5 types of layers (**Figure 1.3**) among which 3 are histologically distinct, in particular epithelial layer, basal layer and mesenchymal layer. The last one can be separated into 3 sublayers: the compact layer, fibroblast layer and spongy layer [1]–[3] AM doesn't exhibit direct blood supply or vascularization [24] and each type of layer that constitutes it has different cell types, making it a good skin substitute. Of the cell types that constitute the membrane, amniotic mesenchymal stem cells (AMSCs) and amniotic epithelial cells (AECs) stand out, which are responsible for creating the ECM, growth factors and even several types of cytokines [2].

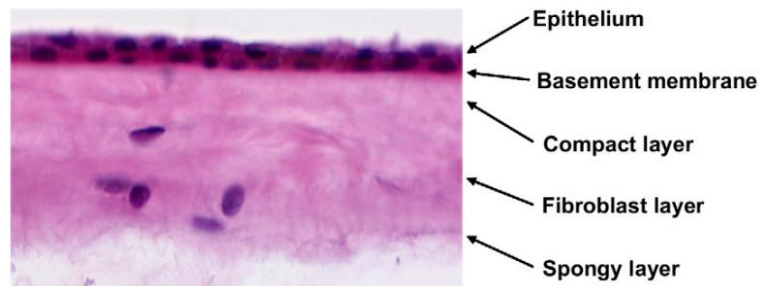


Figure 1.3 – Histological structure of human amniotic membrane [32].

The epithelial layer is the innermost layer of the AM, constituted by a single layer of columnar epithelial cells originating from the ectoderm, the AECs [1], [3], [24]. The basement membrane that constitutes the amnion, is one of the thickest basement membranes discovered in the human body, it is made up of several types of collagen (type I, III, IV, V, VI and VII), laminin, fibronectin, elastin, nidogen and other types of integrins [1], [24], [33]. This membrane is capable of promoting the healing process, fibrosis and neovascularization [24]. The compact layer is an acellular layer composed, only by reticular fibers [1] although occasionally we may also find macrophages (Hofbauer cells), particularly if they are actively phagocytic [34]. The fibroblast layer, which is a reticular network that includes some casual fibroblasts [1], proteoglycans and non-collagenous glycoproteins [33], presents AMSCs, cells derived from embryonic mesoderm, type I and III collagens, which maintain its structural integrity [3], and also contains Hofbauer cells [34]. Finally, the spongy layer is composed by a network of fine fibrils that are surrounded by mucus [1]. Glycoproteins and proteoglycans are found in abundance in this layer, mainly hyaluronic acid and also contains a non-fibrillar collagen type III network [3], [35], some isolated fibroblast and Hofbauer cells [34].

AM is one of the most used biological scaffolds, being applied as a biomaterial for surgical reconstructions for about 100 years [24]. Its high use is due to the basement membrane that has re-epithelialization characteristics [2]. Amnion possesses the ability of cell regeneration and proliferation [31], as well as having antimicrobial properties, capable of decreasing the bacterial load and facilitating the treatment of infected wounds, reducing scar inflammation and improving wound healing [24], due to the growth factors it contains. In addition to these characteristics, the fact that this membrane includes in its

composition components such as collagen, laminin, elastin and fibronectin, makes it an excellent scaffold for tissue engineering [31].

Amniotic mesenchymal stem cells

AMSCs make up a layer of cells where we can find amniotic mesenchymal stromal cells and also mature mesenchymal fibroblasts. Amniotic mesenchymal stromal cells express, on their cell surface, pluripotency markers such as SSEA-1, SSEA-3, SSEA-4, SOX-2, REX-1, OCT-3, OCT-4, KLF4 (Krüppel-like factor 4) and Nanog. Both cell types that are present in the AMSCs layer present on their cell surface the epidermal growth Factor (EGF) receptor, CD29, CD44, CD73, CD90, CD105. About 10% of mature mesenchymal fibroblasts express, as well as amniotic mesenchymal stromal cells, SSEA-1, SSEA-3, CD117, CD133, CD146, CD201 and Globo H. Less than 15% of fibroblasts express SSEA-4, while 35% of cells express Nanog and 45% express OCT-3 and OCT-4 [30].

AMSCs are able to promote angiogenesis with the expression of proangiogenic factors, suspend the innate and adaptive immune systems and also have the capacity for trilineage cell differentiation [3].

Amniotic epithelial cells

AECs are cuboidal cells derived from the epiblast, being created on the eighth day of gestation. These cells build a monolayer on the basal lamina and are in contact with the amniotic fluid. They express on their cell surface many types of growth factors, such as hepatocyte growth factor (HGF), keratinocyte growth factor, EGF and basic fibroblast growth factor (bFGF). They also express different types of antigens, such as E-cadherin, STRO-1, integrins such as $\alpha 6$ and $\beta 1$, c-met protein, ATP-binding transporters G2 and CD10, CD13, CD24, CD29, CD44, CD49e, CD73, CD90, CD105 and CD166. The AECs also express pluripotent markers such as SSEA-4, stage 4 specific embryonic antigen [3], [30].

Amniotic membrane properties

AM has some properties that make it a good choice to be used in regenerative engineering, such as [1]–[3], [24], [29], [30]:

- **Angiogenic and Antiangiogenic Properties** – this membrane can either promote angiogenesis or inhibit it, i.e., as reported by Niknejad *et al.* the epithelial side of AM prevents angiogenesis, in turn, the mesenchymal side of AM increases angiogenesis, having to pay close attention to membrane orientation when incorporating it as a graft into a host, to accomplish the intended purpose. This ability to promote angiogenesis as well as inhibit it is related to the fact that amnion can excrete some of the factors that promote angiogenesis such as: EGF, platelet-derived growth factor (PDGF), interleukin 6 (IL-6), interleukin 8 (IL-8), vascular endothelial growth factor (VEGF), angiopoietin- 2, bFGF and HGF. Some of the factors that are expressed by this membrane, capable of inhibiting angiogenesis are: tissue inhibitor of metalloproteinase 1 (TIMP-1), tissue inhibitor of metalloproteinase 2 (TIMP-2), tissue inhibitor of metalloproteinase 3 (TIMP-3), tissue inhibitor of metalloproteinase 4 (TIMP-4), pigment epithelium-derived factor (PEDF) and thrombospondin-1.
- **Low Immunogenicity** – the low immunogenicity is caused by the low expression of a certain type of molecules by the AECs and AMSCs present in this membrane, in which they show low levels of molecules present in the major histocompatibility complex class I (MHC1), such as human leukocyte antigen (HLA) which ranges from antigens Ia, HLA-A, B and C, to antigens Ib, HLA-G and E, in addition to these HLA, they also express at almost zero levels, HLA class II molecules, such as HLA-DP, DQ and DR, and CD80 and CD86, costimulatory molecules. The null or low expression of these molecules makes the possibility of transplant rejection very small.
- **Antifibrotic Properties** – through the secretion of TIMP-1, TIMP-2, TIMP-3 and TIMP-4, by the amnion, the risk of scar formation and

adhesion is reduced, because these factors restrict the activity of proteases in the place where the graft is applied. The anti-scar action of amnion is due to its anti-inflammatory action caused by the inhibition of interleukin 1 (IL-1), IL-6, IL-8 and inflammatory cells.

- **Anticancer Properties and Nontumorigenicity** – the cells present in the amnion, AECS and AMSCs, have the ability to provoke apoptosis in several types of cell lines, such as the MDA-MB-231 cell line present in breast cancer and the HeLa cell line of cervical cancer. It was proven by Magati *et al.* that AMSCs cause cell cycle interruption of hematopoietic and nonhematopoietic cancer cells in coculture through the inhibition of positive regulators present in the cell cycle, such as cyclin-dependent kinases (CDKs), cyclins, among others, as well as through upregulation of cell cycle inhibitors such as CDK inhibitor N2B or cyclin G2. The cell cycle of cancer cells can be interrupted in the G0/G1 phase, preventing their progression to the next phase, S phase, through the down regulation of the retinoblastoma-like 1 and cullin-1 proteins, and the up regulation of the retinoblastoma protein.
- **Anti-inflammatory Properties** – Anti-inflammatory factors such as the enzyme indoleamine-2,3-dioxygenase (IDO), hyaluronic acid, HGF, transforming growth factor beta (TGF- β), prostaglandin E2 and interleukin 10 (IL-10) are produced in AM, restricting the manifestation of inflammatory cytokines of helper cells type 1, Th1. The amnion cells themselves presents anti-inflammatory properties: they cancel the proliferation of T lymphocytes, difficult the maturation of monocytes into dendritic cells and affect antigen Presenting Cells (APCs) and natural killer (NK) cells.
- **Antimicrobial Properties** – amnion has antimicrobial activity *in vivo*, as AEC cells manifest natural antimicrobials, such as elafin and human β -defensins, as reported by King *et al.* and Buhimschi *et al.*

- **Antiviral Properties** – antiviral activity is observed in AM, because the complementary deoxyribonucleic acid (DNA) for cystatin E was discovered in AECs.
- **Promotion of Epithelialization** – epithelialization is essential for tissue healing and regeneration. This is achieved through the release of factors such as insulin-like growth factor 1 (IGF-1), bFGF, TGF- β , PDGF, EGF, HGF and IL-8, as well as some factors that support differentiation of different cells and epithelialization. Molecules such as laminin-1 and -5, fibronectin and collagen, types I, III, IV and VII, which are present in the extracellular matrix of AM also can facilitate cell migration and adhesion.
- **Analgesic and pain reducing properties** – was reported by Ravishanker *et al.* that, bandages made through AM offer, soon after its use in the injured region, a significant reduction in pain as opposed to traditional bandages. This characteristic of the amnion is related to its protective effect on the nerve endings in the injured region, which makes this region safe from bacterial infections. As there is no need to change the bandages so many times, like the traditional ones, it allows the region not to be so inflamed and still allows the skin to be hydrated.

Applications of AM in regenerative engineering

Amnion was first used in Traditional Chinese Medicine. In 1910 it was used by Davis in a skin transplant, functioning as a surgical material to treat skin burns. Three years later, Sabella reports the fresh use of AM to treat skin ulcerations and burns [1], [24], [36]. In 1940, Roth reports the use of AM transplantation for the correction of conjunctival and symblepharon imperfections. Sorby and Symons, in 1946, reported the use of this membrane to treat acute chemical burns [24]. In addition to these applications, amnion is used in the reconstruction of tympanoplasty, bladder, oral cavity, arthroplasty, biological bandage in the treatment of burns and skin wounds caused by acids, bedsores and ulcers, to restore soft tissue, to prevent tissue adhesion during surgeries of the abdomen, larynx, head, vagina and pelvis, and has been widely used in ophthalmology [1], [24], [29], [36]. Its wide use is also due to the fact that it can be applied to irregular areas of the human body such as the face, hands, through its ability to adhere to the injured

region. When the lesion begins to heal and gain new epithelium beneath the membrane, it begins to detach from the lesion [24]. Its use has also been described in dentistry for covering gingival recession, ridge preservation, healing periodontal bone defects and furcation defects and to reconstruct the tooth inclusion device through endodontic surgery guided tissue regeneration [31].

It has also been discovered that amnion, in tissue engineering, can serve as a cell delivery vehicle [31] and even as a scaffold for human cell culture [24], due to its enriched extracellular matrix and the presence of growth factors [2]. In 2008, Wilshaw *et al.*, by sterilizing AM with peracetic acid, proved that it was biologically compatible with the adhesion and proliferation of human fibroblasts and keratinocytes [24], and could be used as a scaffold for stem cell differentiation and proliferation [2]. Yang *et al.*, in 2009, described that cryopreserved amnion, without the presence of collagen matrices, functioned, for cell culture, as a scaffold of both fibroblasts and keratinocytes and noted that human fibroblasts migrated to the amnion and after three days produced an equivalent skin model, when the stromal zone was fertilized facing the bottle [24]. We can also use the amniotic membrane to form a hydrogel which is a good vehicle for delivery and culture of fibroblasts and keratinocytes [2].

Although the use of this membrane has several advantages, for some years it was no longer used due to the risk of infection caused by placentas collected through normal deliveries and without being serologically tested at the time of collection. Today, placentas are collected in cesarean deliveries, where they can be frozen, serologically tested and sterilized by different types of methods [36].

The timeline of these applications is shown on the next figure, **Figure 1.4**.

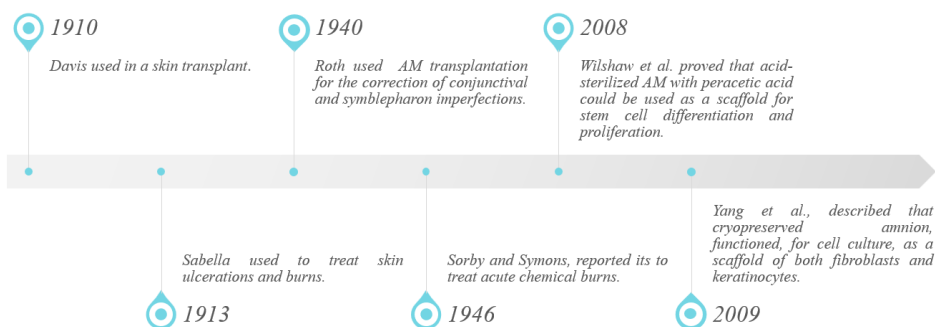


Figure 1.4 – Timeline of AM applications.

1.4.5. Chorionic Membrane

The chorion is the placental membrane that is furthest away from the fetus, it is the outermost layer of the placenta [3], [34]. The innermost layer of the Chorionic membrane (CM) is in contact with the amnion and its outermost layer with the maternal decidua [34]. This membrane is about 3 to 4 times thicker than the amniotic membrane [37] and in opposition to the amnion, a part of the chorion is vascular and has mononuclear trophoblasts [38].

It is an extraembryonic membrane that is formed from a combination of tissues from the cytotrophoblast, syncytiotrophoblast and extraembryonic mesoderm during the blastocyst implantation in the uterine endometrium, which in turn gives rise to the wall of the chorionic sac that will envelop the embryo and the remaining membranes [38], [39]. From the end of the 2nd week of gestation, villi begin to form throughout the membrane, which remain until the beginning of the 8th week of gestation. During the development of the chorionic sac and the embryo, only the villi that are related to the decidua basalis are preserved, constituting the fetal portion of the placenta, the villous chorion. In this region of the chorion, its villi branch, increase in number and become vascularized [39]. Therefore, from the 8th week, the chorion can be divided into villous/leaf chorion and smooth/leave chorion, which is adjacent to the amnion [25]. The chorion leave is an opaque, avascular membrane with obliterated or phantom villi, so called because of its atrophy [33], [34], [40].

Like the amnion, the chorion is composed of layers of epithelial and connective tissue. Its layers are inverted in orientation, more cellular and less organized in relation to the amnion layers [33].

Schwarzfurtner *et al.* reported that the chorion and amnion have the same collagen content and, although the chorion is thicker than the amnion, it has lower tensile strength and viscoelasticity compared to the amnion. This may be a result of their rare cross-connections of fibril bundles and their looser structure [33].

The chorion is composed of 4 different layers (cell layer, reticular layer, basement membrane, and trophoblastic layer) and two types of cells, mesenchymal cells and trophoblastic cells, **Figure 1.5** [25], [33], [34].

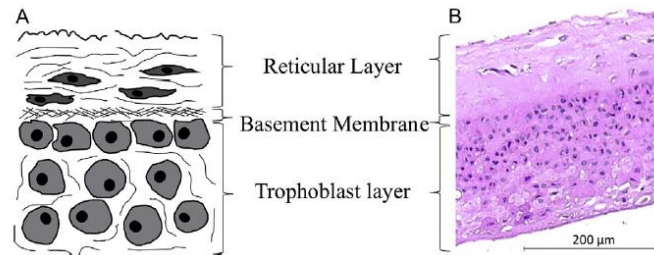


Figure 1.5 – Human chorionic membrane: a) schematic image; b) histological image [41].

The order of the 4 layers of the chorion is cell layer, reticular layer, basement membrane and trophoblastic layer, the latter being on the external side of the chorion, connected to the maternal decidua [34], [37], [42]. The cell layer, often absent, **Figure 1.5**, or imperfect in the chorion, is a thin layer formed by a network of intertwined fibroblasts [34], [40], [42] and Hofbauer cells [34]. The reticular layer is the thickest layer of the chorion, constituting most of its total thickness, it is composed of a reticular network of parallel fibers, where fibroblasts and Hofbauer cells can be found. The nodes present in these fibers are found where they branch [33], [34], [40], [42] and the fibers that are secreted in the reticular layer are collagen fibers type I, III, IV, V, VI. These extend to the trophoblastic layer, uniting the different chorionic layers [33]. The basement membrane, also called pseudobasement membrane because it is an extremely thin membrane, is composed of type IV collagen, laminin, fibronectin [33] and dense argyrophil connective tissue attached directly to the reticular membrane, which sends branched and anchored fibers to the trophoblastic layer [34], [40], [42]. The last layer of the chorion in direct contact with the maternal decidua, the trophoblastic layer, consists of 2 to 10 layers of trophoblastic cells [33], [34], [40], [42], where we can also find Hofbauer cells [34], and has obliterated chorionic villi [33], [34], [42]. The depth of this layer can vary from 10 to 50 μm , making it difficult to conclude histologically with certainty where the cytotrophoblast ends and where the maternal decidua begins [33].

Chorionic membrane properties

Chorion has properties that, like amnion, make it an appropriate choice for use in regenerative engineering, such as:

- **Antiviral properties** – is based on the existence of the inhibitor similar to the cysteine proteinase inhibitor, cystatin E [43];
- **Antimicrobial properties** – its antimicrobial effect, against some microorganisms, has been proven, *in vitro*, previously by Kjaergaard *et al.* in 2001 [43]. This property has been proven against a large number of bacteria, including pathogens such as *Bacillus cereus*, *Staphylococcus saprophyticus*, *Pseudomonas aeruginosa*, *Escherichia coli*, among others [44];
- **Cell differentiation** – the cells that can be found in the chorion are pluripotent cells, capable of giving origin to cells of hematopoietic lineages, mesenchymal lineages and even trilineage germ lineage [3], [43];
- **Hematopoietic potential** – the hematopoietic potential of the chorion is enhanced through the existence of stem cell markers and differentiation clusters, CD34 and CD45, present in the various layers of cytotrophoblastic cells of the chorion [44];
- **Tissue repair and inhibition of scar formation** – its ability to repair tissues comes from the presence of cytokines and growth factors in this membrane. These molecules are key signaling molecules that are capable of carrying out various types of cellular processes, including those behind the healing repair and regeneration process [44], [45];
- **Very low immunogenicity** – its low immunogenicity allows this membrane to create an immune barrier and defend the fetus against the maternal immune system and prevent deterioration of the amniotic membrane [40], [44]–[47]. The protection that the chorion offers the fetus against the maternal immune system is related to the secretion of soluble proteins capable of blocking the production of antibodies, as well as being able to promote the production of some types of lymphocytes that prevent the natural immune response inside the mother's womb [46];
- **Anti-inflammatory properties** – The anti-inflammatory effect of the chorion is corroborated by the presence of interleukin 11 (IL-11) in this membrane [44], [45]. This cytokine has the ability to decrease

inflammation through the down-regulation of several pro-inflammatory mediators [48];

- **Self-adhesion** – this property is important, as this membrane can be used as an allograft, allowing it to not be necessary to use sutures to fix it in place [49]. If the allograft is placed dry, it has the ability to hydrate with the blood present at the site and become flexible, adjusting to the limits of the surface [44];
- **Cell adhesion** – Cell adhesion is provided by this membrane having bioactive cell adhesion factors such as laminin and fibronectin [47], [49];
- **Antibacterial properties** – studies prove that when compared to amnion, chorion has a superior antibacterial effect [44], [50];
- **Angiogenic properties** – this membrane has a high amount of pro-angiogenic growth factors (such as vascular endothelial growth factor (VEGF), EGF, platelet derived growth factor BB (PDGF-BB), angiopoietin-2, hepatocyte growth factor (HB-ECF, HGF), bFGF, angiogenein and placental growth factor (PIGF)) [3], [51]. The ability of this membrane to promote angiogenesis results in neovascularization [52], which is also made possible by the presence of bioactive cell adhesion factors in this membrane [49] and by the presence of growth factors that promote both vascularization and endothelial recruitment [51].

In addition to these properties, the chorion, relative to the amnion, is weaker than the amnion, having about 60 % of the strength of the amnion, and is about twice as extensible as the amnion [53].

Applications of CM in regenerative engineering

The chorion, such as the amnion, is a material that can be obtained through the placenta discarded after childbirth [29]. The chorion, being thicker than the amnion, has better handling properties making it a favorable biomaterial to be used in tissue engineering, regeneration and repair, medicine and even in stem cell research [44]. However, unlike AM and umbilical cord, which have been used clinically in the treatment

of patients for over a century, CM alone has only been studied as a biomaterial in the last few years [21], [54].

Before 2010, the chorion hadn't yet been used as a scaffold, unlike other placental components that have already been used in clinical practice. A study published in 2010 demonstrated the viability of creating a scaffold through the use of the connective tissue of the chorion with MSCs [55]. Chorion contains unique properties that make it a good material for the formation of the scaffolds. Go *et al.* demonstrated that chorion extracts significantly increase the osteogenic differentiation of MG-63 cells when compared to amnion, which may be a consequence of the existing differences in the composition of each membrane, namely in osteogenesis-related growth factors such as EGF, bFGF and transforming growth factor beta 1 (TGF- β 1). This suggests that the chorion is a possible therapeutic material for bone TE as opposed to materials made from ECM, mostly used for soft tissue regeneration [21].

It is assumed that in 2012, the chorion was used for the first time for enhancement of thin gingival biotype to thick biotype and also for root coverage [56]. This application is due to the fact that the chorion contains fibronectin [33], [56], which in turn is involved in cellular processes, such as cell adhesion and migration, tissue repair and blood clotting processes. In addition to fibronectin, the chorion also has other cell adhesion molecules [56], such as laminins [33], [56], which allows that in this type of graft it isn't necessary to suture the membrane where the application is intended [56].

There are several reports of use of the chorion in periodontics [44], [48], [57]. A study carried out in 2013, demonstrated that the chorion can be used as a barrier membrane in periodontal pocket therapy. Its use has significantly improved the clinical and radiographic parameters compared to the isolated periodontal pocket therapy, mainly with regard to the amount of bone regeneration [57], also offering an anti-inflammatory effect [48]. The chorion was used as a barrier membrane between the hard tissue and the gingival epithelium, in order to promote the formation of progenitor cells, from the periodontal ligament cells, for the regeneration of new tissues [57]. The advantages of using bioabsorbable CM in these applications is that there is no need for a second surgical procedure [44], [48], [57], which makes the clinical results better without attachment gain or interruption of bone filling, the chorion offers early stability at the graft site after

transplantation [57], the membrane, being self-adhesive, doesn't need to be fixed with sutures and when it is dry in place, it is quickly hydrated with blood, which makes it very flexible, adapting well to the contours of the alveolar bone [48].

In 2015, it was demonstrated that it was possible to completely separate and decellularize small-diameter vascular structures from the chorionic plate [58]. These vessels can be used to replace small diameter vessels [15], [22], [58] or for 3D cell culture [15], [58]. Lak kireddy *et al.* (2022) demonstrated that decellularized human chorion, compared to decellularized human amnion, is more effective in inducing cell adhesion and proliferation. Other studies carried out indicate that decellularized CM can be used for the production of vascular grafts, if the chorionic membrane is wrapped in tubes, and also for tissue regeneration [22].

The timeline of these applications is shown on the next figure, **Figure 1.6**.

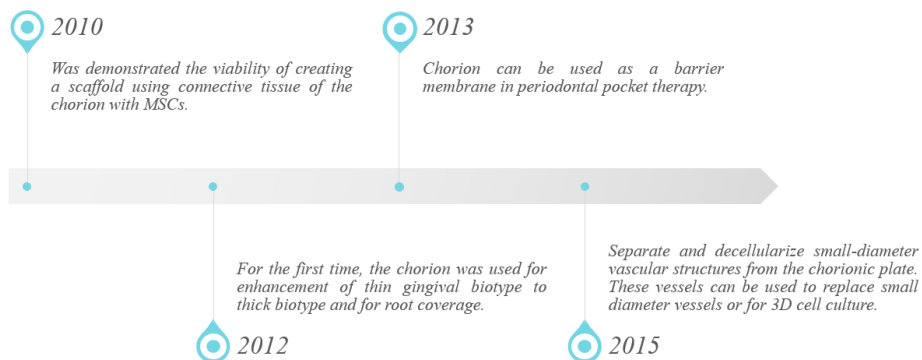


Figure 1.6 – Timeline of CM applications.

1.4.6. Spongy Layer

Spongy layer, also known as the virtual membrane (VM), as mentioned earlier, is made up of Hofbauer cells [34], fine fibrils surrounded by mucus [1], non-fibrillar collagen type III network, an abundance of glycoproteins and proteoglycans, mainly hyaluronic acid [3], [35] and some isolated fibroblast [34].

The spongy layer present in the amnion [1]–[3], is the membrane that separates it from the chorion [59]. It is the layer that allows the amnion to move over the chorion, which is attached to the maternal decidua [34], [60] and is responsible for the increase in

thickness that the amnion can undergo [34]. This layer presents wavy bundles of reticulin, which in turn are bathed in mucins [34].

There aren't many studies with the spongy layer, it is usually discarded when preparing the amnion for grafts. However, Hopkinson *et al.* 2006, hypothesized that it is a source of growth factors, in addition to those present in the amnion, such as TGF- β [61].

Applications of mucins in regenerative engineering

The spongy layer, as mentioned earlier, is a layer made up of different components, among which are the mucins [3], [35].

Mucins belong to a family of highly glycosylated proteins, the glycoproteins [62]–[66]. These proteins have a high molecular mass, being rich in thiol groups (with charged and hydrophobic properties) [64], serine, threonine and hydroxyproline, which allows post-translational O-glycosylation, as well as cysteine-rich areas, which play a role in intermolecular crosslinking [65]. Due to their oligosaccharide side chains, carboxyl groups [64] sulfate residues [63], [64] and terminal sialic acid [63], they are negatively charged [63], [64].

They are the main component of the structure of the mucus layer [63], [64], [66] that is found over the moist epithelia of the human body, such as the female genital tract, respiratory tract and gastrointestinal tract [64], [67]. These confer the viscoelastic properties common in mucus [62], have the ability to retain water and are resistant to proteolysis, which are characteristics identical to the gel found in mucous membranes [65]. Mucins play an important role in the defensive and offensive mechanisms of several species [66], protecting them against bacteria, virus or other small organisms that may be present [64]. These exhibit primary properties such as lubrication, dynamicity, bioactivity, barrier and hydration [66].

Mucins have the ability to interact chemically and physically with each other and with other components of the mucus, forming a structure identical to a mesh, which may have pores of about 10 to 500 nm, thus being able to regulate the entry of particles, microbes and drugs to the epithelium [63]. Its barrier property proved to be an opportunity to study the exploration of interactions between mucins with drugs, for the delivery of different types of drugs over long periods of time [64]. In addition to their interaction

with other mucus components, mucins are also capable of interacting with a range of distinct polymers [67].

There are studies that demonstrate the role that mucins can play. In 1997 Sweeney *et al.* demonstrated that it can be used as an oral spray and in 1998 Davies *et al.* reports that about 73% of xerostomic patients improve with mucin-based salivary substitutes. This is because they have a hydrated topical coating, which helps to alleviate oral mucosal complications [68].

Shi *et al.*, in 2000, showed that mucins have the ability to avoid bacterial adhesion and improve surface wettability of synthetic materials (silicone, polystyrene, poly(methylmethacrylate) or polyurethane), being very useful in the coating of biomedical devices, such as catheters or stents, which need to have low friction and surface lubricity. A similar study was conducted by Crouzier *et al.*, (2013), who showed its usefulness to coat biopolymers, repelling cells from these. This can be used to control the regulation of adhesion of certain types of cells. Also in 2013, Thasneem *et al.*, demonstrated that mucylated nanocarriers have a reduced opsonization effect with favorable cyto- and haemo-compatibility [68]. Mucins can also be used to coat implants, causing inhibition of platelet adhesion and preventing thrombosis, which was demonstrated by the study by Janairo *et al.*, (2014) [68].

In 2009, Johnson *et al.*, showed that peptide microtubes with mucin glycoproteins have better cellular adhesive properties and that these allow the dispersion of cells through their microtubular structural aggregate. Which can be used for medication delivery as well as improving their bioavailability [68]. Drug. *et al.*, (2010), through their work, demonstrated that the mucin complex with hydrophobic molecules improves the aqueous solubility of these molecules, giving them better membrane penetration capacity and bioavailability [68]. Also in 2010, Gozin and his collaborators showed that, in aqueous solution, bovine submaxillary mucin is capable of balancing dispersions of hydrophobic nanocolloids [68]. Wang *et al.*, in 2012, created a stimuli responsive multilayered scaffold with poly(acrylamide-co-3-acryl-amidophenylboronic) acid and porcine gastric mucin, which under certain stimuli, the multilayers can be decomposed, which can be used to induced drug delivery [68]. In 2014, Araújo *et al.*, proved that chitosan-coated

nanocarriers show a sustained release of payload through their mucoadherent tendency [68]. It was demonstrated by two studies, Crouzier *et al.*, (2012) and Polak *et al.*, (2014), that through mucin sugar–lectin interactions, robust multilayers, stable against pH changes and salt effects, can be created for systems targeted drug delivery [68].

In 2015, a published study demonstrated, for the first time, the assembly into hydrogels of mucin biopolymers with the ability to release or retain therapeutic molecules in a sustained manner [64], [68].

Finally, in 2021, a published study proposed the hypothesis that hybrid polymer scaffolds, containing mucin and collagen, may play a relevant role in increasing bone formation *in vitro* 3D matrices. In this study, it was proven that a biomimetic dual network system composed of collagen, mucin and polyethylene glycol dimethacrylate created is superior in terms of performance compared to other scaffolds that may or may not contain individual proteins and that the mineral matrix that is deposited showed osteoplastic activity properties with significant gene expression [65].

The timeline of these applications is shown on the next figure, **Figure 1.7**.

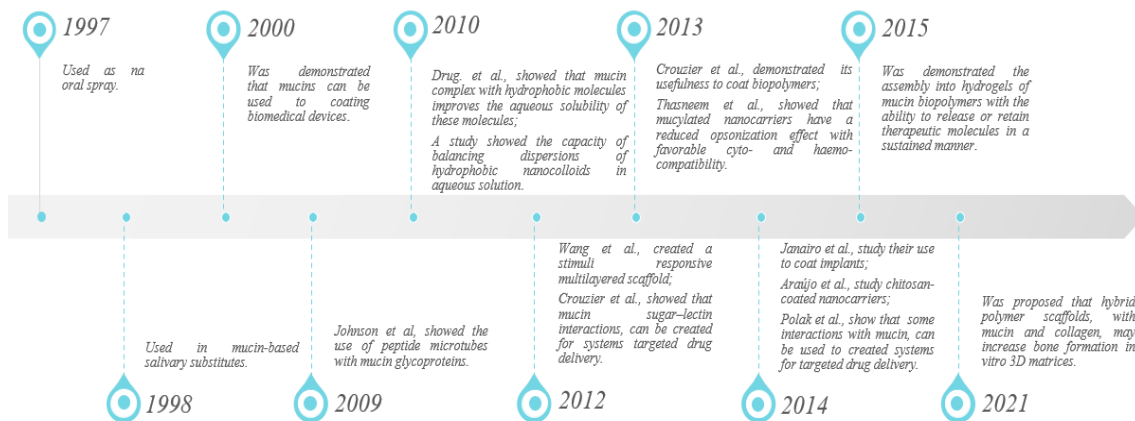


Figure 1.7 – Timeline of mucin applications.

1.4.7. Composition of ECM in each layer of the placenta

The following table, **Table 1.1**, summarizes the composition of the ECM on each layer that is present in the placenta.

Table 1.1 – Summary of *ECM Composition* on each layer of placenta.

| | <i>Layer</i> | <i>ECM Composition</i> | <i>References</i> |
|----------------|-------------------|---|------------------------|
| <i>Amnion</i> | Epithelium | AECs | [1], [3], [24] |
| | Basement membrane | Collagens type I, III, IV, V, VI and VII, laminin, fibronectin, elastin, nidogen and other types of integrins | [1], [24], [33] |
| | Compact layer | Reticular fibers and Hofbauer cells | [1], [34] |
| | Fibroblast layer | Fibroblasts, proteoglycans, non-collagenous glycoproteins, AMSCs, collagens type I and III and Hofbauer cells. | [1], [3], [33], [34] |
| | Spongy layer | Fine fibrils, glycoproteins, proteoglycans (hyaluronic acid), non-fibrillar collagen, Hofbauer cells and fibroblast | [1], [3], [34], [35] |
| <i>Chorion</i> | Cell layer | Fibroblasts and Hofbauer cells | [34], [40], [42] |
| | Reticular layer | Fibroblasts, Hofbauer cells, collagen type I, III, IV, V, VI | [33], [34], [40], [42] |
| | Basement membrane | Collagen type IV, laminin, fibronectin | [33] |
| | Trophoblasts | Trophoblastic cells and Hofbauer cells | [33], [34], [40], [42] |

1.5. Decellularization protocols

The main goal of decellularization methods is the removal of all nuclear and cellular components existing in the membranes and the preservation of their mechanical integrity, biological activity and their composition [9]. There are two types of decellularization, physical and chemical. Physical decellularization takes place through successive cycles of freezing/unfreezing, pressure gradients, contact with supercritical fluids agitation and physical detachment/scraping. Chemical decellularization takes place through the treatment of membranes with chemical agents such as acids, alcohols, detergents, chelating agents, alkalis and enzymes. Although chemical decellularization methods are usually more aggressive, affecting more the properties of the ECM, these are also the ones that allow an efficient removal of cellular contents [69].

An extensive bibliographic research was performed concerning the different methodologies used for the decellularization of fetal membranes and different protocols are described and compared in **Table 1.2**.

As can be observed, all the protocols present disadvantages, namely not being sufficiently effective in eliminating all the cells and significantly decreasing the concentration of biomolecules that are wanted to be preserved namely glycosaminoglycans (GAG's), growth factors and cytokines. Also, and not less important, some of the protocols do not allow the preservation of membranes morphology. Therefore, the optimization of decellularization protocols is needed.

Table 1.2 – Comparison between decellularization protocols.

| <i>ID</i> | <i>Ref.</i> | <i>Membrane</i> | <i>Reagents</i> | <i>Results</i> | <i>Advantages / Disadvantages</i> | <i>Observations</i> |
|-----------|-------------|-----------------|--|--|--|---|
| <i>1</i> | [69] | Amniotic | Triton X-100 1 %; DNase; Phosphate buffered saline (PBS); 4 % paraformaldehyde (PFA). | Not all existing cores were eliminated; Triton X-100, ruined the regular structure of the amniotic epithelial cell membrane; Lipase didn't completely eliminate the remaining nuclei; Resulted in an ECM too loose; Excessive enzymatic reactions destroyed the mechanical properties of the amnion. | Advantages: Doesn't use dimethyl sulfoxide (DMSO) or sodium dodecyl sulfate (SDS). Disadvantages: The membrane wasn't fully decellularized. | Methods used to preserve the integrity of the ECM and to eliminate epithelial cells; Triton X-100, is a non-ionic surfactant with the ability to denature protein in a mild manner; Protocol name: 1 – SD; 2 – HD; 3 – LD; 4 – SLD. |
| <i>2</i> | | | NaCl; PBS; DNase; 4 % PFA. | | | |
| <i>3</i> | | | Lipase; PBS; DNase; 4 % PFA. | | | |
| <i>4</i> | | | Triton X-100 1 %; Lipase; DNase; PBS; 4 % PFA. | | | |

Cont.

Cont...

| | | | | | | |
|---|------|----------------|--|--|--|--|
| 5 | [15] | Chorion | PBS; TRIS; 0.1 % EDTA; 0.5 % SDS; DNase; MgCl ₂ ; Deionized water. | Elimination of nuclear and cytoplasmic material; The network patterns in native and decellularized tissue are identical; Structure of ECM maintained; Reduction about 98.5 % of components such as collagen IV, laminin and fibronectin; Preservation of structural characteristics. | Advantages: Effective decellularization Disadvantages: Uses SDS | SDS damages the elements present in the ECM. |
| 6 | [70] | ECM / Placenta | Distilled water; 0.5 % SDS (diluted 1:1); 0.2 % DNase; RNase. | Elimination of fat acids and cells; Considerable decrease of dsDNS in decellularized ECM; Conservation of large amounts of collagen, elastin, and GAG's; Decreased content of growth factors, but still present at high levels (TGF- β 1, bFGF, EGF, PDGF, IGF-1, and VEGF). | Advantages: Effective decellularization Disadvantages: Uses SDS; Decellularization takes about 5/6 days. | Of the 80 bioactive molecules in the native placenta, 27 types of immune response-related cytokines and 25 types of growth factors were preserved. |
| 7 | [71] | Amniotic | Distilled water; PBS; Antibiotic agents; Antifungal agents; 0.2 % EDTA; 0.5 M NaOH; 5 % Ammonium Chloride. | There was a decrease in the suture retention strength; Total removal of cells; About 95 % of DNA was removed; The amount and distribution of type I, III and IV collagens remained intact. | Advantages: It doesn't use DMSO or SDS. Disadvantages: Membrane isn't completely decellularized. | |

Cont.

Cont...

| | | | | | | |
|---|------|----------|---|---|---|---|
| 8 | [41] | Chorion | 0.5 % SDS; ultrapure water; 0.1 % SDS; 1 % Triton X- 100; PBS; DNase I; 1-2 % antibiotic / antimycotic. | Removal of nuclear material; Existence of DNA fragments with less than 200 bp; The amount of dsDNA /mg of dry tissue is less than 50 ng/mg. | Disadvantages: Uses SDS. | During this process the chorion is without the trophoblastic layer; Freezing/thaw ing cycles allow the creation of ice crystals, which break the cell membrane and lead to cell lysis; Due to the thin thickness of the membrane, exposure times to detergents may be short; The placement of solutions under agitation allows better exposure of the fabric to the solutions. |
| 9 | [72] | Amniotic | Distilled water; 0.2 % EDTA; 0.5 M NaOH; 5 % NH ₄ Cl; PBS. | Effective separation of cells and tissue. | Advantages: Minimal negative effect for ECM; Increased <i>in vivo</i> biocompatibility of decellularized amnion; Good cost benefit; Simplicity; Speed; Security; It doesn't use DMSO or SDS. | Effective, simple and fast method with a good cost- benefit ratio. |

Cont.

Cont...

| | | | | | | |
|----|------|----------|--|---|---|--|
| 10 | [72] | Amniotic | Hypotonic Tris buffer; 0.1 % EDTA; Aprotinin; 0.03 % SDS; TBS; 0.1 % EDTA; DNase; RNase; Tris-HCl; Magnesium chloride; Bovine serum albumin; 0.1 % peracetic acid; PBSa. | Effective tissue decellularization. | <p>Advantages: Effective decellularization.</p> <p>Disadvantages: These procedures cause damage to the ECM and the basal membrane of the tissue; Rupture, shrinkage or cross-contamination with other microorganisms may occur when handling inappropriately; Using SDS and DMSO.</p> | Most cited alternative decellularization procedures. |
| 11 | | | Glycerol or DMSO; PBS; 0.025 % EDTA. | | | |
| 12 | [24] | Amniotic | PBS; 0.01 % SDS; 0.01 % SD. | Preservation of the structural architecture of the amnion; Cells with signs of apoptosis and with a pycnotic cell nucleus; Conservation of the structures where the cells were located; | <p>Advantages: Effective decellularization.</p> <p>Disadvantages: Unfeasible cellular components, possibly by the use of SDS.</p> | The use of SDS may cause a decrease in GAG's concentration and a loss in collagen integrity. |
| 13 | [73] | Placenta | Hypertonic Saline Solution; Isotonic Saline Solution; 20 % SDS; Hydrogen Peroxide Solution; Absolute ethanol. | All cells were eliminated; All cores have been eliminated. | <p>Advantages: Quick and fast-running protocol; Effective decellularization.</p> <p>Disadvantages: Using SDS.</p> | |

Cont.

Cont...

| | | | | | | |
|----|------|----------|---|---|---|--|
| 14 | [74] | Placenta | <p>PBS; 0.01 %, 0.1 % and 1 % SDS; Distilled H₂O; 1 % Triton; Penicillin; Streptomycin.</p> | <p>Vascular structures remained unalterable; The DNA found represents < 1 % of the intact placenta; Removal of nuclear cells; Preservation of the stroma; It presents empty vascular and luminal spaces with ECM protrusions; Larger and more branched placental vessels that lead to filled and intact cotyledons.</p> | <p>Advantages: Effective decellularization; Preservation of membrane structure.</p> <p>Disadvantages: Using SDS.</p> | |
| 15 | [75] | Placenta | <p>96 % N₂/4 % CO₂ gas blend; 95 % O₂/5 % CO₂ gas blend; hypotonic tris buffer solution; 1 % lauroyl sarcosinate; tris base; high salt concentration; 1 % tris-buffered solution of lauroyl sarcosinate; DNase; RNase; 1 % Triton-X100; 1 % ABAM; 1 % PMSF.</p> | <p>Collagen conservation; Removal of cells and cellular debris; Elimination of elastin; Total elimination of DNA and RNA of the matrix; Collagen type IV preserved in the chorionic plate and in the extensions of the villous tree; Laminin preserved in the chorionic plate; Conservation of vascular architecture.</p> | <p>Advantages: Doesn't use DMSO or SDS; Effective decellularization.</p> <p>Disadvantages: Decellularization performed in several days.</p> | |

Cont.

Cont...

| | | | | | | |
|----|------|----------|--|--|---|---|
| 16 | [76] | Amniotic | 0.05 % Trypsin; 0.02 % EDTA; PBS | Collagen conservation; Increase area occupied by collagen; Increase of small collagen fibers type III; Decrease of about 21 % of immunohistochemistry for fibronectin expression. | <i>Advantages:</i> It doesn't use DMSO or SDS. | |
| 17 | [77] | Amniotic | PBS 1x w/o Ca ⁺⁺ , Mg ⁺⁺ ; 0.1 % antibiotic antimycotic; NaOH; Distilled water; Sterile PBS. | Conservation of ultrastructural membrane; Removal of cells and nuclei. | <i>Advantages:</i> Doesn't use DMSO or SDS; Effective decellularization. | |
| 18 | [78] | Chorion | 1.2 % NaCl; 0.4 % NaCl; 1 % Triton X-100; 0.02 % EDTA; DNase I; Sterile PBS; 0.1 % PAA. | Removal of all DNA and cellular residues; Collagen conservation; Only 30 % of GAG's content has been preserved. | <i>Advantages:</i> The use of pressure-comprobed pulsatile perfusion increases cell elimination and decreases triton X-100 exposure time by 1 % Effective decellularization. <i>Disadvantages:</i> Loss of GAG's. | Use of pulsatile flow perfusion system. |

1.6.Characterization techniques

1.6.1. FTIR spectroscopy

Spectroscopy is a cluster of vibrational techniques that uses the interaction of matter with electromagnetic radiation to acquire chemical and physical information about the samples to be analyzed [79]. Infrared spectroscopy studies the interaction of matter with infrared light, in the region of wavelengths (λ) between 0.7 μm to 1 mm of the

electromagnetic spectrum [79], [80]. All molecules of a given material are in constant motion and have their own frequencies related to their rotation and vibration movements [79]. When a beam of light in the infrared region is directed at a sample, the λ that will be absorbed are dependent on the molecular vibrations of the sample in question. Therefore, it is possible to determine the structural and chemical information of a sample, through the absorbance in the infrared region [80].

FTIR spectroscopy can be used to characterize the structure and composition of membrane samples [76]. This type of spectroscopy is a tool capable of providing qualitative and quantitative information on the structural properties of the analyzed samples and offers information on molecular bonds based on the intensity of the represented infrared absorption bands, their position and possible modifications that may occur due to environmental factors. Its main advantage is that it allows the investigation of the secondary structure of proteins either in a dry or aqueous state, making it possible to study the changes that occur at the molecular level [81].

For the acquisition of FTIR spectra, different types of experimental configurations can be used, in particular by transmission, transfection and by Attenuated Total Reflection (ATR) [79]. In the ATR configuration, the sample, which can be in solid or liquid state, has to be placed directly in contact with an internal reflection element (which can be a diamond, a ZnSe prism, germanium or silicon), where the infrared light will be fully reflected internally. For total internal reflection to occur, the angle of incidence of the infrared beam must be greater than the critical angle and the refractive index of the material must be greater than that of the material being analyzed. The radiation that falls on the material is attenuated and penetrates it in the form of an evanescent wave [79], [80], [82]. This technique is ideal for samples that are very absorbent and for thin film samples and surface measurements, because the penetration depth of light is small [82]. The calculation of the penetration depth (d_p) of the light beam in the sample can be performed through Eq. 1.1 [82].

$$d_p = \frac{\lambda}{2\pi\eta_r \sqrt{\sin^2 \theta - \frac{\eta^2}{\eta_r^2}}} \quad (\text{Eq. 1.1})$$

where, the wavelength is represented by λ , η_r and η are the refraction indices of the internal reflection element and the sample, respectively, and θ represents the degree of incidence of the light beam [82].

1.6.2. Differential Scanning Calorimetry/ Thermogravimetry

To study the thermal characteristics of the samples, two types of thermoanalytical techniques were used: DSC and TGA.

The DSC technique is derived from the differential thermal analysis (DTA), technique and studies the energy supplied to a reference material together with a sample in function of the temperature change [83], [84]. Depending on the measurement method used, DSC can be classified as differential scanning calorimetry with heat flux or with power compensation, but in either case, the effects caused by heat related to chemical and physical changes in the material are evaluated [83]. Changes in the DSC curves, caused by the effects of temperature, can be first-order transitions (enthalpy transfer that generates endothermic peaks, negative peaks, or exothermic, positive peaks) or second-order transitions (change in heat capacity without change the enthalpy). The measurement method used in the present study was heat flux DSC, where the basis for determining the heat released or absorbed by the sample is the temperature difference between the sample and the reference material [83].

TGA is a thermoanalytical technique that studies the mass alteration of the sample to be analyzed as a function of temperature variation [84]–[86]. For this type of technique, the parameters of time, mass and temperature are fundamental [85], which allow identifying the moment when the material begins to change, caused by changes in temperature [86].

1.6.3. Confocal Raman Microscopy

Confocal Raman microscopy is a non-invasive technique [87], [88], which doesn't require the samples to be previously treated before being analyzed [89]–[91], doesn't cause degradation in the analyzed samples [88]–[90] and can analyze at different depths [88], [91]. This technique isn't affected by the presence of water in the sample and is a very specific technique [92], each analyzed sample has its own Raman spectrum [92],

that is, it has its own molecular fingerprint [93], [94]. The intensity of each peak in the Raman spectrum is directly related to the amount of each material that composes the sample [94] and the position that each peak occupies in the spectrum is related to a specific type of component [89].

The confocal Raman method is based on the phenomenon of inelastic scattering of light [87], [90], [95] when a laser is incident on a sample [87], [91]. In this phenomenon, the photon energy is transferred to the molecules that make up the sample, causing its characteristic vibration [90], [94], [95]. The vibration intensity of the molecules that make up the sample is recorded and its chemical composition can be visualized [93], [94].

1.6.4. Atomic Force Microscopy

Atomic force microscopy, AFM, also called scanning force microscopy, SFM, [96] is a technique capable of directly measuring and taking images of the 3D topography of the surface of a sample, at atomic scale (nanometric), and also the physical properties of the surface of the sample, through the use of a pointed probe [96], [97]. The use of this technique allows the acquisition of information regarding the quantitative parameters of the surface roughness of the sample to be analyzed [97], [98]. It also allows observing the nanotexture of the surface of the analyzed materials [97], as well as extracting information about their morphology, size and shape of the particles present on the surface of the materials [96]. This technique is used in relation to other microscopy equipment, such as transmission and scanning electronic microscopy, in the study of polymers, because it allows direct measurements of surface roughness and height, it doesn't use coatings for the samples, nor vacuum, in ordered structures it has the ability to provide images with atomic resolution and has a lower operating cost than electronic microscopy [98].

The AFM uses a cantilever, a flexible rod, in which at the bottom of its extremity there is a tip that has a micrometer thickness [97], [99]. The tip is at a nanometer distance from the surface of the sample, moving over this in orthogonal directions (x, y) [99]. To obtain an image and scan the sample, a positioning system that uses piezoelectric ceramics is used, covering the surface of the sample in three directions (x, y, z) with angstrom precision. An alignment system with a laser beam focused on the cantilever is

also used, which will reflect on a sensor with four quadrants [97]. The sensor communicates with software, sharing location information, which allows correcting the position of the cantilever in order to obtain the desired image [97], [98]. A scheme of the AFM operation is represented in **Figure 1.8**.

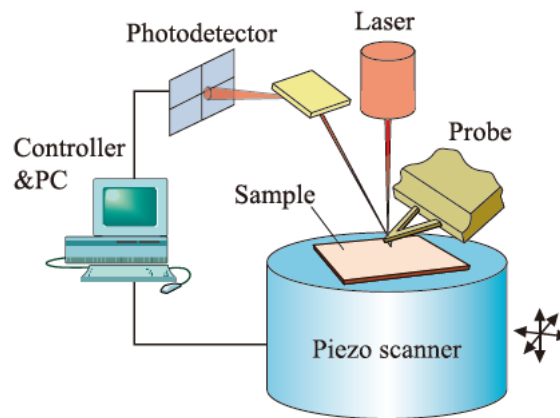


Figure 1.8 – Schematic drawing of the AFM [100].

The cantilever undergoes deflection when interacting with the sample surface due essentially to Van der Waals forces [98], [99], and may also be affected by Lennard-Jones forces [99], and less significant forces, Colombian and magnetic [98]. This deflection is controlled through laser interferometry, which makes it possible to track the increase or decrease in interatomic forces, caused by vertical changes in the surface of the sample [99].

There are three modes of operation of the AFM, the contact mode, the non-contact mode [97], [98] and even in some equipment the intermittent contact mode [98]. The contact mode occurs when the cantilever operates in the repulsive region, where the closest proximity exists between the cantilever and the sample surface. This proximity is only a few angstroms away and the repulsive forces make the cantilever to be deflected away from the sample [97], [98]. When the cantilever acts on the attractive region, we are in the non-contact mode, here the cantilever is a few tens or even hundreds of angstroms away from the sample, being attracted by its surface, which make it to be deflected in its direction [97], [98]. Finally, the intermittent contact mode is the junction of the two previously mentioned modes. Its operating principle is similar to the non-contact mode,

but here the tip is closer to the surface of the sample, which occasionally touches on the sample surface when it's in the lowest position, as it happens in contact mode [98].

The mode to be used is chosen based on the intended application and whether the sample is rigid or not. The contact mode is more appropriate for rigid samples since there is a lower probability of the tip damaging their surfaces.

The non-contact and intermittent modes have little contact with the surface of the sample, being more suitable for less rigid samples that will be damaged if touching occurs. However, the intermittent mode is more effective than the non-contact mode for acquiring images with a larger sweep area that may contain greater topographical variations [98].

1.6.5. Zeta Potential

Zeta potential measures the surface charge (electrostatic or electrokinetic) of that develops at the interface between a solid surface and its liquid medium when there are particles in suspension [101]–[104]. This potential, which is measured in mV, may arise by any of several mechanisms. Among these are the dissociation of ionogenic groups in the particle surface and the differential adsorption of solution ions into the surface region. The net charge at the particle surface affects the ion distribution in the nearby region, increasing the concentration of counterions close to the surface. Thus, an electrical double layer is formed in the region of the particle-liquid interface. The value of the zeta potential, represented in **Figure 2.3 a)**, indicates the interactions that exist between the particles, that are responsible for the dispersion behavior of the particles [101], [103], [104].

1.6.6. Rheology tests

Rheology is used to describe and assess the deformation and flow behavior of materials. Fluids flow at different speeds and solids can be deformed to a certain extent. Rheological tests are carried out in order to study the flow and deformation of matter [105]–[107]. The analyzed materials can be in liquid, solid and gaseous state. There is also the possibility of the material having liquid and solid characteristics, being a viscoelastic

material [107]. Hydrogels are inherently viscoelastic, meaning they exhibit both viscous and elastic behavior.

The flow behavior of materials is directly related to their structure, and changes that occur at structural levels are closely related to their rheological properties [105], [107].

With the information obtained through these tests, the structure of the materials can be changed, in order to achieve the intended rheological properties for certain purposes [105]. This type of testing is widely used in industry as a product quality control mechanism [107] and for creating new intended products [106], [107].

CHAPTER 2 – MATERIALS AND METHODS

2. Materials and Methods

2.1. Membrane's obtaining process

The fetal membranes used in the present project were collected according to a protocol previously established in our group. First of all, it is necessary to obtain the informed consent of the donors, in accordance with the established by the principles of the Declaration of Helsinki, with regard to research involving human subjects. That said, the placentas were collected after delivery. In order to guarantee the maximum quality of the collected samples, they were collected only after cesarean sections, under sterile conditions [108], through protocols authorized by the Ethics Committee of the Aveiro Hospital. After collection, the samples were kept in normal saline solution, at 0.9 %, at a temperature of 4 °C and processed within 24 hours.

Collected placentas were treated under sterile conditions. The different membranes that constitute the placenta, amniotic membrane, chorionic membrane, and spongy layer, were separated and washed in sterile solutions that also contained fungicides and antibiotics. After being cleaned, these membranes were trimmed and individually placed in sterile DMEM: Glycerol (ratio 1:1) and finally preserved by freezing at -80 °C for further analysis.

2.2. Decellularization method

One of the main objectives of the present work was the optimization of a decellularized protocol previously used in our group (Annex A), by eliminating the use of dimethyl sulfoxide (DMSO), since recent studies show that the use of DMSO should be avoided because even at low concentrations it is not inert, inducing changes in cellular processes in both cardiac and hepatic cells, but more severely, induce alterations in miRNA and epigenetic landscape in the 3D maturing cardiac model [109].

The improved protocol can be briefly described as follows. Firstly, membranes were unfrozen in a water bath at 37 °C. Then they were washed three times with Distilled water (dH₂O) and shake for 15 min (electric shaker). After that, membranes were immersed in Buffer A (dH₂O + 1.214 g u/l of Tris + 0.1 g of EDTA for each 100 ml of

final solution, at pH=7.8) and kept in that solution for 18h with agitation (electric shaker). Then they were washed again three times with dH₂O, shake for 15 min (electric shaker) and kept in Triton 1 % solution overnight at 37 °C (IKA 50-70). After, two cycles of washing were performed, the first one with Buffer B and the second one with dH₂O (three times each, 15 minutes wash, electric shaker). Then membranes were immersed in a solution containing distilled water (45 ml) + Tris (0.1214 g) + MgCl₂ (0.0095211 g) + 200 U/mL DNase, at pH=7.8 for 3h, at 37 °C (IKA 50-70). A final washing cycle with dH₂O was performed in the same conditions as previously described. Finally, membranes were kept in dH₂O and were frozen at -20 °C or -80 °C.

2.3.Membrane's lyophilization method

Lyophilization, also called cryodehydration or freeze-drying, is a dehydration method that eliminates the water present in a tissue by a process of sublimation followed by desorption [110]–[112]. The lyophilization process consists of 3 phases: freezing, primary drying, in which the largest amount of water is eliminated through sublimation, and secondary drying, which eliminates, by desorption, a certain amount of water that is bound [111], [113]. Freezing is one of the most important steps in this entire process [111], [113]. At this stage, the product to be lyophilized is fixed, by freezing it by exposure to temperatures below its freezing point [111], which allows biological activities and chemical reactions to be suspended [113].

This method requires a long period of time and needs to be carried out under particular conditions of temperature and pressure, so that the frozen water present in the tissues passes directly from the solid state to the gaseous state, without passing through the liquid state, with sublimation occurring [111], [112]. The lyophilization process, as opposed to other dehydration methods, is effective against characteristics such as thermal decomposition, protein denaturation, loss of volatiles, product contraction and enzymatic actions, therefore destructive chemical reactions that can lead to the alteration of the tissue in question [110]–[112]. Lyophilized membranes compared to cryopreserved ones are macroscopically weaker and thinner [110]. In addition, they are easy to transport and they can be stored at room temperature, without deterioration, for an extended period of time [110], [113].

In the development of this work, amniotic, chorionic and spongy layer membranes were lyophilized using lyophilizer Freeze Dryer Freezone 2,5 L of Labconco and a temperature of (-80 °C).

2.4.Membrane's staining methods

In order to be able to observe the results of the decellularization of the membranes, and their cellular structures under the microscope, membranes were fixed overnight in formalin (10% neutral buffered formalin) and embedded in paraffin. After, sections of 3 µm thickness were sequentially obtained and stained using hematoxylin and eosin (H&E) and Picro-Sirius Red/Alcian Blue (PSR-AB).

H&E staining is abundantly used in histological procedures [114], being used for several decades in pathology [115]. This type of staining makes it possible to distinguish basophils, acidic components (cell nuclei that contain DNA or RNA and certain areas of the cytoplasm), and acidophiles, basic structures present in the cytoplasm of the samples [114], [116]. Hematoxylin is a base that has a blue-purple color and stains basophils with bluish tones, whereas eosin is an acid with a pink color and stains proteins, connective tissues and cytoplasm with pink [114]–[116].

PSR-AB staining is useful for determining the type of material found within the lacunar space [117]. Picro-sirius red is an anionic dye that stains collagen with pink on a pale yellow background [117]–[119]. This collagen staining is related to the reaction that occurs between the basic groups present in collagen with sulfonic acid [117]. Alcian blue is a cationic dye that reveals the presence of sulfated and carboxylated sialomucins, glycoproteins, and sulfated and carboxylated acid mucopolysaccharides (GAG's), staining them with blue [117], [120]–[123]. The reaction takes place with electrostatic bonds formed with tissue polyanions that contain sulfate or carboxyl groups [117].

The staining membranes protocols, by the two mentioned methods are described below.

2.4.1. H&E staining protocol

1. Dewaxing of the membranes. To dewax the membranes, they were placed:

- a. 3 times in Xylene, 3 min each time;
 - b. 2 times in Ethanol (EtOH) 100 %, 3 min each time;
 - c. 3 min in EtOH 96 %;
 - d. 3 min on EtOH 70 %;
 - e. 3 min on EtOH 50 %;
 - f. 3 min on ddH₂O;
2. Immersion of the membranes in Gill's Hematoxylin;
 3. Washing of the membranes in tap water for the double time of the hematoxylin, so in this case, for 6 min;
 4. Immersion of the membranes in:
 - a. a gradient of EtOH, starting with EtOH 50 %, EtOH 70 %, EtOH 96 % and EtOH 100 %, for 1 min each;
 - b. Eosin for 1 min;
 - c. 3 times in EtOH 100 %, 1 min each time;
 - d. 3 times on Xylene, for 3 min each time;
 5. Mounting the slides with Entellan.

2.4.2. PSR-AB staining protocol

1. Dewaxing of the membranes following procedure mentioned above for the H&E staining;
2. Immersion of the membranes 3 min on Gill's Hematoxylin;
3. Washing of the membranes in tap water for 6 min;
4. Immersion of the membranes on Alcian Blue for 30 min;
5. Washing the membranes in tap water for 2 min;
6. Immersion of the membranes on Sirius Red for 1 hour;
7. Washing of the membranes in acidified water for 30 seconds;
8. Washing of the membranes in distilled water;
9. Air drying of the samples (until slides are completely dry);
10. Mounting the slides with Entellan.

2.5. Membrane's characterization methods

2.5.1. Histological analysis

After staining the membranes, they were observed under a light microscope. The microscope Leica DM2000 LED was used, with a magnification of 10x, connected to a camera and to a computer. Through a software, Leica LAS X, the images of the most interesting areas of each sample were captured to enable their later analysis.

This type of analysis gives us visual information about what is present in the membranes after they have been decellularized, and evaluate if the intended cellular components, namely cell nuclei, were eliminated. Complementary analysis using other techniques can also be performed in order to investigate the presence of biochemical components such as collagen and GAG's or specific glycoproteins in the membranes.

2.5.2. FTIR spectroscopy

The type of configuration used in this analysis was the ATR being the sample placed directly in contact with an internal reflection element, a diamond crystal, where the infrared light was fully reflected internally. For this analysis, a PerkinElmer (Frontier model) spectrophotometer was used and the PerkinElmer Spectrum software (version 10.5.2.). A resolution of 4 cm^{-1} was used and 200 scans were acquired in each sample analysis. Background signal was acquired using the same conditions. Further data treatment (baseline correction, peak labels, plotting of the graphics) was performed in the free SpectraGryph software, version 1.2.15. [124]. For the deconvolution of FTIR peaks, the trial version OriginPro 2023 software was used [125], [126]. After extracting, in “.csv” format, the data processed by the SpectraGryph, was loaded into Excel, where the Eq. 2.1 was applied to the cells that contained the transmittance data, in order to convert it to absorbance [127].

$$Ab = 2 - \log_{10}(\%T) \quad (\text{Eq. 2.1})$$

The absorbance data obtained were loaded into the Origin software, where after selecting a data range ($1481\text{-}1747\text{ cm}^{-1}$) that included the characteristic zone of amide I ($1600\text{-}1700\text{ cm}^{-1}$), a Lorentzian band-shape was used to fit the contours. The curve-fitting algorithm creates Lorentzian bands that are added to produce a computed spectrum, which

is compared with the experimental one. The process is iterated until a satisfactory fit between the computed and experimental bands is obtained by a least square regression analysis. The calculated area of each sub band is reported as a percentage of the computed contour.

2.5.3. Differential Scanning Calorimetry and Thermogravimetric Analysis

To study the thermal characteristics of the samples, two types of thermoanalytical techniques were used: DSC and TGA.

DSC/TGA analyzes were performed using the thermal analyzer NETZSCH STA 449F3 (**Figure 2.1**). The samples were placed in aluminum crucibles and were subjected to heating from 25 °C to 250 °C at a rate of 5 K/min, under an atmosphere of nitrogen at a rate of 50 ml/min.



Figure 2.1 – Thermal analyzer NETZSCH STA 449F3.

2.5.4. Confocal Raman

Confocal Raman microscopy is a technique where we are provided with biochemical information, such as chemical composition and/or molecular interactions and structure, of the samples that are analyzed [87]–[90], [92], [95], [128], [129]. Therefore, it is widely used in the study of biomaterials [87], as well as in other areas where there is a need to study the chemical composition of materials [88], [129]. Raman spectroscopy

is complementary to infrared spectroscopy, since there are bands that are active in one of the techniques and not active in the other.

In **Figure 2.2**, a scheme of a confocal Raman microscope is shown and the confocal Raman microscope that was used.

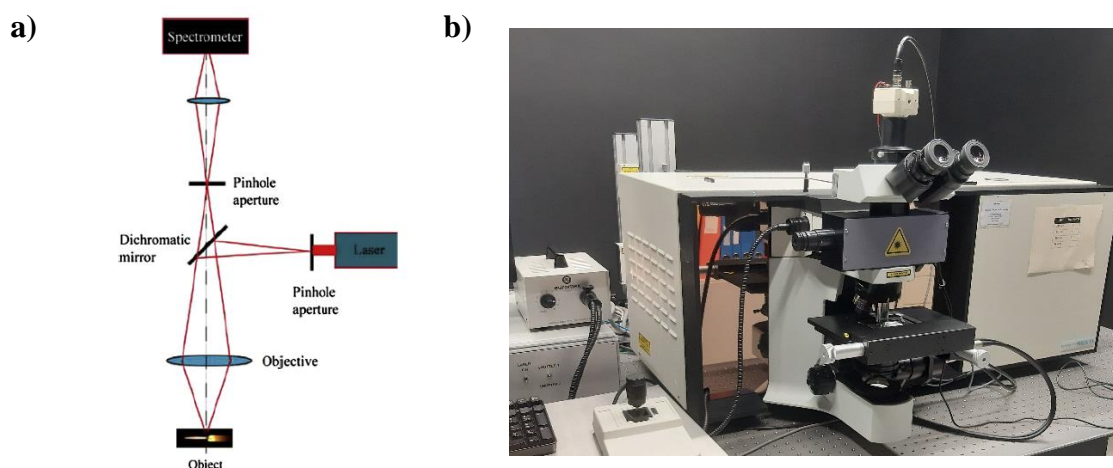


Figure 2.2 – Confocal Raman Microscopy: **a)** Setup of a Confocal Raman Microscope [93]; **b)** Confocal Raman Microscope LabRAM HR 800.

A LabRAM HR 800 confocal Raman microscope system (Horiba-JobinYvon) comprising a spectrometer and a fully integrated confocal microscope Olympus BX41 was used to characterize hydrated membranes. Raman spectra were generated using 515.2 nm laser diode as excitation source with an effective laser power of 6 mW, focused on the sample with a 100x (LWD) objective. The scattered light was dispersed by a grating with 1,800-lines/mm (Jobin–Yvon), and a thermoelectrically cooled charged coupled detector (CCD) camera recorded the spectra. The CCD was connected to a computer for data collection and analysis using Labspec software (Horiba JobinYvon, Lille, France). Spectral acquisitions were performed in 400–4000 cm^{-1} wavenumber range using the following conditions: exposure time 120 s, two accumulations, confocal pinhole 100 μm , spectral resolution 4 cm^{-1} .

Before performing any type of measurement, it was necessary to calibrate the equipment using a silicon sample. All analyses were conducted on membranes placed on aluminium foil wrapping a microscope glass slice, in order to enhance the signal to noise ratio. A drop of dH_2O was added to the samples in order to fix it better to the aluminium

foil since membranes are very light and could move during the analysis. The excess of water was removed with absorbing paper through capillarity.

2.5.5. Atomic Force Microscopy

To analyze the intended samples, they first had to be glued to a freshly cleaned mica sheet. Through the use of a PicoPlus scanning probe microscope interfaced with a Picoscan 5000 controller (Keysight Technologies, USA) and using the PicoView 1.20 software (Keysight Technologies, USA), connected to an inverted optical microscope (Observer Z1, Zeiss, Germany), AFM images were acquired. For measurements, the contact mode at RT, with a triangular tip (MLCT-BIO-DC probe, Bruker, USA) and a spring constant of 0.60 N/m were used. Scan speed was set at 0.5 Hz. Using the WsxM5.0 software, the roughness quantification and 3D images were performed [130].

2.5.6. Swelling ratio evaluation

Hydrogels are hydrophilic polymers of three-dimensional networks that have a finite capacity to absorb water [131]–[133], physiological solutions or even saline solution [132]. The swelling power of hydrogels is what makes them useful for biomedical, industrial and pharmaceutical applications, and they can be used for example in the creation of controlled drug release devices [132], [134]. The swelling ratio is determined by the increase in weight of the hydrogel due to the absorption of water or other solvent [135].

To determine the swelling ratio (Sr) of the lyophilized membranes, the following equation was used Eq. 2.2 [134], [136].

$$Sr = \frac{M_s - M_d}{M_d} \quad (\text{Eq. 2.2})$$

where, M_s is the mass of the swollen sample and M_d is the mass of the dry sample [134], [136].

To calculate the swelling ratio of the intended samples, first, the completely dry membranes had to be weighed, then they were placed in dH_2O , with a volume 10 times the sample weight, for 10 min. The excess of dH_2O was removed by capillarity and the weight of the hydrated samples were determined again.

2.5.7. Zeta Potential

The evaluation of the Zeta potential was possible through flow measurements using a commercial electrokinetic analyzer (EKA) (Anton Paar GmbH, Austria) and a special powder cell fitted inside a cylindrical, which is used for particles (**Figure 2.3 b**).

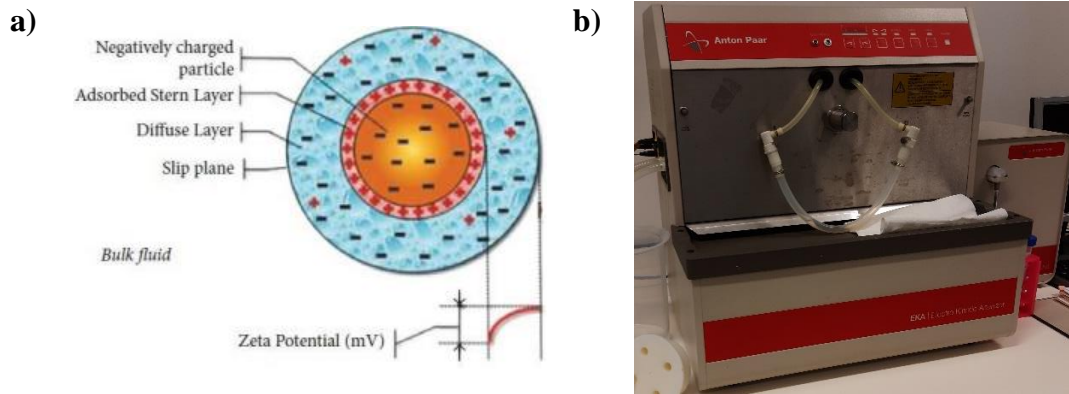


Figure 2.3 – Zeta Potential: **a)** Graphical illustration of zeta potential value [137]; **b)** Electrokinetic analyzer Anton Paar GmbH.

With the aid of the powder cell, the solid particles were assembled inside it, occupying a total volume of approximately 48.75 mm^3 , thus preserving a constant overall height of the sample during the determination of all measurements performed. With the use of Ag/AgCl electrodes, placed at both ends of the streaming channel – the cylindrical cell, the streaming potential was determined. A 1 mM KCl solution was used as the electrolyte with the pH ranging between 6.13 and 7.23. Measurements were performed at about $24.60 \text{ }^\circ\text{C}$. During the tests, the conductivity of the electrolyte solution was measured. With the application of an electrolyte flow, in alternate directions, and pressure ramps from 0 to 200 mbar, the flow potential was measured. For each test, 12 pressure ramps were performed (6 in each flow direction in order to deal with asymmetric potential fluctuations).

2.5.8. Rheological Tests

Rheological studies were performed on the spongy layer hydrated samples using the Kinexus Pro rheometer (Malvern Instruments, Malvern, UK, **Figure 2.4**).

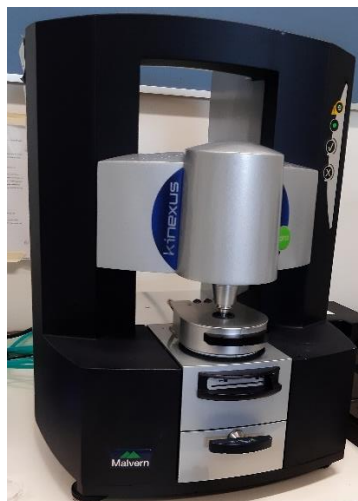


Figure 2.4 – Kinexus Pro rheometer.

The analyzes were carried out in a water-vapor saturated environment, at a temperature of 25 °C, parameters guaranteed by the rheometer chamber. Parallel plate geometries were used to perform the oscillatory measurements. In order to determine the linear viscoelastic region (LVR) of the analyzed samples, it was necessary to use Ø 8 mm sandblasted parallel plate geometries, which, in turn, compress the samples, in a range of oscillatory measurements, where frequency sweep and strain amplitude sweep measurements were repeatedly performed.

Frequency sweeps were performed, with a fixed shear stress of 1 %, in a range from 0.01 to 100 Hz and amplitude sweeps, with a fixed frequency of 1 Hz, in a range from 0.01 to 100 %.

CHAPTER 3 – RESULTS AND DISCUSSION

3. Results and Discussion

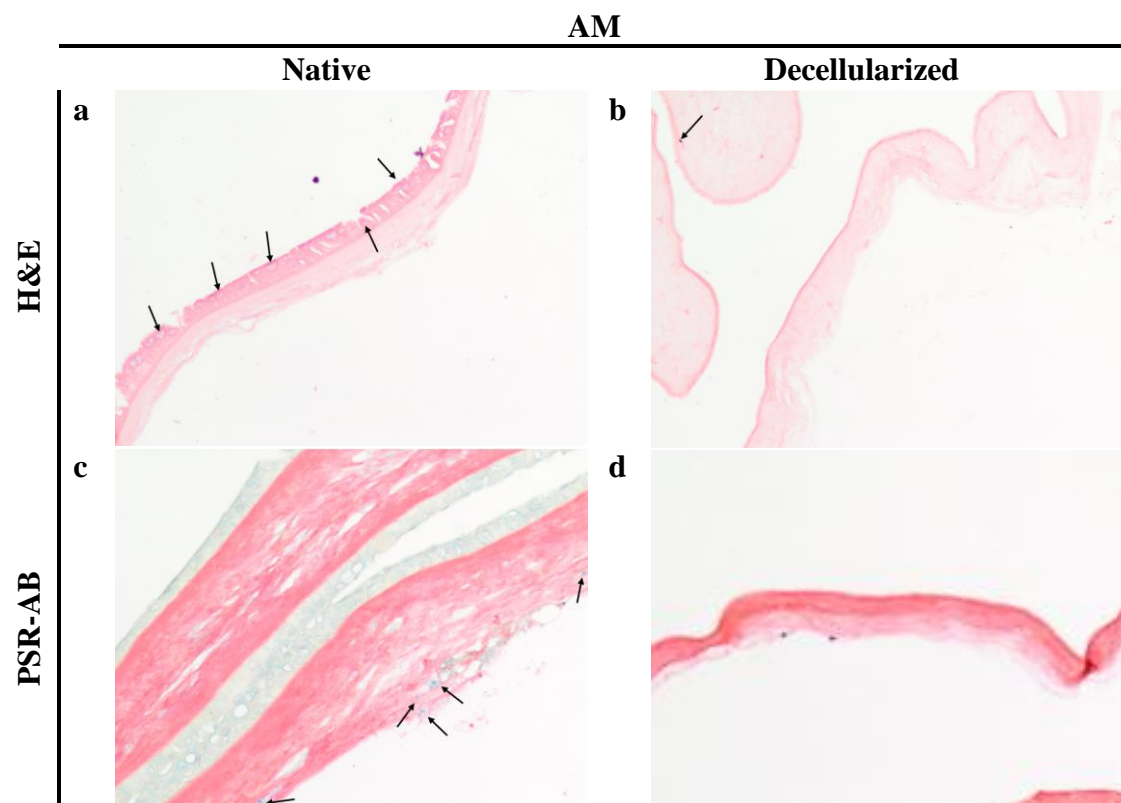
3.1. Membrane's decellularization results

3.1.1. Histological analysis

Histological analysis of Amniotic Membrane

In the following table, **Table 3.1**, we can observe the light microscope images of AM stained samples before and after decellularization using the improved protocol.

Table 3.1 – Micrographic images of stained Amniotic membranes.



By observing the structures of interest in the membranes it is possible to verify that the decellularization method was effective and didn't cause damage to the membranes structure.

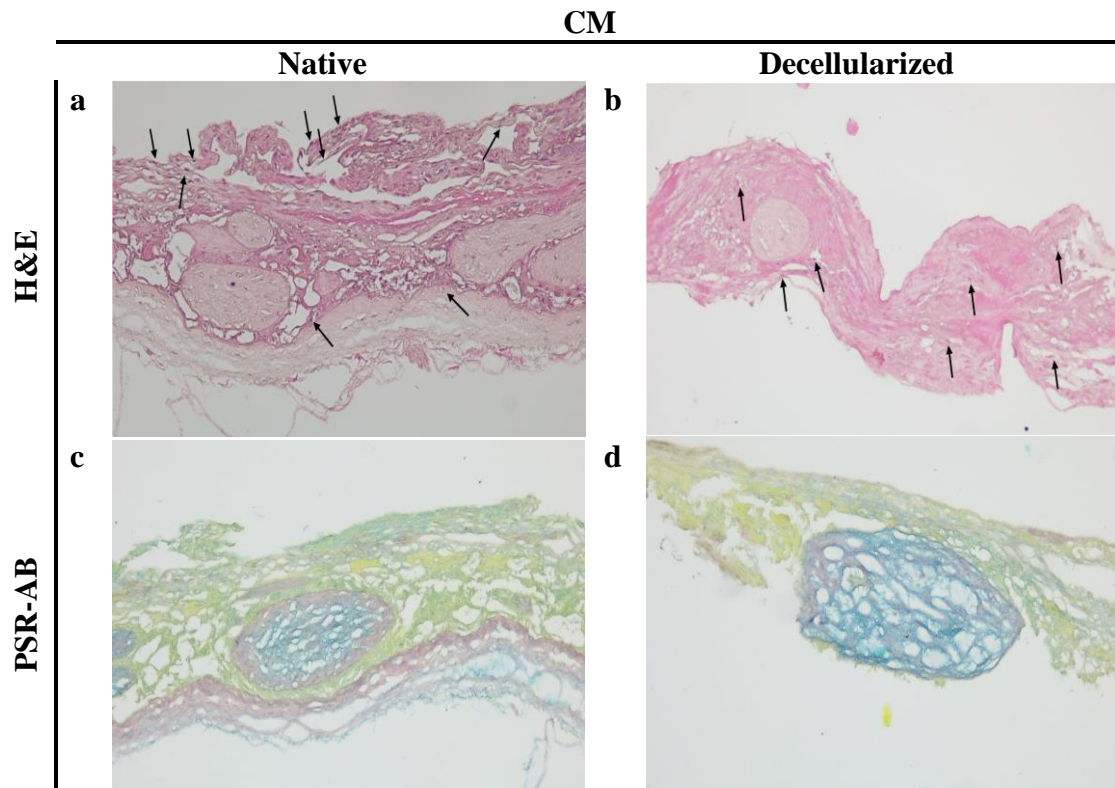
The H&E staining method, allows to identify and distinguish basophils from acidophiles. **Fig. a**, shows a membrane that has not undergone the decellularization

process (native membrane). The arrows point out some of the identified basophils, which in turn were stained by hematoxylin with blue color [114]–[116]. We can also observe that the epithelium is slightly damaged, possibly due to the freezing and unfreezing process to store and subsequently analyze the membranes. In **fig. b**, we can verify that a single basophil remained, an AMSC, marked by the arrow. It is possible to identify the type of cell, because the membrane, after being decellularized, has no epithelial layer and in the amnion, there are only 2 types of cells, the AECs and the AMSCs, being basophils found in the fibroblast layer [3]. In both figures, all basic membrane components, the acidophiles, present in the cytoplasm were stained with a pink color by eosin [114]–[116].

In the PSR-AB staining method, **fig. c**, the arrows indicate the components (GAG's or glycoproteins) that were stained by the alcian blue dye [120]. The alcian blue also stained components on the epithelial layer. The picro-sirious network stains almost all layers of AM, those containing collagen, with a pink color [117]–[119], whereas the epithelium and compact layer aren't stained because they do not have collagen in their composition [1]. In **fig. d**, there are no components stained by alcian blue, which means that these were lost during decellularization. In **fig. d**, an amnion layer with a stronger pink tone is observed, which is the basement membrane. This intense color is due to the presence of various types of collagen in this layer [1], [24], [33]. The stronger pink layer is also present in **fig. c**, but it isn't as noticeable because the native membrane still has the epithelial layer.

Histological analysis of Chorionic Membrane

On **Table 3.2**, we can observe the light microscope images of CM stained samples, before and after decellularization using the improved protocol.

Table 3.2 – Micrographic images of stained Chorionic membranes.

The histology results show that the macrostructure of the chorionic membrane is very damaged (**fig. b** and **fig. d**). This is possibly do to the pre-processing of the membrane since the scratching of the placenta to separate the amniotic and chorionic membranes is quite an aggressive procedure. No such damaged was observed for the amniotic membrane (**fig. a** and **fig. c**). Also, in opposition to what happened with the amniotic membrane, the chorionic membrane was not completely decellularized.

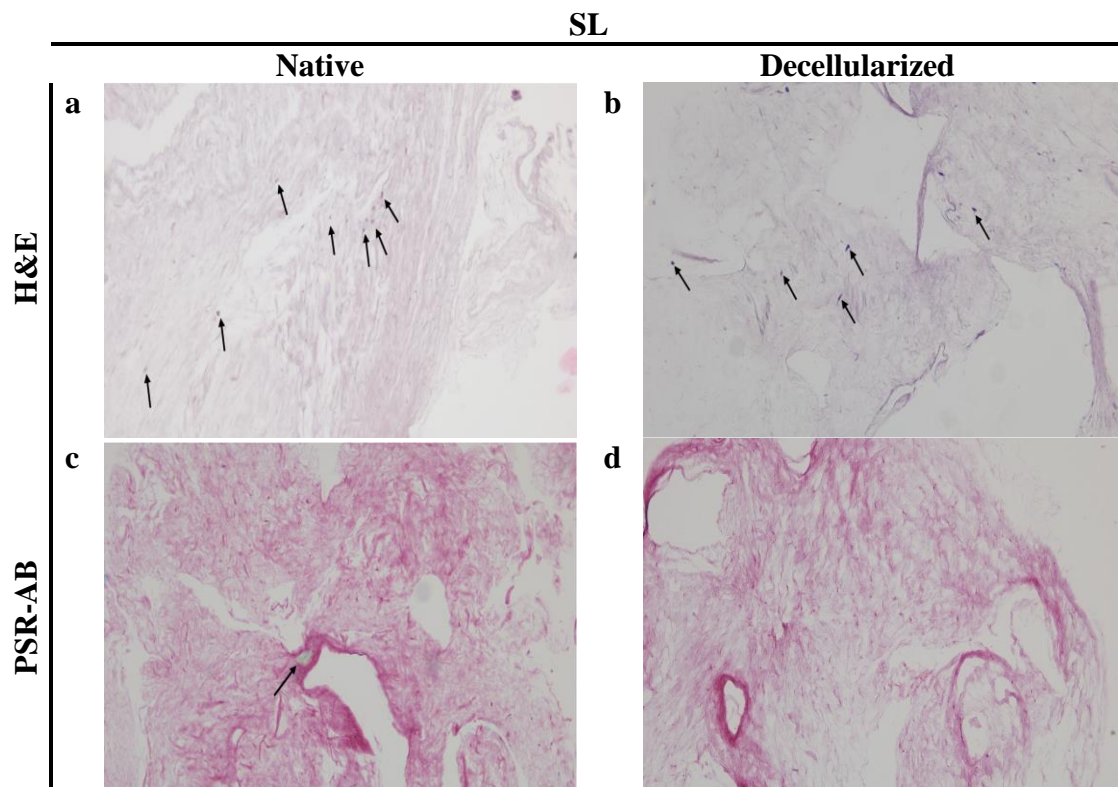
In the native chorionic membrane (**fig. a**), a large number of basophils are identified, indicated by arrows, through their bluish color caused by hematoxylin staining [114]–[116]. It would be expected that, having undergone the decellularization process, this membrane would be free of basophils, but this didn't happen. In **fig. b** it is possible to observe some basophils that remained in the membrane after the decellularization process (the arrows are pointing out only a small number of them). In the two figures, **fig. a** and **fig. b**, the other membrane components, the acidophiles, were stained by eosin with a pink color [114]–[116].

In **fig. c** and **fig. d** we can observe the native chorionic membrane and the decellularized chorionic membrane respectively, stained with PSR-AB. The native membrane contains a large amount of GAG's stained by the alcian blue dye [120]. In the same figure, collagen is colored pink by picro-sirious [117]–[119]. In **fig. d**, we can still observe GAG's, which means that they weren't completely eliminated from the membrane during the decellularization process. In **fig. c** and **fig. d** there are also other components stained with a green color, that aren't collagen or GAG's, are components that aren't stained by de picro-sirious or alcian blue.

Histological analysis of Spongy layer

On the **Table 3.3**, we can observe the light microscope images of spongy layer stained samples, before and after decellularization, using the base protocol. The optimized protocol was not tested with the spongy layer due to the small quantity of membrane available.

Table 3.3 – Micrographic images of stained Spongy Layer membrane.



With the H&E staining method, it is possible to observe that the native spongy layer, **fig. a**, has small nuclei (basophils), some of which are indicated by arrows, which have a bluish color caused by hematoxylin [114]–[116]. As with the amniotic membrane, it would be expected that the spongy layer, after decellularization would be free of nuclei, but what the H&E staining shows, **fig. b**, is that some basophils remained, indicated by arrows, despite being in a less number than those shown in the native spongy layer. In **fig. a**, acidophiles are colored pink by eosin [114]–[116], which isn't the case in **fig. b**. In the decellularized spongy layer, what would be the acidophiles are colored to more purple tones, indicating that the decellularization protocol have eliminated acid components present in this layer [114]–[116].

Fig. c and **fig. d** show the native and decellularized spongy layers stained with PSR-AB. According to the literature, in addition to other components, the spongy layer is made up of a non-fibrillar collagen type III network, an abundance of glycoproteins and proteoglycans, mainly hyaluronic acid [3], [35], which are stained with PSR-AB [117]–[120]. However, when analyzing **fig. c**, it is observed that in this layer there were few GAG's present, pointed out by arrows, with a bluish color caused by the alcian blue staining [120]. Additionally, everything else in the figure is colored pink by picro-sirious, which means that there is collagen present [117]–[119]. In **fig. d**, no elements with a bluish color were found, which means that the few GAG's this layer contained were eliminated by the decellularization process.

The remaining components that make up this layer, such as fine fibrils surrounded by mucus [1], Hofbauer cells, and some isolated fibroblast [34] are stained in a greenish color but appear in small quantities. The results obtained suggest that possibly this membrane was not collected in the ideal conditions justifying this lack of GAG's and other membrane characteristic components.

Further histology images of the stained membranes scan be observed in Annex B.

3.1.2. FTIR spectroscopy

The ATR-FTIR spectroscopy data obtained using was processed (correcting its baseline and labeling of the peaks) using the SpectraGryph software.

The use of the ATR-FTIR tool is advantageous for the study of the structure and chemical composition of tissues [80], [138] since no sample preparation is needed.

By observing the FTIR spectra of the 3 native membranes (**Figure 3.1**), we can see they are very similar, since their main constituent is collagen, differing in very specific areas namely, in the wave number range $1350\text{-}850\text{ cm}^{-1}$.

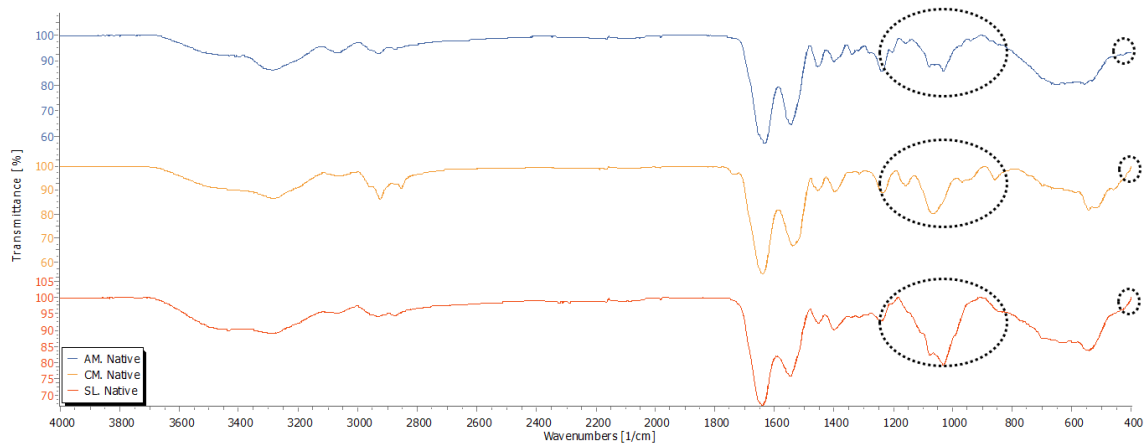


Figure 3.1 – FTIR spectra of native membranes.

The FTIR spectra of each membrane, when submitted to different decellularization protocols, were analyzed in more detail, as follows.

FTIR spectroscopy of Amniotic Membrane

Figure 3.2. shows the the FTIR spectra of the native amniotic membrane and of the decellularized membranes using the two decellularization protocols.

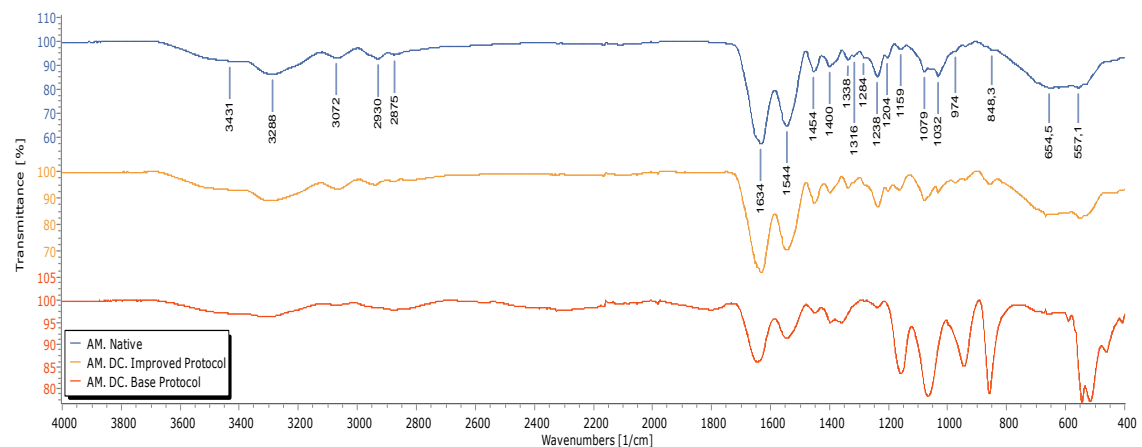


Figure 3.2 – FTIR spectra of amniotic membrane: AM Native; Amniotic membrane decellularized using improved protocol; Amniotic membrane decellularized using base protocol.

It was observed that the native amniotic membrane and the AM DC using the improved protocol, exhibit a similar spectra pattern, differing only in the peak intensities, indicating that the decellularization process didn't cause drastic changes in the functional groups of the analyzed samples. The spectrum of the sample decellularized by the base protocol differs, not only in the intensity of the peaks, but also in the absence of some of them. The base protocol seems to negatively affect the decellularized samples, causing them to lose structural components.

The AM spectra, obtained by ATR-FTIR, present the 5 characteristic bands of proteins [80], [139], which are originated by the vibrations of the atoms related to the peptide bonds [139], three of which are known as amide bands. The 5 characteristic bands, constituted by amide I, amide II, amide III, amide A and amide B, have slightly different positions in the 3 spectra. In the spectrum of the native amniotic membrane the 5 bands are found at the following positions: amide I (1634 cm^{-1}), amide II (1544 cm^{-1}), amide III (1238 cm^{-1}), amide A (3288 cm^{-1}) and amide B (2930 cm^{-1}). In AM DC by the improved protocol, the 5 bands present the following positions: amide I (1633 cm^{-1}), amide II (1544 cm^{-1}), amide III (1237 cm^{-1}), amide A (3289 cm^{-1}) and amide B (2941 cm^{-1}). Finally, in AM DC by the base protocol we have: amide I (1646 cm^{-1}), amide II (1548 cm^{-1}), amide III (1238 cm^{-1}), amide A (3315 cm^{-1}) and amide B (2939 cm^{-1}). The position of the characteristic bands of the AM DC spectrum using the base protocol, when compared with the native AM spectrum differs more, than the AM DC spectrum using the improved protocol, suggesting that the base protocol affects more the membrane structure/composition than the improved protocol.

The band of amide I is the most intense one and is attributed to the C=O stretching vibrations of the carboxylic group [80], [81], [140]–[142] coupled weakly with N-H bending vibrations [80], [142]. The amide II is mainly derived from the C-N stretching along with N-H in-plane bending [80], [140] and C-C-N deformation or else, it is associated with vibrations of hydrogen paired with COO⁻ in the peptide bonds [140]. The C=O stretching vibrations present hydrogen bonds with the N-H group of peptide bonds of the chains that are closer [140]. It is the hydrogen bonds that provide stability to the secondary structure of the protein, present in the collagen molecule [139], [140]. This band is normally found between the wavenumbers $1640\text{--}1690\text{ cm}^{-1}$, but it can be located

in lower wavenumbers, due to the presence of hydrogen bonds, the lower the wavenumber, the more hydrogen bonds it has [10], [139] and therefore a lower degree of molecular order [10]. The amide I band is the most used for the study of the secondary structure of proteins [80], [140], because its exact location is determined by the pattern in which the hydrogen bonds are found within the protein molecule and by the conformation of its backbone. The conformational sensitivity of this band and the way the molecule interacts with infrared light is related to its hydrogen bonds and bonds between the transition dipoles, both intra and intermolecular [80].

The amide II band is located at 1500–1600 cm^{-1} and originates from the N-H bending mode and the C-N stretching mode [81], [141], [142], as does the amide III band [10], [139] and is linked to the triple helix structure of collagen. In the 3 analyzed samples, this band presented values lower than 1550 cm^{-1} , typical of hydrogen bonds, which means that the 3 samples have a similar secondary structure [140].

The amide III band, which can usually be found between the wavenumbers 1300-1200 cm^{-1} [80], [142] is the result of the complex combination of the stretching vibrations of the C-N bond in conjunction with the vibration of the N-H bond plane and also with the stretching vibrations of the C-C bond and the bending of the C=O bond [81], [141].

The amide A band is associated with the N-H stretching bonds of the peptide bonds [10], [139], [140]. Previous studies have shown that this band should occur in the wavenumber region between 3400-3440 cm^{-1} , however if the N-H stretching bond is coupled with hydrogen bonds, this band can be found at lower wavenumbers lower [10], [139], around $\sim 3200 \text{ cm}^{-1}$ [10]. As in all analyzed samples this band is below this wavenumber range, it means that there are hydrogen atoms involved in the N-H stretching bonds.

The amide B bands are bands of low intensity, with asymmetric stretching of C-H bonds, CH_2 (methylene groups) [139], [140], which occurs at approximately 2962 cm^{-1} [140].

In the following table, **Table 3.4**, the assignment of each of the points of the native amniotic membrane is summarized.

Table 3.4 – Assignment of each peak in the FTIR spectrum of Native Amniotic Membrane.

| <i>Native Amniotic Membrane</i> | | | |
|-------------------------------------|---------------|--|---------------------------------------|
| <i>Wavenumber (cm⁻¹)</i> | <i>Region</i> | <i>Assignment</i> | <i>References</i> |
| 1238 | Amide III | Mixing of the stretching vibrations of the C-N bond with the vibration of the N-H bond plane and with the stretching vibrations of the C-C bond and bending of the C=O bond | [10], [81], [138]–[140], [142], [143] |
| 1284 | - | Nucleic acids and phosphor-lipids | [81] |
| 1338 | - | CH ₂ Swing | [10] |
| 1400 | - | Carboxylate ion and C=O planar deformation | [141] |
| 1454 | - | C-N stretch vibrations, paired with N-H deformations of amide bonds and C-H of the CH ₂ group of the proline side chains and the glycine backbone | [139], [140] |
| 1544 | Amide II | N-H bending mode coupled with C-N stretching mode | [80], [139], [142] |
| 1634 | Amide I | C=O stretching vibrations of the carboxylic group paired with N-H bending vibrations, C-N stretching and C-C-N deformation or else, it is associated with vibrations of hydrogen paired with COO ⁻ in the peptide bonds | [10], [80], [139], [142] |
| 2875 | - | Aliphatic C-H stretching | [142] |
| 2930 | Amide B | Asymmetric stretching of C-H bonds and aliphatic C-H stretching | [10], [138], [139], [142] |
| 3288 | Amide A | N-H stretching bonds of peptide bonds coupled with hydrogen bonds, O-H and C-H bending vibrations | [13], [141] |
| 3431 | - | Hydroxyl groups, O-H, resulting from water molecules | [13] |

In order to evaluate the structural changes that may have occurred in the collagen matrix of the membranes during the decellularization process, it was necessary to proceed with the computational processing of the FTIR spectra was performed [81], [141] (**Figure 3.3**). The amide group vibrations of protein backbones is of particular interest, since they are present in all proteins and provide information on protein secondary conformation.

Although all the three amide bands can be useful to elucidate the secondary structure of a protein, the Amide I band is the most sensitive to structural changes and is the most commonly used in secondary structure analysis. There are several factors that are responsible for the conformational sensitivity of the Amide I band including hydrogen bonding and coupling between transition dipoles, both inter and intra molecular, which will significantly influence the way in which a protein molecule interacts with IR light [80].

The FTIR spectroscopic characteristics are composed of a set of thousands of unique spectra, among which the synergistic participation of sugars, nucleic acids, proteins and lipids are part [81], [141]. The band representing amide I, where the vibration of the C=O stretch is located, is quite sensitive to the protein folding [81], so this band is where the most relevant structural changes are located, and is used to estimate the quantities and types of secondary structure that are present [80], [81], [141]. The changes in the secondary structure are observed in the amide I band, namely α -helix (1659 cm^{-1}), β -sheets (1628 cm^{-1}), turns (1678 cm^{-1}), unordered or random coil contributions (1646 cm^{-1}) and side chains (1613 cm^{-1}) [81], [141].

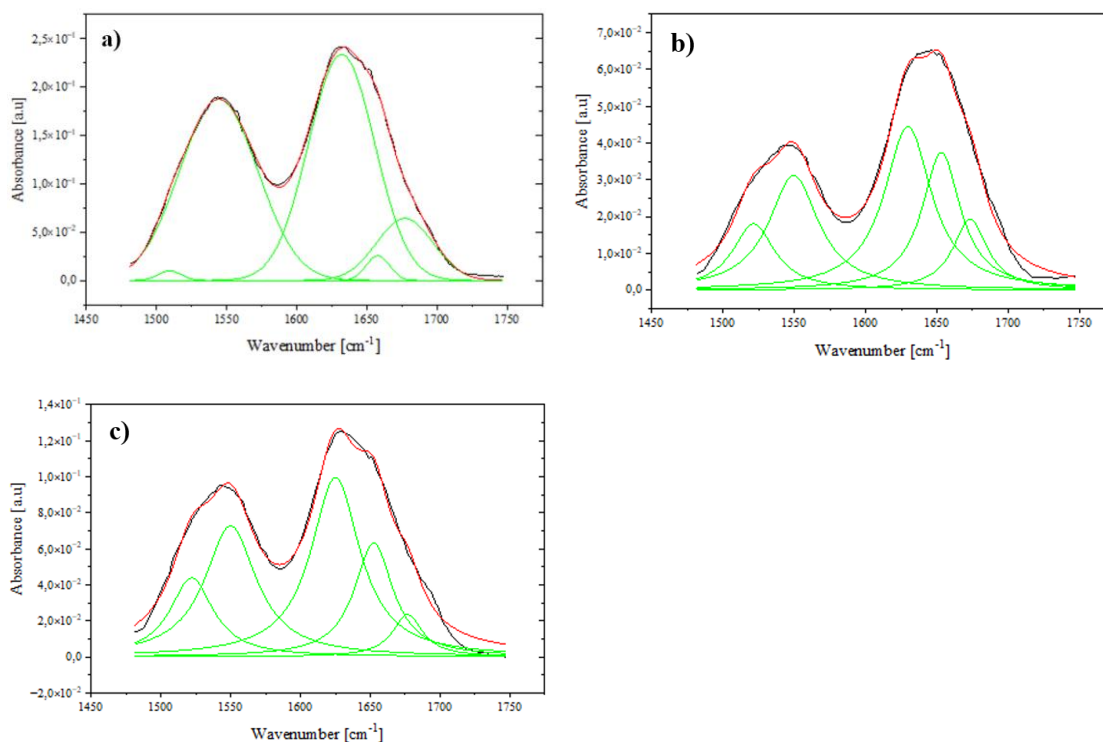


Figure 3.3 – Computational fitting of the amide I FTIR spectroscopy absorption band: **a)** AM Native; **b)** AM. DC. Base Protocol; **c)** AM. DC. Improved protocol.

By observing the deconvoluted spectra presented in **Figure 3.3**, we see that the ones corresponding to samples that went through the decellularization process, **b)** and **c)**, are practical identical, which may indicate that both protocols affected the secondary structure of the proteins in the same way. The position of the bands of amide I related to the secondary structures of proteins concerning the graphs on **Figure 3.3**, are shown in the following table, (**Table 3.5**).

Table 3.5 – Characteristic protein secondary structure amide I bands of Amniotic Membranes.

| | <i>α-helix</i> | <i>β-sheets</i> | <i>turns</i> |
|----|----------------------------------|----------------------------------|-------------------------|
| a) | 1658.0 cm ⁻¹ | 1632.1 cm ⁻¹ | 1677.2 cm ⁻¹ |
| b) | 1653.1 cm ⁻¹ | 1629.7 cm ⁻¹ | 1673.4 cm ⁻¹ |
| c) | 1652.5 cm ⁻¹ | 1625.1 cm ⁻¹ | 1676.8 cm ⁻¹ |

The differences observed in the position of the bands indicate that changes have occurred in the secondary structure of the proteins, nevertheless being the values obtained in a range that is in accordance with the literature [81], [141].

FTIR spectroscopy of Chorionic Membrane

The same study using FTIR spectroscopy was performed for the chorionic membrane, **Figure 3.4**.

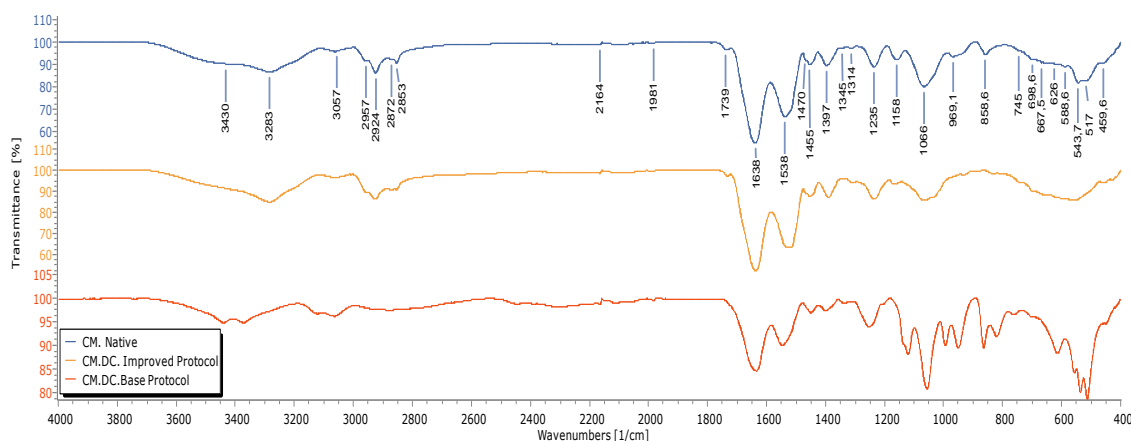


Figure 3.4 – FTIR spectra of chorionic membrane: CM Native; Chorionic membrane decellularized by improved protocol; Chorionic membrane decellularized by base protocol.

Again, it is possible to observe a greater similarity between the spectrum of the native chorionic membrane and the CM DC using the improved protocol, than with the CM DC using the base protocol, although some differences in the intensity of the peaks is observed. Additional peaks arise in the CM DC spectrum using the base protocol. These observations suggest that the improved protocol is more beneficial for the conservation of membrane characteristics and properties.

Like the amniotic membrane, the chorionic membrane is essentially a collagen tissue, and as such, its FTIR spectra includes the 5 amide characteristic bands of this type of tissue (**Figure 3.4**) [80], [139] in the following positions: amide I (1638 cm^{-1}), amide II (1538 cm^{-1}), amide III (1235 cm^{-1}), amide A (3283 cm^{-1}) and amide B (2924 cm^{-1}). In CM DC by the improved protocol, the 5 bands present the following positions: amide I (1637 cm^{-1}), amide II (1517 cm^{-1}), amide III (1235 cm^{-1}), amide A (3284 cm^{-1}) and amide B (2926 cm^{-1}). Finally, in CM DC by the base protocol they present the positions: amide I (1635 cm^{-1}), amide II (1548 cm^{-1}), amide III (1252 cm^{-1}), amide A (3373 cm^{-1}) and it appears that the amide B band doesn't exist. As mentioned before, the spectrum of CM DC by the base protocol is less similar to the native spectrum, than the spectrum of CM DC by the improved protocol due possibly to the fact of being more harmful to the membrane, which is evidenced by the absence of one of the characteristic bands of collagen, the amide B.

The assignment of each band of the native chorionic membrane is summarized in **Table 3.6**.

Table 3.6 – Assignment of each peak in the FTIR spectrum of Native Chorionic Membrane.

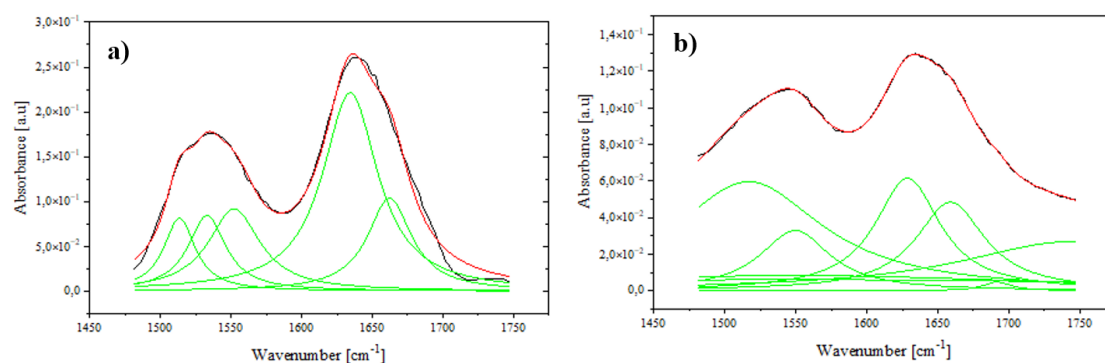
| <i>Native Chorionic Membrane</i> | | | |
|---|---------------|--|---------------------------------------|
| <i>Wavenumber (cm^{-1})</i> | <i>Region</i> | <i>Assignment</i> | <i>References</i> |
| 626 | - | Carboxylate ion and C=O planar deformations | [141] |
| 1235 | Amide III | Result from N-H stretching and C-N in plane bending and is attributed to the phospholipids, glycolipids, and phosphodiester group of nucleic acids | [80], [81], [138], [140], [142]–[144] |

Cont.

Cont...

| | | | |
|------|----------|---|--------------|
| 1397 | - | Carboxylate ion and C=O planar deformations | [141], [144] |
| 1455 | - | C-H bending modes | [141] |
| 1538 | Amide II | N-H bending mode coupled with C-N stretching mode | [80] |
| 1638 | Amide I | C=O stretching vibrations of the carboxylic group paired with N-H bending vibrations | [80], [142] |
| 2853 | - | Aliphatic C-H stretching | [142] |
| 2872 | - | Aliphatic C-H stretching | [142] |
| 2924 | Amide B | Asymmetric stretching mode of CH ₃ Group and aliphatic C-H stretching | [142], [144] |
| 2957 | - | Aliphatic C-H stretching | [142] |
| 3283 | Amide A | N-H stretching bonds of peptide bonds coupled with hydrogen bonds, O-H and C-H bending vibrations | [13], [141] |
| 3430 | - | Hydroxyl groups, O-H, resulting from water molecules | [13] |

As with AM, to estimate the structural changes that may have occurred in the collagen matrix of the chorionic membranes during the decellularization process, it was necessary to proceed to the deconvolution of amide I region [81], [141], **Figure 3.5**.



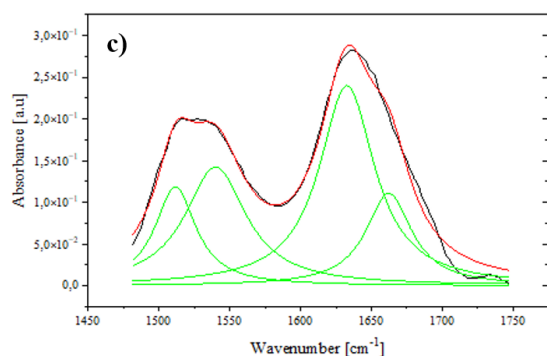


Figure 3.5 – Computational fitting of the amide I FTIR spectroscopy absorption band: **a)** CM Native; **b)** CM. DC. Base Protocol; **c)** CM. DC. Improved protocol.

Contrary to what was observed concerning the amniotic membrane, the obtained results for the native chorionic membrane, **a)**, and for the membrane decellularized by the improved protocol, **c)**, are more similar. Therefore, this membrane also doesn't present the five secondary structures of the amide I proteins, as would be expected. The position of the bands of amide I related to the secondary structures of proteins concerning the graphs of **Figure 3.5** are indicated in **Table 3.7** and are in accordance with the literature [81], [141].

Table 3.7 – Characteristic protein secondary structure amide I bands of Chorionic Membrane.

| | <i>α-helix</i> | <i>β-sheets</i> | <i>turns</i> |
|-----------|----------------------------------|----------------------------------|-------------------------|
| a) | 1662.3 cm ⁻¹ | 1634.4 cm ⁻¹ | - |
| b) | 1659.0 cm ⁻¹ | 1628.7 cm ⁻¹ | 1691.9 cm ⁻¹ |
| c) | 1662.3 cm ⁻¹ | 1632.8 cm ⁻¹ | - |

We can verify that in both spectra of the native membrane, **a)**, and the membrane decellularized by the improved protocol, **c)**, the characteristic band of the turns secondary structure is not observed and, in the membrane decellularized by the base protocol, **b)**, it exists. The decellularization protocols seem to affect more the secondary structure of proteins present in the chorionic membrane, than the ones present in the amniotic membrane.

FTIR spectroscopy of Spongy Layer

Like as the other two membranes, the spongy layer was characterized by FTIR spectroscopy (**Figure 3.6.**).

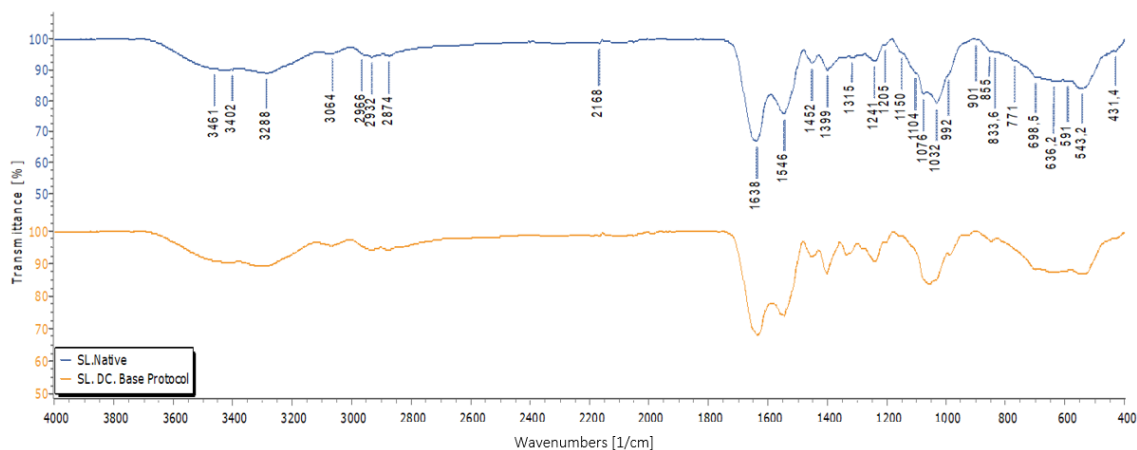


Figure 3.6 – FTIR spectra of spongy layer: SL Native; spongy layer decellularized by base protocol.

Due to the small quantity of lyophilized spongy layer available, only the base protocol was used to decellularize it. The spectra of the native and decellularized samples are very similar (**Figure 3.6.**), differing in the relative intensities of the bands and in the lack of some peaks in the zone between the 1150 and 1000 cm^{-1} .

As in the two previously studied membranes, the spongy layer contains collagen and therefore presents the 5 characteristic bands of collagen [80], [139]. These characteristic bands have different positions depending on the spongy layer being decellularized or not. In the SL native spectrum, the following bands can be observed: amide I (1638 cm^{-1}), amide II (1546 cm^{-1}), amide III (1241 cm^{-1}), amide A (3288 cm^{-1}) and amide B (2932 cm^{-1}). In SL DC by Base Protocol, we have: amide I (1637 cm^{-1}), amide II (1546 cm^{-1}), amide III (1240 cm^{-1}), amide A (3302 cm^{-1}) and amide B (2934 cm^{-1}).

The assignment of each band of the native spongy layer is summarized in the **Table 3.8.**

Table 3.8 – Assignment of each peak in the FTIR graph of Native Spongy Layer.

| <i>Native Spongy Layer</i> | | | |
|---|---------------|--|---|
| <i>Wavenumber (cm⁻¹)</i> | <i>Region</i> | <i>Assignment</i> | <i>References</i> |
| 1104 | - | Glyco- and phospho-lipids and phosphodiester group of nucleic acids | [81], [141] |
| 1241 | Amide III | Result from N-H stretching and C-N in plane bending and is attributed to the phospholipids, glycolipids, and phosphodiester group of nucleic acids | [10], [13], [80], [138]–[143] |
| 1399 | - | C=O planar deformation and carboxylate ion | [141], [144] |
| 1452 | - | C-H bending modes and pyrrolidine rings of the amino acid proline | [13], [139], [141], [144] |
| 1546 | Amide II | N-H bending mode coupled with C-N stretching mode | [10], [13], [80], [81], [138], [139], [141]–[144] |
| 1638 | Amide I | C=O stretching vibrations of the carboxylic group paired with N-H bending vibrations | [13], [80], [142] |
| 2874 | - | Aliphatic C-H stretching | [142] |
| 2932 | Amide B | Asymmetric stretching mode of CH ₃ Group and aliphatic C-H stretching | [139], [142] |
| 2966 | - | Aliphatic C-H stretching | [142] |
| 3288 | Amide A | N-H stretching bonds of peptide bonds coupled with hydrogen bonds, O-H and C-H bending vibrations | [13], [141] |
| 3402 | - | Asymmetric stretching vibration of free N-H and O-H from the water molecule | [10], [13], [140] |
| 3461 | - | Hydroxyl groups, O-H, resulting from water molecules | [13] |

As with the other membranes, to estimate the secondary structure of the collagen matrix of the spongy layer before and after the decellularization process, amide I zone was deconvoluted (**Figure 3.7**) [81], [141].

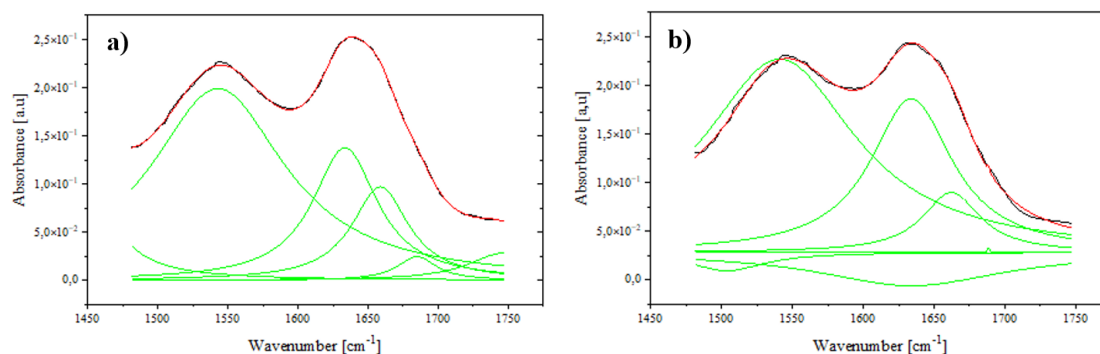


Figure 3.7 – Computational fitting of the amide I FTIR spectroscopy absorption band: **a)** SL Native; **b)** SL. DC. Base Protocol.

The data concerning the deconvolution of the amide I zone is very similar for both membranes, the decellularized and the non-decellularized one. As observed with the other two membranes, the spongy layer only present three types of secondary structure of proteins (**Table 3.9**), being the positions of the characteristic bands of the secondary structure of proteins similar to what is described in the literature [81], [141].

Table 3.9 – Characteristic protein secondary structure amide I bands of Spongy Layer membrane.

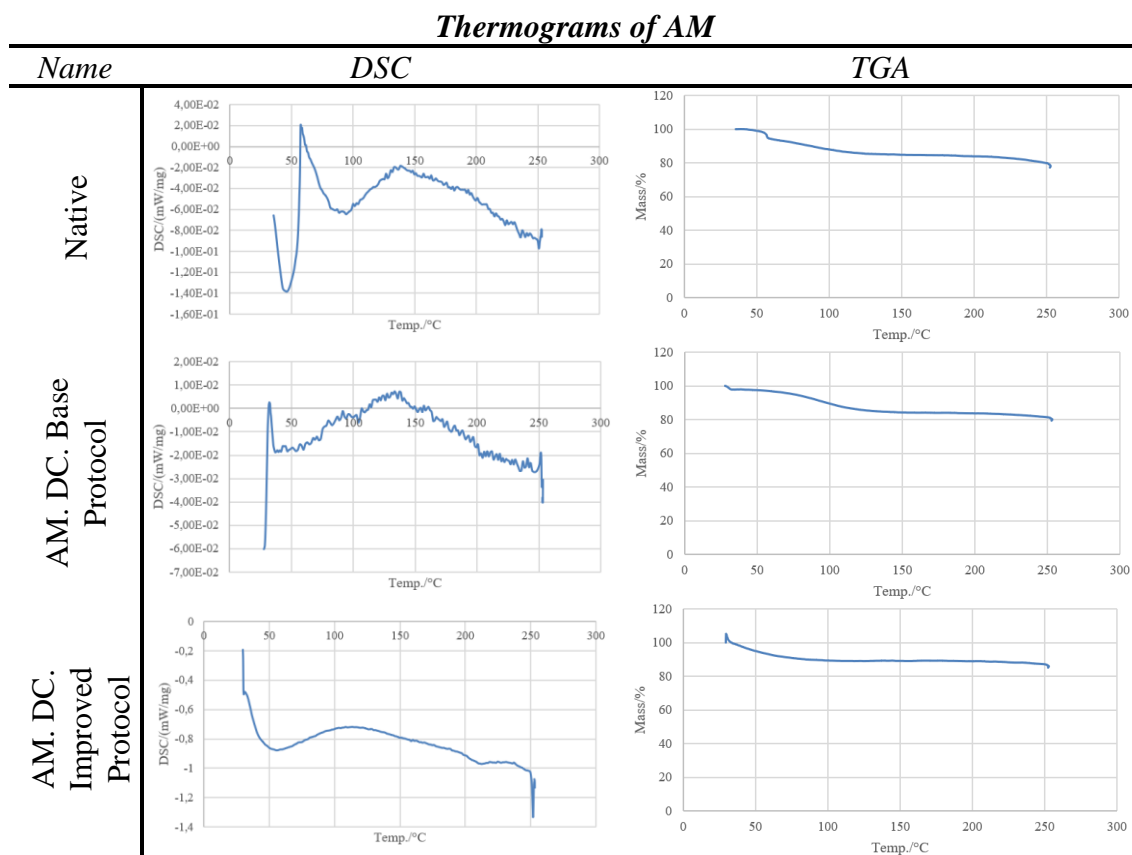
| | <i>α-helix</i> | <i>β-sheets</i> | <i>turns</i> |
|-----------|----------------------------------|----------------------------------|-------------------------|
| a) | 1658.8 cm ⁻¹ | 1633.5 cm ⁻¹ | 1685.0 cm ⁻¹ |
| b) | 1662.3 cm ⁻¹ | 1634.0 cm ⁻¹ | 1688.5 cm ⁻¹ |

Complementary FTIR spectra of the membranes are presented in Annex C.

3.1.3. Differential Scanning Calorimetry

DSC/TGA of Amniotic Membrane

Table 3.10. shows the thermograms of the amniotic membranes, native and decellularized, using both protocols in study.

Table 3.10 – Thermograms of AM obtained through two different protocols.

Through the DSC graphs, we can observe that the protocol that presents less differences for the native membrane is the base protocol. The graphs of native membrane and AM. DC. by base protocol have a lot of noise, which couldn't be eliminated by the software's own smoothing techniques.

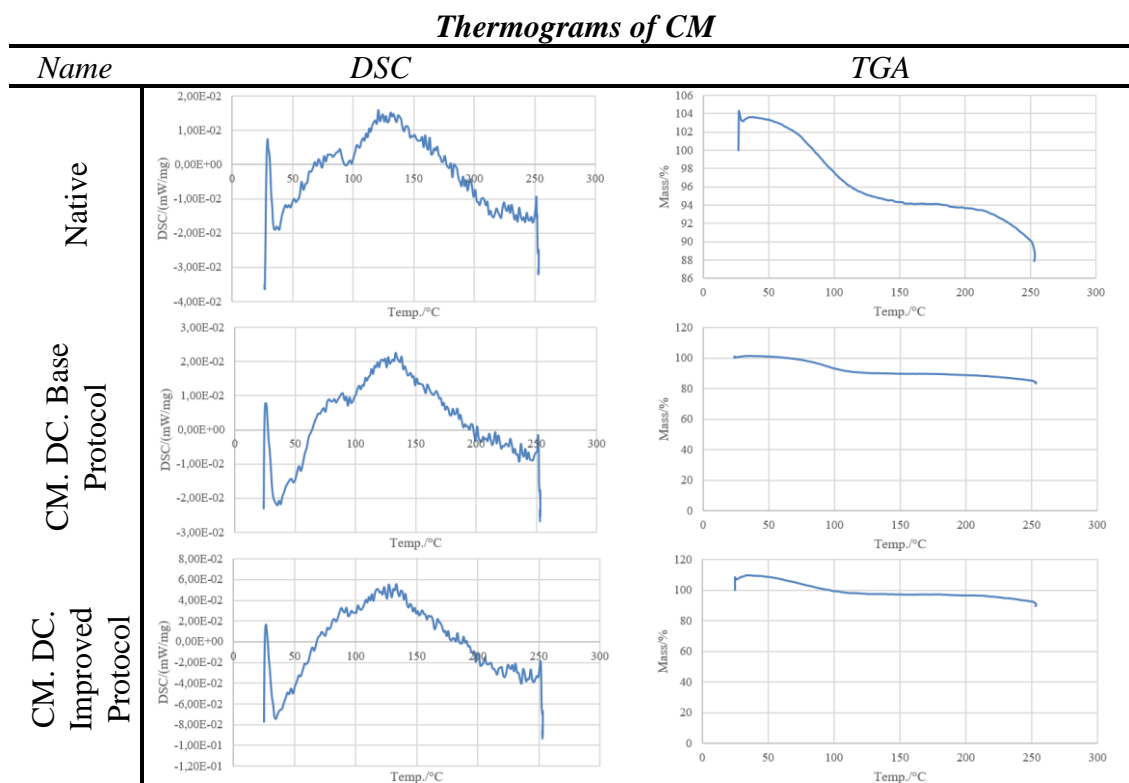
Materials containing collagen, when exposed to high temperatures, can undergo irreversible denaturation [142]. According to the literature, collagen denatures at about 54 °C [145]. The native membrane and AM. DC. by base protocol, present an endothermic peak, approximately around 45 °C, temperature at which, according to the experiment data, collagen denaturation will occur. In opposition, the AM. DC. by improved protocol shows the endothermic peak at ~55 °C, which is in accordance to what is described in the literature [145]. As this one has an endothermic peak at a higher temperature than the other two samples, it means that this sample has possibly a greater amount of water. The amount of water in a sample is directly related to the collagen denaturation temperature, the greater the amount of water, the higher the temperature at which collagen denaturation

takes place [142]. AM. DC. by improved protocol has the endothermic peak much more prominent than the other samples, at $\sim(-0.88)$ mW/mg, while native AM and AM. DC. by base protocol show $\sim(-1,40 \cdot 10^{-1})$ mW/mg and $\sim(-1,87 \cdot 10^{-2})$ mW/mg, respectively. The fact that the endothermic peak of AM. DC. by improved protocol is more prominent means that this sample absorbs a higher amount of heat than the others, which leads to higher collagen denaturation, than the other samples. The native membrane thermogram has an exothermic peak around $58,38$ °C ($\sim 1,65 \cdot 10^{-2}$ mW/mg), the AM. DC. by improved protocol at $115,87$ °C ($\sim 0,72$ mW/mg), and AM. DC. by base protocol at $137,17$ °C ($\sim 7,16 \cdot 10^{-3}$ mW/mg). The more intense the exothermic peak, the greater the amount of heat released by the sample.

The TGA thermograms give us information concerning the mass variation of the samples as a function of temperature change [84]–[86]. The sample that presented the higher mass alteration was the native membrane, losing 22,8 % of mass, then the AM. DC. by base protocol (20,63 %) and, finally, the AM. DC. by improved protocol (14,97 %). As had been observed by DSC the AM. DC. by improved protocol presents a higher amount of water compared to the other samples, which agrees with TGA results. As this membrane has a lower mass loss, in relation to the other two analyzed samples, it means that it loses a smaller amount of water, indicating that it has a greater amount of water bound (not adsorbed) in this membrane, while in the remaining two samples, there is a higher amount of free water [10]. This result may indicate the existence of a tertiary structure of collagen, since what cooperates for the stability of the collagen triple helix are the hydrogen bonds [10].

DSC/TGA of Chorionic Membrane

Table 3.11 shows the thermograms of the chorionic membranes, native and decellularized, using both protocols in study.

Table 3.11 – Thermograms of CM obtained through two different protocols.

All DSC graphs have a lot of noise, which couldn't be eliminated through the software's own smoothing tools. Attempts were made to reduce the noise, namely increasing the amount of sample and using closed aluminum crucibles, with no success.

All the thermograms are very similar, but the one of CM. DC. by base protocol is more similar to the native one, which means that regardless the protocol used, the samples present the same behavior.

In all DSC thermograms an exothermic peak between ~ 125 °C and 135 °C is observed. In CM. DC. by the improved protocol, the exothermic peak, around $127,5$ °C, is much more prominent, $\sim 5,52 \cdot 10^{-2}$ mW/mg, than in the remaining ones, $\sim 2,02 \cdot 10^{-2}$ mW/mg, at $135,85$ °C, of CM. DC. by the base protocol and $\sim 1,47 \cdot 10^{-2}$ mW/mg, at $133,41$ °C, of native membrane, which means that there was a higher heat release from this sample. Also, all thermograms have a small endothermic peak around 35 °C, being more prominent, $(-7,45 \cdot 10^{-2}$ mW/mg), than the others, $(-2,18 \cdot 10^{-2}$ mW/mg on the graph for CM. DC. by the base protocol and $-1,90 \cdot 10^{-2}$ mW/mg for the native membrane). The fact that the CM. DC. by the improved protocol present a more prominent endothermic

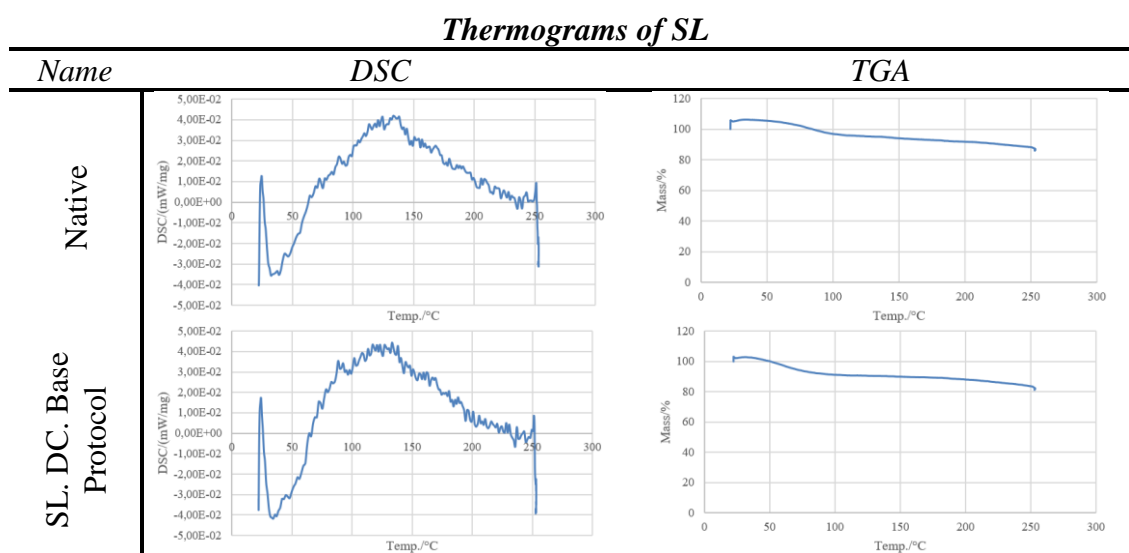
peak means that this sample has suffered higher collagen denaturation than the other ones. As the endothermic peak maintains its position in all samples, indicates that they have the same amount of water [142]. The denaturation temperature of pure collagen is indicated in the literature as being around 54 °C [145], however in these samples denaturation seems to occur around 30 °C.

The sample that presents the higher mass loss is the CM. DC. by the improved protocol, losing ~19,6 % of its original mass. The native membrane loses about 16 % of mass and CM. DC. by the base protocol about 16,9 %. The native membrane loses lower mass, compared to the other membranes, indicating that more water is bound to this membrane [10].

DSC/TGA of Spongy Layer

Table 3.12. shows the thermograms of the spongy layer membranes, native and decellularized, using base protocol.

Table 3.12 – Thermograms of SL obtained through two different protocols.



As in the analysis of the amniotic and chorionic membranes, the DSC graphs present too much noise, which wasn't possible to eliminate using the smoothing tools of the used software, making more difficult their interpretation. Despite the more aggressive character of the base protocol, both the DSC and TGA plots of the decellularized membrane are very similar to those of the native spongy layer.

The native spongy layer presents an endothermic peak at 33.74 °C, and $-3,5 \cdot 10^{-2}$ mW/mg, possibly corresponding to the collagen denaturation temperature. Similarly, the SL. DC. by Base Protocol shows its denaturation peak at 34.60 °C and $-4,17 \cdot 10^{-2}$ mW/mg. None of these analyzed samples present a collagen denaturation temperature similar to the one mentioned in the literature for collagen (~ 54 °C) [145]. Both samples present the endothermic peak at almost the same temperature, suggesting that they have approximately the same amount of constitution water, since the quantity of water in collagen is proportional to its denaturation temperature [142]. The endothermic peak of the decellularized sample has a higher intensity, meaning that this sample absorbs a higher amount of heat, leading to higher denaturation. In addition to the endothermic peaks, the samples also show exothermic peaks. The native sample has an exothermic peak at 135.79 °C and $4,05 \cdot 10^{-2}$ mW/mg, whereas the decellularized sample has a peak at 134.55 °C and $4,18 \cdot 10^{-2}$ mW/mg. Therefore, the thermal behavior of the membranes, is very similar, indicating that the decellularization protocol didn't affect negatively this membrane.

TGA results show that the membranes lose approximately the same amount of mass when subjected to high temperatures. The native one has a mass loss of about 19.28 % and the decellularized one a loss of 21.58 %.

3.1.4. Confocal Raman

Confocal Raman microscopy complements the FTIR analysis, since there are bands that are active in the Raman spectroscopy and aren't in the FTIR and vice versa. **Figure 3.8** shows the Raman spectra of the native and decellularized spongy layer membranes.

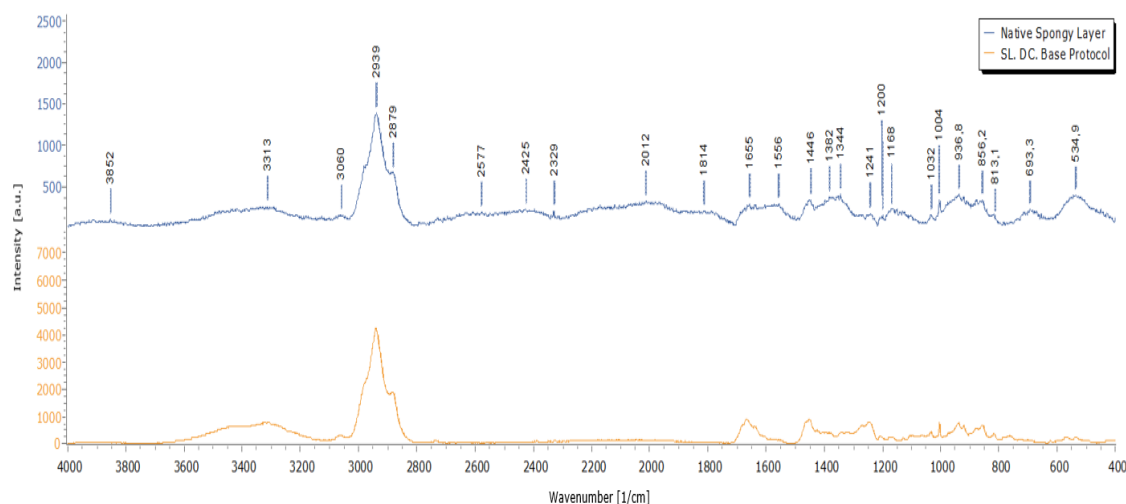


Figure 3.8 – Confocal Raman spectra of Native Spongy Layer and Spongy Layer decellularized by base protocol.

The native and decellularized spongy layer present similar spectra, but with more peaks (**Figure 3.8**). In Annex D, these spectra can be observed individually. As the spongy layer main constituent is non-fibrillar collagen type III [3], [35], the comparison with ultrapure collagen confocal Raman spectra was made (Annex D), as well as a graph that directly compare the three samples spectra. As expected, the spongy layer show similar peaks to the collagen spectrum in four specific zones, [3000-2800] cm^{-1} , [1700-1600] cm^{-1} , [1500-1200] cm^{-1} and [1050-800] cm^{-1} . The peaks of the spongy layer spectrum are represented, along with each assignment on the **Table 3.13**.

Table 3.13 – Assignment of each peak in the Confocal Raman graph of Native Spongy Layer.

| <i>Native Spongy Layer</i> | | |
|---|---|-------------------|
| <i>Wavenumber (cm^{-1})</i> | <i>Assignment</i> | <i>References</i> |
| 813,1 | Tyrosine | [91] |
| 856,2 | Proline | [90], [146] |
| 936,8 | Hydroxyproline | [90], [146] |
| 1004 | Protein band, vibration of C-C bonds of lipids, stretching O-CH ₂ | [88], [89], [93] |
| 1032 | Collagen phenylalanine, CH ² CH ³ , phospholipid and collagen twist modes, vibration of lipid C-C bonds | [88], [128] |
| 1168 | Lipids | [128] |

Cont.

Cont...

| | | |
|------|---|--------------------------------|
| 1241 | Amide III (α helix of tropocollagen) | [90], [147] |
| 1344 | Triptonated, C-H twist, glycosaminoglycans | [90] |
| 1382 | Nucleus and nucleoli in the H5V cell | [89] |
| 1446 | CH, -CH ₂ - and -CH ₃ - bending | [88], [89], [146], [147] |
| 1556 | Amide II, tryptophan and tyrosine, olefins | [91], [128] |
| 1655 | Amide I | [146] |
| 2879 | C-H vibrations and C-H stretching | [89], [93] |
| 2939 | C-H vibrations and C-H stretching | [89], [93] |

3.1.5. Atomic Force Microscopy

AFM allows measuring and obtaining 2D and 3D images of the surface topography of analyzed samples at a nanometer scale [96], [97], as well as extracting information about the surface roughness of the sample [97], [98].

The topography of the lyophilized spongy layer membranes was analyzed by AFM, a difficult task since the samples were too porous. If the tip is smaller or of the same size as the pores in the sample, when passing over these it goes down into a pore, making it difficult to analyze and acquire images and data. That said, it was necessary to analyze a very small area of the sample in question (10 x 10 μm), in order to avoid a surface area with too much pores.

On the **Figure 3.9**, we can observe the topography, in 3D and 2D images, of a certain region on the spongy layers that were examined.

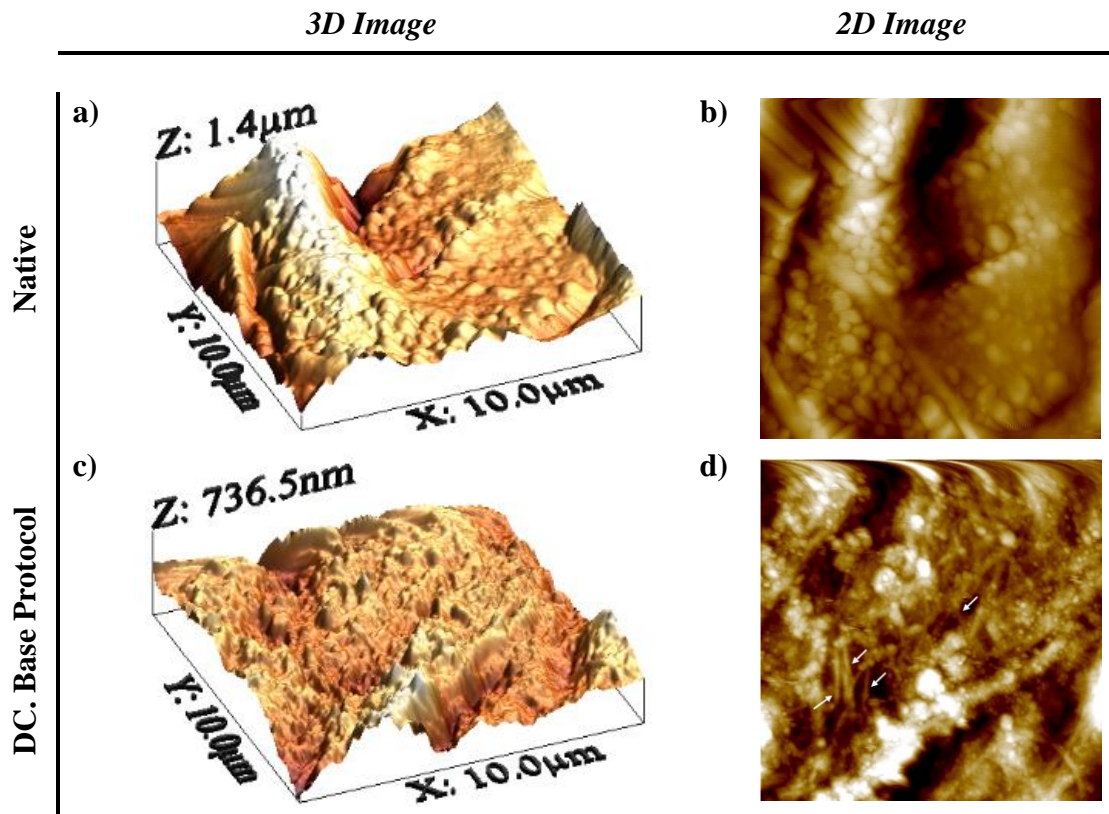


Figure 3.9 – AFM 3D and 2D images of the Spongy Layer topography: native membrane (**a** and **b**) and decellularized by the base protocol (**c** and **d**).

The 3D image of the native membrane **a**) has more relief, with a surface height of $Z=1.4\ \mu\text{m}$ ($Z=1400\ \text{nm}$), compared to image **c**) which has a height of $Z=736.5\ \text{nm}$, having a little more than half the height of image **a**). The reduction in height from image **a**) to **c**) is due to the fact that the sample present in image **c**) has gone through the decellularization process, which made the surface of the sample flatter. Also, image **d**), compared to **b**), shows differences, that is in **d**) it is possible to see some collagen fibers (indicated by the white arrows). In image **c**), it is also possible to visualize the collagen fibers present, perhaps the decellularization process removed components that made it difficult to visualize collagen fibers.

Additionally, AFM images of spongy layer can be observed in Annex E.

Through the AFM analysis of the samples, in addition to the topography images observed previously, it was possible to acquire data on the parameters of the surface roughness of the samples, (**Table 3.14**), namely the R_a , R_q and R_z .

Table 3.14 – Parameters of the surface roughness of the analyzed samples.

| | <i>Test</i> | <i>Ra</i> [μm] | <i>Rq</i> [μm] | <i>Rz</i> [μm] |
|---|-------------|-----------------------------|-----------------------------|-----------------------------|
| <i>Native Spongy layer</i> | A | 0.164 | 0.244 | 1.442 |
| | B | 0.283 | 0.347 | 1.654 |
| | C | 0.657 | 0.763 | 3.560 |
| | D | 0.296 | 0.410 | 3.219 |
| <i>Spongy layer DC by Base Protocol</i> | A | 0.089 | 0.111 | 0.801 |
| | B | 0.075 | 0.098 | 0.772 |
| | C | 0.131 | 0.161 | 0.890 |

Ra stands for mean roughness, it is the mean amplitude of the profile of the analyzed sample in relation to a reference line, for all sample lengths that are in the total length of the sample. One of the limitations of the use of Ra is that, as it is a mean value of amplitudes, it doesn't take into account the shape of the ripples, it doesn't distinguish peaks from valleys and also, due to the ripples present in the length of the analyzed sample, the result may vary [99].

The Rq is the mean square roughness [96], [99], and as Ra, indicates the mean amplitude of the irregularities present on the surface of the sample. But in opposition, because it is squared, the larger amplitudes will have a greater weight in the calculation of their averages, which means that this calculation is more sensitive to peaks and valleys, which gives us more information about the shape of the surface of the analyzed sample. Like what happens in Ra, the value of Rq also varies according to the length of the analyzed sample [99].

Finally, Rz is related to the heights of peaks and valleys, that is, it is the average of the five highest peaks and five highest valleys, along the length of the analyzed sample [99].

By analyzing the data on **Table 3.14** we can conclude that the roughness parameters of the decellularized sample suffered a great reduction due to the decellularization process, which smoothed out the irregularities present on the surface of the sample.

3.1.6. Swelling ratio evaluation

The swelling ratio is defined as the difference between the initial weight of dry microgel and the weight of fully swollen gel divided by the initial weight of dry gel. Spongy layer swelling ratio was determined using Eq. 2.2, **Table 3.15**.

Table 3.15 – Swelling ratio of Spongy layer.

| | M_d (mg) | dH_2O (μ l) | M_s (mg) | Sr |
|---|------------|--------------------|------------|------|
| <i>Native Spongy layer</i> | 0,93 | 93 | 2,17 | 1,33 |
| <i>Spongy layer DC by Base Protocol</i> | 1,17 | 117 | 3,59 | 2,06 |

The fact that we had only small quantities of lyophilized spongy layer, did not allow us to use several replicas of the sample in the swelling analysis. Nevertheless, a preliminary test showed that the spongy layer, after being decellularized, has a swelling ratio higher than the native sample. This may be related to the fact that the decellularization protocol changes the polymer network of the membrane, increasing its hydrophilicity, enabling enough water to be absorbed to increase the volume, but creating elastic tension within the networked polymer chains that prevents total dissolution.

One of the possible applications of the spongy layer is in the form of an hydrogel for regenerative medicine purposes. Swelling characteristics of an hydrogel are important and must be precisely known for such applications [132], [134].

3.1.7. Zeta Potential

The zeta potential values of the native and decellularized spongy layer were determined and are indicated in **Table 3.16**.

Table 3.16 – Zeta Potential of Spongy Layer.

| | pH | $Zeta\ Potential$ (mV) |
|---|------|------------------------|
| <i>Native Spongy layer</i> | 6,15 | -9,65 |
| <i>Spongy layer DC by Base Protocol</i> | 7,09 | -8,21 |

During the determination of the zeta potential, the pH values cannot be controlled. What is presented in the table is an average of the pH values during the test. The zeta potential values are also the calculated average of the values obtained during the execution of this test.

Regarding the zeta potential value, the native spongy layer has a more negative value than the decellularized spongy layer, as well as a lower pH value. This may be related to the decellularization protocol, which possibly removed elements that turned the zeta potential of the layer more negative, as well as more acidic. GAG's for instance are negatively charged components that if present could have been removed during decellularization process. Future work should include GAG's quantification.

Through the zeta potential values obtained, it is possible to infer that our samples are unstable, because they have an absolute value lower than 25 mV [137]. Consequently, there is a tendency for flocculation or coagulation to occur, due to the fact that the attractive forces between the droplets overcome the repulsive forces [102], [104], [148], causing no dispersion [104].

Based on the information obtained from the literature, the spongy layer is composed, in addition to other components, by mucins. These are negatively charged [63], [64] due to their oligosaccharide side chains, carboxyl groups [64], terminal sialic acid [63] and sulfate residues [63], [64], which explains the negative values obtained for the zeta potential.

3.1.8. Rheological Tests

The rheological tests of the native and decellularized spongy layers were performed on small portions of each membrane, which are referenced by distinct letters. Each graph concerns a single membrane, and is composed of more than one sample of the same membrane, in order to understand whether the test is reproducible or not.

The rheological properties of a material directly affect its future employability, as a hydrogel or for another purpose [149]. In the following results, the amplitude sweep and the frequency sweep were studied.

Amplitude sweep, has as main objective to define the linear viscoelastic region of hydrogels (LVR) [149], [150]. In this type of test, the hydrogel is subjected to an increasing rate of shear strain, at a constant frequency [150]. From these parameters, it is possible to determine the storage modulus or elastic modulus, G' , and the loss modulus or viscous modulus, G'' , of the hydrogel when subjected to increasing shear strain [149], [150]. The phase angle δ is a relative measure of the viscous and elastic properties of a material. It ranges from 0° for a fully elastic material to 90° for a fully viscous material.

Frequency sweep, has as main objective to determine its crosslinking behavior, to understand if it is a hydrogel with a reversible network [150], so details related to the architecture of its chain can be observed [149]. In this rheological test, the relationship of the G' and G'' modules with increasing frequency is evaluated [150].

The graphs of the rheological tests, which concern the native spongy layer, can be seen in the **Figure 3.10** and **Figure 3.11**.

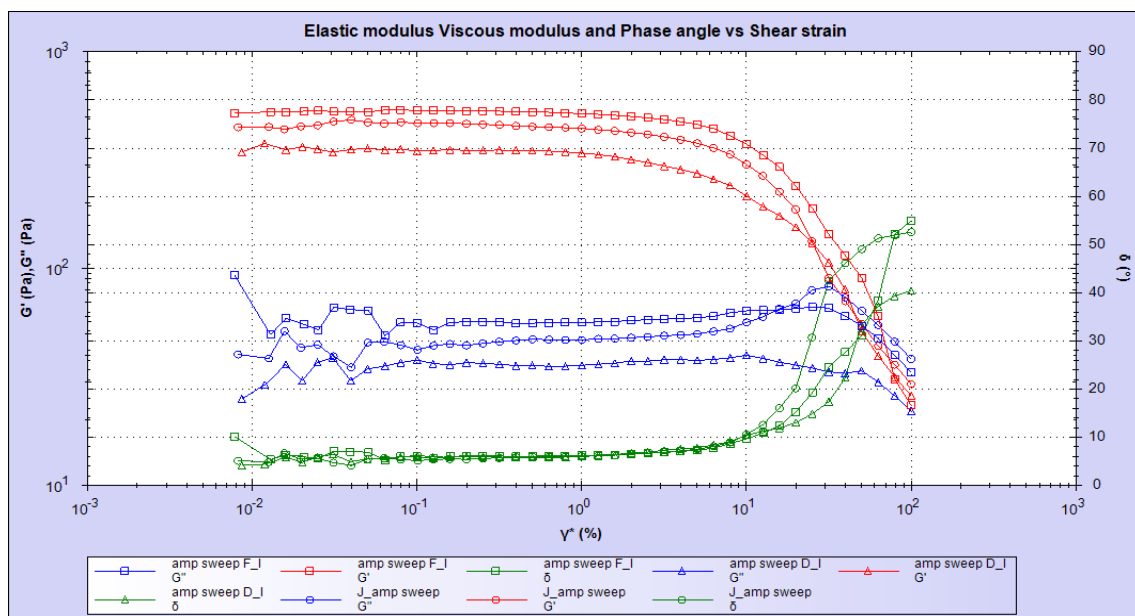


Figure 3.10 – Graph of Amplitude Sweep comparing 3 samples of the Native Spongy Layer.

With the observation of **Figure 3.10**, it is possible to conclude that the behavior of the different samples of the native membrane is quite similar when analyzing the G' , G'' and the phase angle of each analyzed sample. Analyzing each parameter individually with increasing shear strain, we have:

- The G' remains relatively constant until a shear strain of $\sim 10^0$ %, which is its LVR, then the samples begin to yield, at which point the samples begin to behave like a fluid, and the transformation gel-sol occurs [150];
- The G'' , presents its LVR, in a shear strain range from $\sim 10^{-1}$ to 10^1 %, being more constant in this range, before this range the samples show an irregular behavior and after this, they begin to yield, becoming more thin, due to the tension exerted and turning into a fluid [150];
- The phase angle is quite coincident in all samples, presenting exactly the same behavior in the range $\sim 10^{-1}$ to 10^1 %, of shear strain, from which the behavior of the samples already starts to disperse and in all of them it begins to increase the phase angle differently from each other.

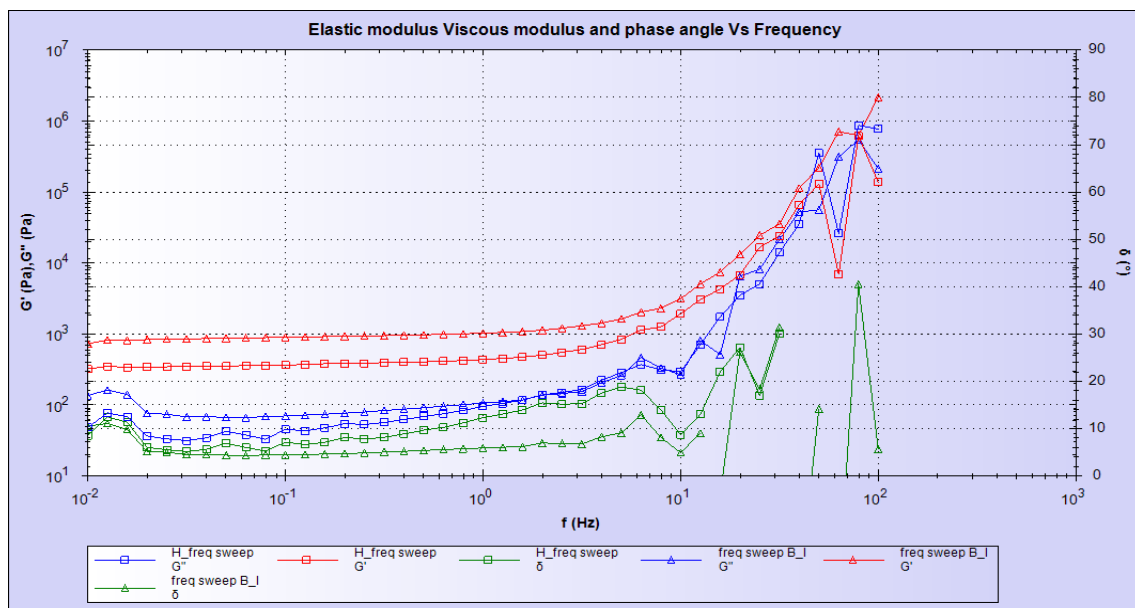


Figure 3.11 – Graph of Frequency Sweep comparing 2 samples of the Native Spongy Layer.

As in the amplitude sweep test, in the frequency sweep test (**Figure 3.11**), the samples show a similar behavior. Analyzing each parameter individually with increasing frequency, we can conclude that:

- Observing the G' and the G'' , the samples show a crossover between the G' and the G'' , in the frequency range $[10^1$ to 10^2 Hz], which means that from this point on, they present a reversible crosslinking [150];

- Regarding the phase angle, it presents a very different behavior from the 10^1 Hz frequency.

The graphs of the rheological tests, which concern the decellularized spongy layer, are represented in **Figure 3.12** and **Figure 3.13**.

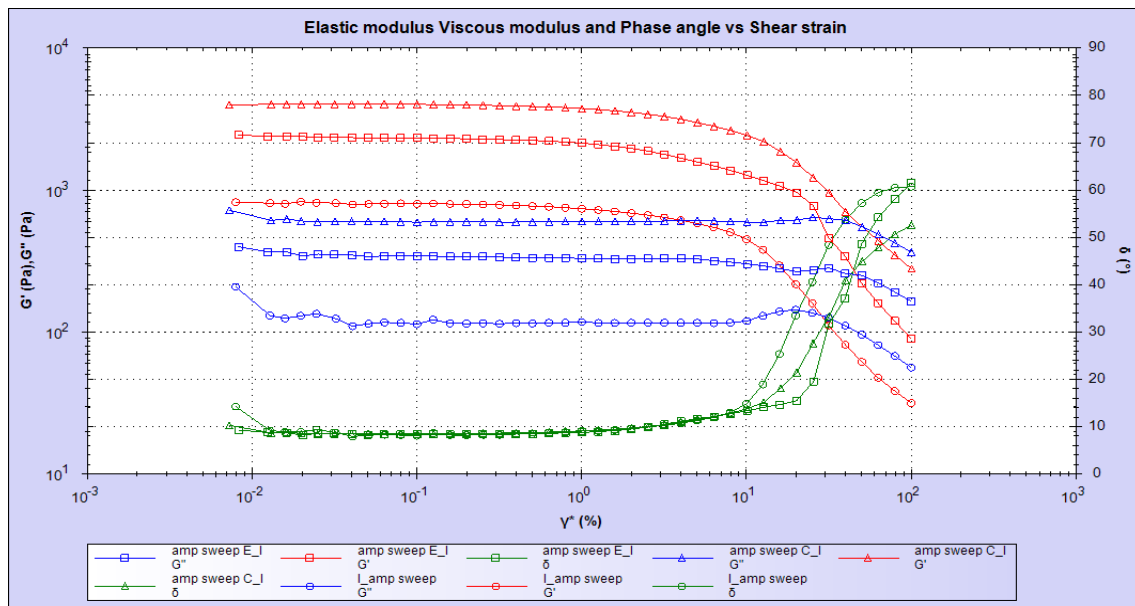


Figure 3.12 – Graph of Amplitude Sweep comparing 3 samples of the Decellularized Spongy Layer.

The **Figure 3.12**, demonstrates the behavior of the decellularized spongy layer when submitted to amplitude sweep tests. The samples present a very similar behavior. Analyzing each parameter individually we can observe that:

- G' maintains its behavior constant, until $\sim 10^0$ % of shear strain, from which the samples start to get thinner and behave like a fluid [150];
- G'' , has a more or less constant behavior up to a shear strain that is approximately halfway between 10^1 and 10^2 %, from which the gel-sol transformation begins [150];
- The phase angle, as occurred in the native membrane, has a very coincident behavior in all samples, being relatively constant in the range $\sim 10^{-2}$ a 10^0 %, of shear strain, from which all samples begin to increase its phase angle with increasing shear strain.

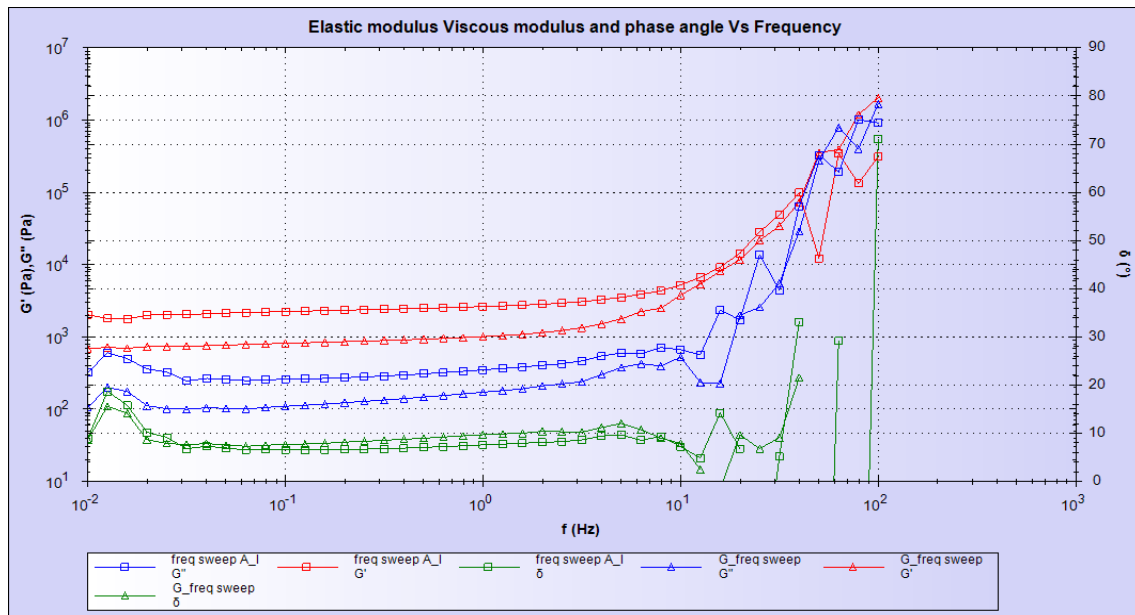


Figure 3.13 – Graph of Frequency Sweep comparing 2 samples of the Decellularized Spongy Layer.

The **Figure 3.13**, portrays the behavior of decellularized samples when submitted to frequency sweep tests. It is observed that the performance of all samples is quite similar. Analyzing each parameter, we have:

- The parameters G' and G'' , cross approximately in the middle of the frequency range [10^1 to 10^2 Hz], demonstrating that they have a reversible crosslinking [150];
- As for the phase angle, it has a very different behavior, starting from the 10^1 Hz frequency.

Both the native and decellularized spongy layers present a very similar behavior when subjected to amplitude sweep and frequency sweep tests, which indicates that the decellularization protocol used didn't significantly affected the rheological characteristics of the spongy layer.

Storage modulus G' represents the stored deformation energy and loss modulus G'' characterizes the deformation energy lost (dissipated) through internal friction when flowing. We can conclude that the spongy layer is a viscoelastic material having a higher storage modulus than loss modulus ($G' > G''$). This is due to links inside the material, for example chemical bonds or physical-chemical interactions.

CHAPTER 4 – FINAL CONSIDERATIONS

4. Final Considerations

4.1. General Discussion

The present research work had as one of the main objectives to study a new decellularization protocol that minimizes the use of toxic components and that wouldn't significantly eliminate components of interest from membranes during their decellularization. Another important objective was to give insights into the characterization of the spongy layer for applications in regenerative and tissue engineering.

To achieve the first objective, the histological analysis of the membranes that constitute the placenta was studied and these were also subjected to FTIR and DSC/TGA analysis. As for the second objective, the spongy layer was also analyzed by AFM and confocal Raman microscopy, the swelling ratio was determined, and it was also submitted to zeta potential and rheological tests.

The available decellularization protocols described in the literature have important limitations (**Table 1.2**). Most of them require prolonged periods, others fail in the preservation of some ECM components. Also, some use compounds that are inadvisable to their toxicity as it is the case of sodium dodecyl sulfate (SDS) or dimethyl sulfoxide. Although SDS can successfully remove unwanted native constituents of the tissue, it can be damaging to the structural and signaling proteins [151]. Also Verheijen *et al* clearly demonstrated that DMSO cannot be considered biologically inert but induces large alterations in microRNAs and epigenic landscape, especially in the maturing cardiac model [109].

Through histological analysis, it was verified that the improved protocol was effective in decellularizing the amniotic membrane, by opposition to what happened to the chorionic membrane where it was more difficult to remove the cells, being visible in the staining samples a significant number of cells. Furthermore, concerning chorionic membrane it was possible to keep after decellularization a high concentration of GAG's, that exist in much higher concentration in the native chorionic membrane than in the amniotic one. To overcome this limitation, we suggest a second cycle to be included in

the decellularization protocol for the chorionic membrane in order to reduce the number of cells.

The spongy layer was decellularized using the old protocol, and a residual number of nucleus were observed after decellularization procedure, something that was not expected since this layer is described in the literature as being almost acellular. This observation may be related to the collection conditions of the membranes that were possibly not the more adequate, leading to an ineffective separation of the amniotic membrane from the spongy layer. According to the literature, it was expected to find glycoproteins in this layer, since it is a mucous layer, together with GAG's, but only few were found, and in the decellularized layer they don't even were identified.

Through FTIR analysis, it was observed that the spectra of native membranes that constitute the placenta present the characteristic amide bands of collagen. Concerning the amniotic membrane, the base decellularization protocol was found to negatively affect the membrane compared to the new protocol. The same happened with the chorionic membrane, the base protocol introducing structural changes in the collagen, evidenced by the elimination of the amide B band in FTIR spectrum. The decellularization base protocol did not affect the spongy layer collagen structure. Nevertheless, no comparison could be made between the effectiveness of each protocol since, due to the small quantity of spongy layer available, it was only possible to test the base protocol with this membrane. All the three membranes, kept their secondary structure of proteins as evidenced by FTIR spectroscopy (amide I region).

The DSC/TGA analysis showed that the denaturation temperature of the native membrane, after decellularization using the improved protocol, increased and was in line with what is described in the literature, ~54 °C. The decellularized membranes when subjected to TGA analysis, loss less mass than the native ones. Concerning the chorionic membrane, no major differences are observed between the protocols, all thermograms showed the same denaturation temperature, but the decellularized membrane with the improved protocol showed the highest mass loss in the TGA analysis. For the spongy layer, the native thermal behavior is similar to the decellularized one.

There is not much information in the literature concerning the characterization of the spongy layer. The present work gave new insights in the characterization of this particular membrane, having in mind its potentialities in tissue and regenerative engineering applications.

The spongy layer is essentially made up of collagen, as described in the literature, and confirmed by the data obtained in histology studies. So, it was essential to compare their confocal Raman spectra with an ultrapure collagen spectrum. Confocal Raman microscopy showed that after decellularization, the spongy layer presents a spectrum very similar to the one of ultrapure collagen, maintaining its characteristic bands.

AFM results showed that this membrane is very porous and has a very rough surface. Its roughness was reduced, almost to half, after the decellularization process, since it eliminates some of its components, essentially maintaining the collagen. This is in agreement with what can be concluded from histology and confocal Raman microscopy. It was also observed that the membrane after going through the decellularization process becomes more hydrophilic.

The study of the zeta potential showed that the native spongy layer has a more negative surface charge than the decellularized one, as well as a lower pH. The more negative charge of the native membrane is in line with what is described in the literature, as the spongy layer is made up of mucins and contains also GAG's, which are negative, making its surface charge negative. After decellularization process, it loses GAG's and mucins, which is also observed by histology, leaving it with a less negative surface charge. Samples are unstable because, since they have a zeta potential value lower than 25 mV, clotting can occur.

The rheological tests, amplitude sweep and frequency sweep, demonstrate that the spongy layer, native and decellularized, present a very similar behavior. The spongy layers exhibit a gel behavior up to approximately a shear strain of 10⁰ % and has a viscoelastic behavior and reversible crosslinking.

In conclusion, it appears that the improved decellularization protocol is less aggressive for the membranes, but it is not completely efficient in removing all the cells, so it still has to undergo some improvements. Regarding the use of the spongy layer in

regenerative and tissue engineering, it seems to have great potential, since it is a very porous membrane, that swells in the presence of water, becoming a viscoelastic hydrogel that has reversible crosslinking, maintaining its gel behavior over a certain shear strain range.

One obstacle with which we come across during the development of the present thesis was the limited amount of available membranes that we had to work with. This problem will be overcome in the future with the new protocol that was established with the Centro Hospitalar S. João (CHSJ). Also, the compositional variability, characteristic of a human tissue is a limitation of this kind of material, that can be minimized by having a batch of membranes from a significant number of different donors.

4.2.Future work

For future work, it would be necessary to improve the new protocol, so that it becomes more effective in decellularizing the membranes, or alternatively submit the membranes to two cycles of decellularization using the same protocol. The quantification of GAG's and DNA should also be performed, before and after decellularization. It would also be interesting to test the decellularization of the membranes with supercritical CO₂ as an alternative to the protocols used. Additionally, it would also be very important to test the production of spongy layer based hydrogels and scaffolds envisaging their use in regenerative and tissue engineering. Finally, *in vitro* tests with different cells followed by *in vivo* tests using the most promising formulations, would also be very interesting.

References

- [1] R. Laurent, A. Nallet, L. Obert, L. Nicod, and F. Gindraux, “Storage and qualification of viable intact human amniotic graft and technology transfer to a tissue bank,” *Cell Tissue Bank.*, vol. 15, no. 2, pp. 267–275, 2014, doi: 10.1007/s10561-014-9437-x.
- [2] B. Farhadhosseinabadi *et al.*, “Amniotic membrane and its epithelial and mesenchymal stem cells as an appropriate source for skin tissue engineering and regenerative medicine,” *Artif. Cells, Nanomedicine Biotechnol.*, vol. 46, no. sup2, pp. 431–440, 2018, doi: 10.1080/21691401.2018.1458730.
- [3] K. A. Shaw, S. A. Parada, D. M. Gloystein, and J. G. Devine, “The Science and Clinical Applications of Placental Tissues in Spine Surgery,” *Glob. Spine J.*, vol. 8, no. 6, pp. 629–637, 2018, doi: 10.1177/2192568217747573.
- [4] C. Mason and P. Dunnill, “A brief definition of regenerative medicine,” *Regen. Med.*, vol. 3, no. 1, pp. 1–5, 2008, doi: 10.2217/17460751.3.1.1.
- [5] Z. Peng *et al.*, “Advances in biomaterials for adipose tissue reconstruction in plastic surgery,” *Nanotechnol. Rev.*, vol. 9, no. 1, pp. 385–395, Jan. 2020, doi: 10.1515/NTREV-2020-0028/MACHINEREADABLECITATION/RIS.
- [6] M. Cuppini, “Engenharia Tecidual aplicado à Odontologia: Estado da Arte,” *Repos. Unisc*, pp. 11–58, 2015.
- [7] F. J. O’Brien, “Biomaterials & scaffolds for tissue engineering,” *Mater. Today*, vol. 14, no. 3, pp. 88–95, 2011, doi: 10.1016/S1369-7021(11)70058-X.
- [8] P. X. Ma, “Scaffolds for tissue fabrication,” *Mater. Today*, vol. 7, no. 5, pp. 30–40, 2004, doi: 10.1016/S1369-7021(04)00233-0.
- [9] P. Julio *et al.*, “Processo De Descelularização De Órgãos E Uso Do Mesmo,” no. 21, 2017.
- [10] M. Justino, “Extração E Caracterização De Colágeno De Pele De Tilápia (*Oreochromis Niloticus*): Avaliação Do Seu Potencial Na Formulação De

- Hidrogéis Para Medicina Regenerativa,” 2021.
- [11] R. M. L. Nobre, “Hidrogéis: potencial de aplicação em engenharia de tecidos,” 2016, [Online]. Available: <http://hdl.handle.net/10400.1/9922>.
- [12] I. F. Lavrador, “Desenvolvimento de biomateriais para futura aplicação em medicina regenerativa,” pp. 1–97.
- [13] C. D. F. Moreira, “Avaliação da adição de colágeno tipo I e nanopartículas de vidro bioativo a hidrogéis termossensíveis de quitosana para uso na engenharia de tecido,” p. 91, 2014.
- [14] R. S. C. Galante, “Esterilização De Hidrogéis Para Aplicações Biomédicas,” 2017.
- [15] S. José, “Decellularization and Solubilization of Human Chorion Membrane : a novel ECM supplement / substrate for mesenchymal stem cells culture,” 2018.
- [16] P. M. A. Coimbra, “Preparação e caracterização de sistemas de libertação controlada de fármacos com base em polímeros de origem natural,” p. 268, 2010, [Online]. Available: <https://estudogeral.sib.uc.pt/handle/10316/14502>.
- [17] E. L. dos S. Campos and M. Rogério, “Síntese E Caracterização De Hidrogéis Híbridos Baseados Em Alginato, Goma Arábica E Microesferas De Sílica, Para Aplicação Na Liberação Controlada E Sustentada De Fármacos,” 2017.
- [18] V. Ryzhuk *et al.*, “Human amnion extracellular matrix derived bioactive hydrogel for cell delivery and tissue engineering,” *Mater. Sci. Eng. C. Mater. Biol. Appl.*, vol. 85, p. 191, Apr. 2018, doi: 10.1016/J.MSEC.2017.12.026.
- [19] I. A. Deus, “Preparation of a hydrogel from human fetal membranes for 3D cell culture,” pp. 1–42, 2012.
- [20] S. Leal-Marin *et al.*, “Human Amniotic Membrane: A review on tissue engineering, application, and storage,” *J. Biomed. Mater. Res. - Part B Appl. Biomater.*, vol. 109, no. 8, pp. 1198–1215, 2021, doi: 10.1002/jbm.b.34782.
- [21] I. A. Deus, J. F. Mano, and C. A. Custódio, “Perinatal tissues and cells in tissue engineering and regenerative medicine,” *Acta Biomater.*, vol. 110, no. xxxx, pp. 1–14, 2020, doi: 10.1016/j.actbio.2020.04.035.

- [22] S. Rohringer *et al.*, “Chorion-derived extracellular matrix hydrogel and fibronectin surface coatings show similar beneficial effects on endothelialization of expanded polytetrafluorethylene vascular grafts,” *Mater. Today Bio*, vol. 14, no. November 2021, p. 100262, 2022, doi: 10.1016/j.mtbio.2022.100262.
- [23] D. Heck, “Avaliação Da Associação Células-Tronco Mesenquimais De Placenta Humana Em Biomateriais Baseados Em Celulose Bacteriana,” 2012.
- [24] J. Cesar, F. Desenvolvimento De Biomaterial, and A. P. De Matriz, “Desenvolvimento De Biomaterial A Partir De Matriz Amniótica Humana,” 2012.
- [25] A. Araújo, “Avaliação De Técnicas De Isolamento E Comparação De Células-Tronco Mesenquimais Humanas De Membrana Amniótica, Membrana Coriônica, Cordão Umbilical E Decídua Da Placenta,” no. August, pp. 0–91, 2016.
- [26] A. R. Silini *et al.*, “Perinatal Derivatives: Where Do We Stand? A Roadmap of the Human Placenta and Consensus for Tissue and Cell Nomenclature,” *Front. Bioeng. Biotechnol.*, vol. 8, p. 1438, Dec. 2020, doi: 10.3389/FBIOE.2020.610544/BIBTEX.
- [27] D. Braghirolli, “Produção De Scaffolds Contendo Células-Tronco Para Uso Na Engenharia De Tecidos Através Da Associação Das Técnicas De Electrospinning E Bio-Electrospraying.”
- [28] S. Shariatzadeh *et al.*, “Developing a pro-angiogenic placenta derived amniochorionic scaffold with two exposed basement membranes as substrates for cultivating endothelial cells,” *Sci. Rep.*, vol. 11, no. 1, Dec. 2021, doi: 10.1038/S41598-021-01922-Y.
- [29] F. Gindraux *et al.*, “Similarities between induced membrane and amniotic membrane: Novelty for bone repair,” *Placenta*, vol. 59, pp. 116–123, 2017, doi: 10.1016/j.placenta.2017.06.340.
- [30] T. Ž. Ramuta and M. E. Kreft, “Human Amniotic Membrane and Amniotic Membrane-Derived Cells: How Far Are We from Their Use in Regenerative and Reconstructive Urology?,” *Cell Transplant.*, vol. 27, no. 1, pp. 77–92, 2018, doi: 10.1177/0963689717725528.

- [31] N. Suresh, B. Arul, D. Kowsky, and V. Natanasabapathy, “Successful regenerative endodontic procedure of a nonvital immature permanent central incisor using amniotic membrane as a novel scaffold,” *Dent. J.*, vol. 6, no. 3, 2018, doi: 10.3390/dj6030036.
- [32] A. K. Riau, R. W. Beurman, L. S. Lim, and J. S. Mehta, “Preservation, sterilization and de-epithelialization of human amniotic membrane for use in ocular surface reconstruction,” *Biomaterials*, vol. 31, no. 2, pp. 216–225, 2010, doi: 10.1016/j.biomaterials.2009.09.034.
- [33] C. Haller, “Evaluation of human fetal membrane sealing (Doctoral dissertation, University of Zurich).,” 2013.
- [34] G. Bourne, F.R.C.S., and M.R.C.O.G., “The Fetal Membranes,” 1962.
- [35] H. Elkhenany, A. El-Derby, M. Abd Elkodous, R. A. Salah, A. Lotfy, and N. El-Badri, “Applications of the amniotic membrane in tissue engineering and regeneration: the hundred-year challenge,” *Stem Cell Res. Ther.*, vol. 13, no. 1, pp. 1–19, 2022, doi: 10.1186/s13287-021-02684-0.
- [36] M. A. Fusco De Souza, “Membrana amniótica humana como curativo biológico para feridas de difícil resolução e as possíveis utilizações no hnmmd 1ºten (rm2-md),” *Arq. Bras. Med. Naval, Rio Janeiro*, vol. 76, no. 1, pp. 63–68, Accessed: Apr. 11, 2022. [Online]. Available: <https://www.mediligence.com/store/pa->
- [37] C. M. Zelen, R. J. Snyder, T. E. Serena, and W. W. Li, “The Use of Human Amnion / Chorion Membrane in the Clinical Setting for Lower Extremity Repair : A Review,” vol. 32, pp. 135–146, 2015, doi: 10.1016/j.cpm.2014.09.002.
- [38] V. Mancini and V. Pensabene, “Organs-On-Chip Models of the Female Reproductive System,” *Bioeng. 2019, Vol. 6, Page 103*, vol. 6, no. 4, p. 103, Nov. 2019, doi: 10.3390/BIOENGINEERING6040103.
- [39] R. Gargioni, “Avaliação Do Nicho Molecular De Células-Tronco Hematopoéticas E Mesenquimais Em Placenta Humana: Caracterização Estrutural E Ultraestrutural,” 2014.
- [40] R. BSc. and M. P., “Arachidonic Acid Metabolism by Human Fetal Membranes in

- Tissue Culture.,” *Riskesdas 2018*, vol. 3, pp. 103–111, 2015.
- [41] L. P. Frazão, J. Vieira-de-Castro, C. Nogueira-Silva, and N. M. Neves, “Method to decellularize the human chorion membrane,” *Methods Cell Biol.*, vol. 157, pp. 23–35, 2020, doi: 10.1016/bs.mcb.2019.11.002.
- [42] M. Gordon L. Bourne F.RCS, “The microscopic anatomy of the human amnion and chorion,” vol. 0, pp. 0–3, doi: 10.1016/0002-9378(60)90512-3.
- [43] A. Gupta, S. D. Kedige, and K. Jain, “Amnion and chorion membranes: Potential stem cell reservoir with wide applications in periodontics,” *Int. J. Biomater.*, vol. 2015, 2015, doi: 10.1155/2015/274082.
- [44] C. D’Lima, U. Samant, A. L. Gajiwala, and A. Puri, “Human chorionic membrane: A novel and efficient alternative to conventional collagen membrane,” *Trends Biomater. Artif. Organs*, vol. 34, no. 1, pp. 33–37, 2020.
- [45] N. J. Willett *et al.*, “Intra-articular injection of micronized dehydrated human amnion/chorion membrane attenuates osteoarthritis development,” *Arthritis Res. Ther.*, vol. 16, no. 1, pp. 1–10, 2014, doi: 10.1186/ar4476.
- [46] “Anexos embrionários,” 2020, Accessed: Jul. 25, 2022. [Online]. Available: https://uab.ufsc.br/biologia/files/2020/08/Capitulo_11.pdf.
- [47] R. Shah, R. Thomas, and D. Mehta, “Ridge preservation using demineralized freeze-dried bone allograft and chorion membrane,” *Int. J. Oral Heal. Sci.*, vol. 4, no. 2, p. 89, 2014, doi: 10.4103/2231-6027.165101.
- [48] S. Kothiwale and J. Ajbani, “Evaluation of anti-inflammatory effect of chorion membrane in periodontal pocket therapy: A clinical and biochemical study,” *J. Indian Soc. Periodontol.*, vol. 22, no. 5, p. 433, 2018, doi: 10.4103/JISP.JISP_280_18.
- [49] J. Esteves, K. M. Bhat, B. Thomas, J. M. Varghese, and T. Jadhav, “Efficacy of Human Chorion Membrane Allograft for Recession Coverage: A Case Series,” *J. Periodontol.*, vol. 86, no. 8, pp. 941–944, 2015, doi: 10.1902/jop.2014.140025c.
- [50] M. Zare-Bidaki, S. Sadrinia, S. Erfani, E. Afkar, and N. Ghanbarzade, “Antimicrobial properties of amniotic and chorionic membranes: A comparative

- study of two human fetal sacs,” *J. Reprod. Infertil.*, vol. 18, no. 2, pp. 218–224, 2017.
- [51] S. Kothiwale, A. Rathore, and V. Panjwani, “Enhancing gingival biotype through chorion membrane with innovative step in periodontal pocket therapy,” *Cell Tissue Bank.*, vol. 17, no. 1, pp. 33–38, 2016, doi: 10.1007/s10561-015-9524-7.
- [52] B. Graça *et al.*, “Angiogénese e cancro: Da biopatologia à terapêutica,” *Acta Med. Port.*, vol. 17, no. 1, pp. 76–93, 2004.
- [53] H. Oxlund, R. Helmig, J. T. Halaburt, and N. Uldbjerg, “Biomechanical analysis of human chorioamniotic membranes,” *Eur. J. Obstet. Gynecol. Reprod. Biol.*, vol. 34, no. 3, pp. 247–255, 1990, doi: 10.1016/0028-2243(90)90078-F.
- [54] L. P. Frazão, J. Vieira de Castro, C. Nogueira-Silva, and N. M. Neves, “Decellularized human chorion membrane as a novel biomaterial for tissue regeneration,” *Biomolecules*, vol. 10, no. 9, pp. 1–16, 2020, doi: 10.3390/biom10091208.
- [55] S. Mohr, C. B. Portmann-Lanz, A. Schoeberlein, R. Sager, and D. V. Surbek, “Generation of an osteogenic graft from human placenta and placenta-derived mesenchymal stem cells,” *Reprod. Sci.*, vol. 17, no. 11, pp. 1006–1015, 2010, doi: 10.1177/1933719110377471.
- [56] D. K. Suresh and A. Gupta, “Gingival Biotype Enhancement and Root Coverage Using Human Placental Chorion Membrane,” *Clin. Adv. Periodontics*, vol. 3, no. 4, pp. 237–242, 2013, doi: 10.1902/cap.2012.120039.
- [57] S. V. Kothiwale, “The evaluation of chorionic membrane in guided tissue regeneration for periodontal pocket therapy: A clinical and radiographic study,” 2013, doi: 10.1007/s10561-013-9386-9.
- [58] K. H. Schneider *et al.*, “Decellularized human placenta chorion matrix as a favorable source of small-diameter vascular grafts,” *Acta Biomater.*, 2015, doi: 10.1016/j.actbio.2015.09.038.
- [59] I. Inci, A. Norouz Dizaji, C. Ozel, U. Morali, F. Dogan Guzel, and H. Avci, “Decellularized inner body membranes for tissue engineering: A review,” *J.*

- Biomater. Sci. Polym. Ed.*, vol. 31, no. 10, pp. 1287–1368, 2020, doi: 10.1080/09205063.2020.1751523.
- [60] G. L. Bourne, “The Volume and Circulation of the Liquor Amnii [Abridged],” *Proc. R. Soc. Med.*, vol. 59, no. 11P1, pp. 1127–1128, 1966, doi: 10.1177/003591576605911p128.
- [61] P. Nazari Hashemi Fanny Chaventre Aurelie Bisson Julie Gueudry Olivier Boyer Marc Muraine, “Mapping of proteomic profile and effect of the spongy layer in the human amniotic membrane,” *Cell Tissue Bank.*, vol. 21, doi: 10.1007/s10561-020-09821-8.
- [62] R. Bansil and B. S. Turner, “The biology of mucus : Composition , synthesis and organization ☆,” *Adv. Drug Deliv. Rev.*, vol. 124, pp. 3–15, 2018, doi: 10.1016/j.addr.2017.09.023.
- [63] J. Y. Lock, T. L. Carlson, and R. L. Carrier, “Mucus models to evaluate the diffusion of drugs and particles,” *Adv. Drug Deliv. Rev.*, vol. 124, pp. 34–49, 2018, doi: 10.1016/j.addr.2017.11.001.
- [64] C. V. Duffy, L. David, and T. Crouzier, “Covalently-crosslinked mucin biopolymer hydrogels for sustained drug delivery,” *Acta Biomater.*, vol. 20, pp. 51–59, 2015, doi: 10.1016/j.actbio.2015.03.024.
- [65] D. Barik *et al.*, “Polymer–Protein Hybrid Network Involving Mucin: A Mineralized Biomimetic Template for Bone Tissue Engineering,” *Macromol. Biosci.*, vol. 21, no. 6, pp. 1–18, 2021, doi: 10.1002/mabi.202000381.
- [66] D. Barik, K. Kundu, and M. Dash, “Montmorillonite stabilized chitosan-co-mucin hydrogel for tissue engineering applications,” *RSC Adv.*, vol. 11, no. 48, pp. 30329–30342, 2021, doi: 10.1039/d1ra04803a.
- [67] C. Taylor, J. P. Pearson, K. I. Draget, P. W. Dettmar, and O. Smidsrød, “Rheological characterisation of mixed gels of mucin and alginate,” *Carbohydr. Polym.*, vol. 59, no. 2, pp. 189–195, 2005, doi: 10.1016/j.carbpol.2004.09.009.
- [68] S. P. Authimoolam and T. D. Dziubla, “Biopolymeric mucin and synthetic polymer analogs: Their structure, function and role in biomedical applications,” *Polymers*

- (*Basel*), vol. 8, no. 3, 2016, doi: 10.3390/polym8030071.
- [69] A. Shakouri-Motlagh, R. Khanabdali, D. E. Heath, and B. Kalionis, “The application of decellularized human term fetal membranes in tissue engineering and regenerative medicine (TERM),” *Placenta*, vol. 59, pp. 124–130, Nov. 2017, doi: 10.1016/j.placenta.2017.07.002.
- [70] J. S. Choi, J. D. Kim, H. S. Yoon, and Y. W. Cho, “Full-thickness skin wound healing using human placenta-derived extracellular matrix containing bioactive molecules,” *Tissue Eng. - Part A*, vol. 19, no. 3–4, pp. 329–339, 2013, doi: 10.1089/ten.tea.2011.0738.
- [71] M. Gholipourmalekabadi *et al.*, “Development of a cost-effective and simple protocol for decellularization and preservation of human amniotic membrane as a soft tissue replacement and delivery system for bone marrow stromal cells,” *Adv. Healthc. Mater.*, vol. 4, no. 6, pp. 918–926, 2015, doi: 10.1002/adhm.201400704.
- [72] S. Khosravimelal, M. Momeni, M. Gholipur, S. C. Kundu, and M. Gholipourmalekabadi, *Protocols for decellularization of human amniotic membrane*, 1st ed., vol. 157. Elsevier Inc., 2020.
- [73] Ö. S. Somuncu, Y. Coşkun, B. Ballica, A. F. Temiz, and D. Somuncu, “In vitro artificial skin engineering by decellularized placental scaffold for secondary skin problems of meningomyelocele,” *Journal of Clinical Neuroscience*, vol. 59, pp. 291–297, 2019, doi: 10.1016/j.jocn.2018.10.044.
- [74] Z. Kakabadze *et al.*, “Decellularized human placenta supports hepatic tissue and allows rescue in acute liver failure,” *Hepatology*, vol. 67, no. 5, pp. 1956–1969, 2018, doi: 10.1002/hep.29713.
- [75] L. Flynn, J. L. Semple, and K. A. Woodhouse, “Decellularized placental matrices for adipose tissue engineering,” *J. Biomed. Mater. Res. - Part A*, vol. 79, no. 2, pp. 359–369, 2006, doi: 10.1002/JBM.A.30762.
- [76] L. I. Sous Naasani *et al.*, “Decellularized human amniotic membrane associated with adipose derived mesenchymal stromal cells as a bioscaffold: Physical, histological and molecular analysis,” *Biochem. Eng. J.*, vol. 152, no. May, p.

- 107366, 2019, doi: 10.1016/j.bej.2019.107366.
- [77] R. A. Salah, I. K. Mohamed, and N. El-Badri, “Development of decellularized amniotic membrane as a bioscaffold for bone marrow-derived mesenchymal stem cells: ultrastructural study,” *J. Mol. Histol.*, vol. 49, no. 3, pp. 289–301, 2018, doi: 10.1007/s10735-018-9768-1.
- [78] K. H. Schneider *et al.*, “Decellularized human placenta chorion matrix as a favorable source of small-diameter vascular grafts,” *Acta Biomater.*, vol. 29, pp. 125–134, 2016, doi: 10.1016/j.actbio.2015.09.038.
- [79] C. Lima, “Caracterização bioquímica de lesões neoplásicas via espectroscopia de absorção no infravermelho por Transformada de Fourier,” *J. Geotech. Geoenvironmental Eng. ASCE*, vol. 120, no. 11, p. 259, 2015.
- [80] S. E. Glassford, B. Byrne, and S. G. Kazarian, “Recent applications of ATR FTIR spectroscopy and imaging to proteins,” *Biochim. Biophys. Acta - Proteins Proteomics*, vol. 1834, no. 12, pp. 2849–2858, 2013, doi: 10.1016/j.bbapap.2013.07.015.
- [81] G. Roiu, S. Cavalu, A. Teusdea, D. A. Petricas-Heredea, and O. Fratila, “Assessment of antibiotic influence on structural modifications of amniotic membrane by FTIR spectroscopy,” *Mater. Plast.*, vol. 57, no. 2, pp. 191–198, 2020, doi: 10.37358/MP.20.2.5365.
- [82] J. Grdadolnik, “ATR-FTIR spectroscopy: Its advantages and limitations,” *Acta Chim. Slov.*, vol. 49, no. 3, pp. 631–642, 2002.
- [83] M. G. Santos, “Desenvolvimento E Caracterização Termo-Mecânica De,” 2021.
- [84] G. Denari and É. Cavalheiro, “Princípios e aplicações de análise térmica,” vol. 48, 2012, doi: 10.2141/jpsa.010134.
- [85] M. K. D. Rambo, M. C. D. Rambo, K. J. C. R. Almeida, and G. P. Alexandre, “Estudo de análise termogravimétrica de diferentes biomassas lignocelulósicas utilizando a análise por componentes principais,” *Ciência e Nat.*, vol. 37, no. 3, pp. 862–868, 2015, doi: 10.5902/2179460x18332.
- [86] D. M. NEJELISKI and L. de C. DUARTE, “Caracterização do Porongo (Lagenaria

- siceraria): análise termogravimétrica, determinação do teor de umidade, da densidade básica e da densidade aparente,” pp. 6078–6078, 2020, doi: 10.5151/ped2018-https://doi.org/10.29147/dat.v4i1.108.
- [87] A. Cyrino Lucena, D. Mendez Soares, W. Evaristo Gomes, A. Etchegaray Junior, D. Beretta, and P. Simões Casagrande, “Quantificação de surfactinas utilizando espectroscopia Raman Confocal,” *XXV Congr. Iniciação Científica da Unicamp*, vol. I, p. 78931, 2017, doi: 10.19146/pibic-2017-78931.
- [88] I. M. B. Gomes, A. P. C. Prereira, M. G. P. Silva, D. M. Taciana, P. Singh, and A. A. Martin, “Análise Da Permeação De Nanolipídeos Em Cabelo Humano,” pp. 1–6, 2012.
- [89] S. Tott, M. Grosicki, B. Klimas, D. Augustynska, S. Chlopicki, and M. Baranska, “Raman spectroscopic features of primary cardiac microvascular endothelial cells (CMECs) isolated from the murine heart,” *Analyst*, vol. 143, no. 24, pp. 6079–6086, 2018, doi: 10.1039/c8an01308j.
- [90] M. P. Souza *et al.*, “Diferenças Entre Estrias Brancas E Estrias Vermelhas o Núcleo De Estudos Biológicos E Métodos Alternativos,” p. 4, 2014.
- [91] P. K. Oliveira, M. G. Tosato, R. de S. Alves, A. A. Martin, P. P. Fávero, and L. Raniero, “Análise da composição bioquímica da pele por espectroscopia Raman,” *Rev. Bras. Eng. Biomed.*, vol. 28, no. 3, pp. 278–287, 2012, doi: 10.4322/rbeb.2012.032.
- [92] C. Fang *et al.*, “Identification and visualisation of microplastics / nanoplastics by Raman imaging (iii): algorithm to cross-check multi-images,” *Water Res.*, vol. 194, p. 116913, 2021, doi: 10.1016/j.watres.2021.116913.
- [93] G. Giridhar, R. R. K. N. Manepalli, and G. Apparao, *Confocal Raman Spectroscopy*, vol. 2. Elsevier Inc., 2017.
- [94] S. K. Soininem, *Cellular, Placental and in vivo Pharmacokinetics of Liposomal Doxorubicin*. 2016.
- [95] L. C. Fontana, S. M. Ali, L. Raniero, J. Ferreira-strixino, T. Fotodinâmica, and D. A. S. Hifumi, “Análise Espectroscópica De Tumores Mamários Submetidos A

- Terapia Fotodinâmica,” pp. 1–6, 2010.
- [96] C. Paper, P. Grossa, and P. Grossa, “Estudo Da Fração Argila Do Solo Por,” no. June, 2016.
- [97] M. C. S. Fernandes, P. I. Paulin Filho, and M. R. Morelli, “Análise da superfície de grês porcelanato por microscopia de força atômica,” *Cerâmica*, vol. 57, no. 342, pp. 173–179, 2011, doi: 10.1590/s0366-69132011000200007.
- [98] S. Veríssimo, “Análise superficial em AFM de filmes finos com gradiente de composição em profundidade obtidos por codeposição catódica Agradecimentos,” 2009.
- [99] L. C. R. Carpinetti, E. V. Gonçalves Filho, A. J. V. . Porto, and R. G. Jasinevicius, “Rugosidade Superficial: Conceitos e Princípios de Medição,” p. 51, 1996.
- [100] N. Ishida and V. S. J. Craig, “Direct Measurement of Interaction Forces between Surfaces in Liquids Using Atomic Force Microscopy †,” no. December 2018, 2019, doi: 10.14356/kona.2019013.
- [101] G. Becker *et al.*, “Estudo do potencial zeta na coagulação/floculação de suspensões de caulim,” *Siepe*, pp. 6–11, 2018.
- [102] D. Dinger, “Medidas de pontos isoelétricos sem o uso de analisador de Potencial Zeta,” *Cerâmica Ind.*, vol. 11, no. 3, pp. 23–24, 2006.
- [103] R. Marsalek, “Zeta Potential - Applications,” vol. 35, 2012, doi: 10.1007/978-3-642-40872-4_612-1.
- [104] J. Batalla Mayoral, A. Cuadros Moreno, and E. San Martín Martínez, “Potencial zeta en la determinación de carga superficial de liposomas.,” *Latin-American J. Phys. Educ.*, vol. 8, no. 4, p. 19, 2014.
- [105] D. G. De Araújo, “Propriedades Reológicas da Polpa de Bauxita – II. Avaliação do rotor tipo vane,” pp. 1–7, 2000, [Online]. Available: <http://mineralis.cetem.gov.br/handle/cetem/645>.
- [106] M. V. de S. e Silva and R. G. Pereira, “Comportamento reológico de formulações para dentifrícios,” doi: 10.1097/01.ede.0000416813.46555.3b.

- [107] C. R. Nascimento, *Reologia e Reometria Aplicadas ao Estudo de Polpas Minerais*. 2008.
- [108] M. Laranjo, “Preservation of Amniotic Membrane,” *Amniotic Membr. Orig. Charact. Med. Appl.*, pp. 1–254, 2015, doi: 10.1007/978-94-017-9975-1.
- [109] M. Verheijen *et al.*, “DMSO induces drastic changes in human cellular processes and epigenetic landscape in vitro,” *Sci. Rep.*, vol. 9, no. 1, pp. 1–12, 2019, doi: 10.1038/s41598-019-40660-0.
- [110] S. L. B. de Ferenczy Peter Alexander von Harbach, “Comparação dos meios de preparação e preservação de membrana amniótica humana para uso no tratamento de doenças da superfície ocular,” *Rev. Bras. Oftalmol.*, vol. 79, no. 1, pp. 71–80, 2020, doi: 10.5935/0034-7280.20.
- [111] H. C. Terroni *et al.*, “Liofilização,” pp. 271–284.
- [112] E. T. de V. Silva, P. I. S. e Silva, A. K. de S. Lima, S. F. do Oriente, and D. S. G. Gouveia, “Secagem Por Liofilização: Método De Operação E Relevância Na Área De Alimentos,” no. 1, 1997.
- [113] K. G. P. C. de Mello, “Imobilização de pepsina em membranas liofilizadas de quitosana e O-carboximetilquitosana,” p. 99, 2009.
- [114] L. D. L. Timm, “Técnicas Rotineiras De Preparação E Análise De Lâminas Histológicas,” *Cad. La Salle XI*, vol. 2, no. 1, pp. 231–239, 2005.
- [115] E. Moraes, “Segmentação De Imagens De Hematoxilina- Eosina (H & E) Utilizando Análise De Agrupamentos K-Means Segmentação De Imagens De Hematoxilina- Eosina (H & E) Utilizando Análise De Agrupamentos K-Means,” 2021.
- [116] A. H. Fischer, K. A. Jacobson, J. Rose, and R. Zeller, “Hematoxylin and eosin staining of tissue and cell sections,” *Cold Spring Harb. Protoc.*, vol. 3, no. 5, pp. 4986–4988, 2008, doi: 10.1101/pdb.prot4986.
- [117] H. E. Gruber, J. Ingram, and E. N. Hanley, “An improved staining method for intervertebral disc tissue,” *Biotech. Histochem.*, vol. 77, no. 2, pp. 81–83, 2002, doi: 10.1080/bih.77.2.81.83.

- [118] H. I. Roach, “Trans-differentiation of hypertrophic chondrocytes into cells capable of producing a mineralized bone matrix,” *Bone Miner.*, vol. 19, no. 1, pp. 1–20, 1992, doi: 10.1016/0169-6009(92)90840-A.
- [119] J. Shu, G. Qiu, and I. Mohammad, “A semi-automatic image analysis tool for biomarker detection in immunohistochemistry analysis,” *Proc. - 2013 7th Int. Conf. Image Graph. ICIG 2013*, pp. 937–942, 2013, doi: 10.1109/ICIG.2013.197.
- [120] R. Reid, “Alcian Blue pH2.5 - Acid Mucopolysaccharides,” p. 4, [Online]. Available:
<https://webpath.med.utah.edu/HISTHTML/MANUALS/ALCIAN.PDF>.
- [121] Y. Kadoya, O. Katsumata, and S. Yamashina, “Substructures of the acinar basement membrane of rat submandibular gland as shown by alcian blue staining and cryo-fixation followed by freeze-substitution,” *J. Electron Microsc. (Tokyo)*, vol. 46, no. 5, pp. 405–412, 1997, doi: 10.1093/oxfordjournals.jmicro.a023536.
- [122] A. H. Md Ali Tahir, M. A. I. M. Amin, A. Azhim, and M. Sha’ban, “Evaluation of cartilaginous extracellular matrix production in in vitro ‘cell-scaffold’ construct,” *2018 IEEE EMBS Conf. Biomed. Eng. Sci. IECBES 2018 - Proc.*, pp. 500–504, 2019, doi: 10.1109/IECBES.2018.08626712.
- [123] V. A. D. A. Lopes *et al.*, “Alterações histoquímicas das glicosaminoglicanas na cérvix uterina no final da prenhez da rata albina após ministração local de hialuronidase,” *Rev. Bras. Ginecol. e Obstet.*, vol. 30, no. 7, pp. 328–334, 2008, doi: 10.1590/S0100-72032008000700002.
- [124] “Spectragryph - optical spectroscopy software: Description.”
https://www.ffmpeg2.de/spectragryph/about_descr.html (accessed Jun. 22, 2022).
- [125] “OriginLab - Company Main Page.”
<https://www.originlab.com/index.aspx?go=COMPANY/AboutUs> (accessed Aug. 09, 2022).
- [126] “Origin: Data Analysis and Graphing Software.”
<https://www.originlab.com/index.aspx?go=PRODUCTS/Origin> (accessed Aug. 09, 2022).

- [127] I. E. P. Júnior, “Desenvolvimento De Um Oxímetro De Pulso,” 2014. https://bdm.unb.br/bitstream/10483/11331/1/2014_IraniEliasPereiraJunior.pdf (accessed Aug. 08, 2022).
- [128] J. Dos Santos Corrêa *et al.*, “Lymph node study by confocal Raman spectroscopy,” *Mundo da Saude*, vol. 41, no. 1, pp. 30–39, 2017, doi: 10.15343/0104-7809.201741013039.
- [129] M. P. Silva, A. P. C. Pereira, T. D. M. Alva, and A. A. Martin, “a Espectroscopia Raman Confocal Na Investigação Da Penetração De Produto Cosmético Despigmemente,” *Rev. Univap*, vol. 22, no. 40, p. 752, 2017, doi: 10.18066/revistaunivap.v22i40.1537.
- [130] I. Horcas, R. Fernández, J. M. Gómez-Rodríguez, J. Colchero, J. Gómez-Herrero, and A. M. Baro, “WSXM: A software for scanning probe microscopy and a tool for nanotechnology,” *Rev. Sci. Instrum.*, vol. 78, no. 1, p. 013705, 2007, doi: 10.1063/1.2432410.
- [131] K. I. Hoshino, T. Nakajima, T. Matsuda, T. Sakai, and J. P. Gong, “Network elasticity of a model hydrogel as a function of swelling ratio: From shrinking to extreme swelling states,” *Soft Matter*, vol. 14, no. 47, pp. 9693–9701, 2018, doi: 10.1039/c8sm01854e.
- [132] C. Chang, B. Duan, J. Cai, and L. Zhang, “Superabsorbent hydrogels based on cellulose for smart swelling and controllable delivery,” *Eur. Polym. J.*, vol. 46, no. 1, pp. 92–100, 2010, doi: 10.1016/j.eurpolymj.2009.04.033.
- [133] H. Park, K. Park, and D. Kim, “Preparation and swelling behavior of chitosan-based superporous hydrogels for gastric retention application,” *J. Biomed. Mater. Res. - Part A*, vol. 76, no. 1, pp. 144–150, 2006, doi: 10.1002/jbm.a.30533.
- [134] J. Ostrowska-Czubenko, M. Gierszewska, and M. Pieróg, “pH-responsive hydrogel membranes based on modified chitosan: water transport and kinetics of swelling,” *J. Polym. Res.*, vol. 22, no. 8, 2015, doi: 10.1007/s10965-015-0786-3.
- [135] X. Guo, H. Park, J. S. Temenoff, Y. Tabata, A. I. Caplan, and A. G. Mikos, “Effect of swelling ratio of injectable hydrogel composites on chondrogenic differentiation

- of encapsulated rabbit marrow mesenchymal stem cells in vitro,” *AICHE Annu. Meet. Conf. Proc.*, pp. 541–546, 2008.
- [136] W. Zhang *et al.*, “Surprising Conversion of Nanocomposite Hydrogels with High Mechanical Strength by Posttreatment: From a Low Swelling Ratio to an Ultrahigh Swelling Ratio,” 2006, doi: 10.1002/pola.
- [137] H. Ali, T. Raza Shah, H. Babar, and A. M. Ali, “Hybrid nanofluids: Techniques and challenges of stability enhancement,” *4Th Int. Conf. Adv. Mech. Eng. Istanbul 2018*, no. March 2019, pp. 60–76, 2018, [Online]. Available: <https://www.researchgate.net/publication/331629139>.
- [138] D. H. K. Ma, J. Y. Lai, H. Y. Cheng, C. C. Tsai, and L. K. Yeh, “Carbodiimide cross-linked amniotic membranes for cultivation of limbal epithelial cells,” *Biomaterials*, vol. 31, no. 25, pp. 6647–6658, 2010, doi: 10.1016/j.biomaterials.2010.05.034.
- [139] J. Costa, “Avaliação Das Propriedades Químicas, Térmicas E Citotóxicas De Filmes De Colágeno Incorporados Com Lignina Kraft Fracionada,” 2019.
- [140] M. Santos, “Isolamento e caracterização de colágeno a partir da biomassa residual de peixes (cartilagens de elasmobranchii),” vol. 549, 2017.
- [141] S. Cavalu, G. Roiu, O. Pop, D. A. P. Herdea, T. O. Costea, and C. F. Costea, “Nano-scale modifications of amniotic membrane induced by uv and antibiotic treatment: Histological, afm and ftir spectroscopy evidence,” *Materials (Basel)*, vol. 14, no. 4, pp. 1–19, 2021, doi: 10.3390/ma14040863.
- [142] A. C. V. Ballesteros *et al.*, “Bovine decellularized amniotic membrane: Extracellular matrix as scaffold for mammalian skin,” *Polymers (Basel)*, vol. 12, no. 3, 2020, doi: 10.3390/polym12030590.
- [143] R. Singh and M. P. Chacharkar, “Dried gamma-irradiated amniotic membrane as dressing in burn wound care,” *J. Tissue Viability*, vol. 20, no. 2, pp. 49–54, 2011, doi: 10.1016/j.jtv.2010.06.001.
- [144] D. C. A. Jose, “In Vitro Characterization Of Five Different Commercially Available Guided Tissue Regeneration Membranes Master Of Dental Surgery

- MEMBRANES MASTER OF DENTAL SURGERY,” 2020.
- [145] E. Tonhi and A. M. De Guzzi Plepis, “Obtenção e caracterização de blendas colágeno-quitosana,” *Quim. Nova*, vol. 25, no. 6 A, pp. 943–948, 2002.
- [146] S. M. Ali, “In vivo confocal Raman spectroscopic imaging of the human skin extracellular matrix degradation due to accumulated intrinsic and extrinsic aging,” no. September 2020, pp. 140–152, 2021, doi: 10.1111/phpp.12623.
- [147] A. Slimani and F. J. G. Cuisinier, “Confocal Raman mapping of collagen cross-link and crystallinity of human dentin – enamel junction,” vol. 22, no. 8, 2022, doi: 10.1117/1.JBO.22.8.
- [148] F. R. Formiga, “Potencial Zeta: Importante Parâmetro Na Avaliação Da Estabilização De Emulsões O/A Contendo Um Fármaco Lipofílico,” 2012.
- [149] D. K. Baby, *Rheology of hydrogels*. Elsevier Inc., 2019.
- [150] G. Stojkov, Z. Niyazov, F. Picchioni, and R. K. Bose, “Relationship between structure and rheology of hydrogels for various applications,” *Gels*, vol. 7, no. 4, 2021, doi: 10.3390/gels7040255.
- [151] A. Gilpin and Y. Yang, “Decellularization Strategies for Regenerative Medicine: From Processing Techniques to Applications,” *Biomed Res. Int.*, vol. 2017, 2017, doi: 10.1155/2017/9831534.

ANNEXES

ANNEX A

Annex A

Base Protocol

NOTE: To wash the membranes put them inside the container with the solution.

1. Wash the membranes 1 time with Phosphate buffered saline (PBS);
2. Immerse the membranes on a container with PBS + PenStrep + Fung, at 7,8 pH, for 15 min;
3. Immerse on PBS for 15 min;
4. Put the membranes on Buffer A (distilled water + 1,214 g u/l of Tris + 0,1 g of EDTA for each 100 ml of final solution, at 7,8 pH), overnight ~18h, at room temperature;
5. Wash with PBS 3 times, 15 min each time;
6. Put the membranes on Triton 1 % + DMSO, (overnight ~24h) – 37 °C (IKA 50-70);
 - a. 2700ul Triton 1 % + 300 ul DMSO
 - b. From triton 10 % dissolve 1 % in Buffer B (distilled water + 1,214 g u/l of Tris, at 7,8 pH)
7. Wash with Buffer B, 3 times, 15 min each time, at room temperature;
8. Wash with PBS 3 times, 15 min each time;
9. Wash the membranes in a solution with 20 mM Tris + 2 mM MgCl + 200 U/mL DNase, at 7,8 pH, for 3h, at 37 °C, IKA 50-70
10. Wash with PBS 3 times, 15 min each time;
11. Cell scrapper, wash 1 time with PBS, and freeze.

ANNEX B

Annex B

Table B.0.1 – Microscopy images of stained amniotic membranes.

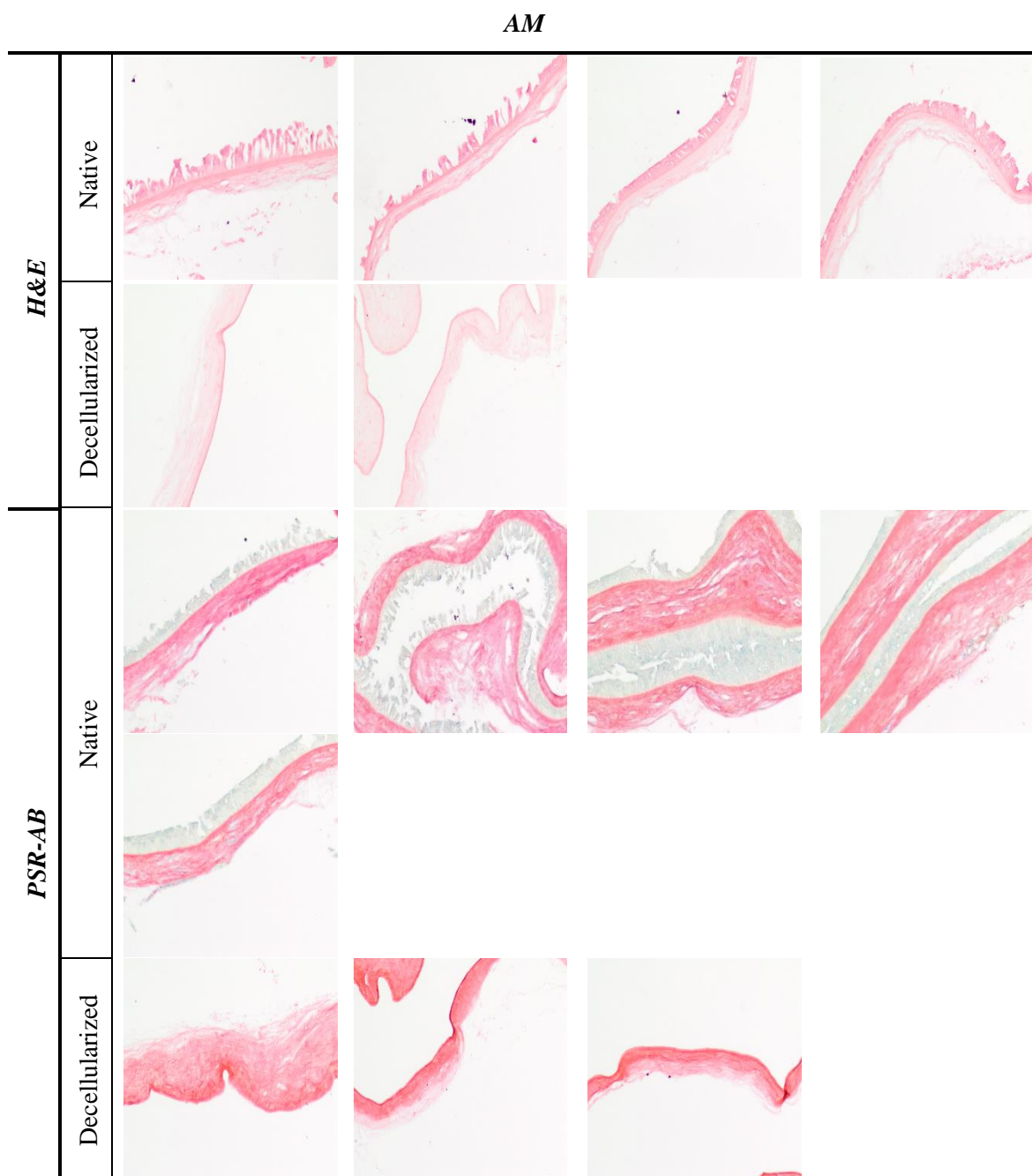


Table B.0.2 – Microscopy images of stained chorionic membrane.

CM

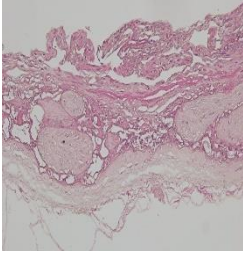
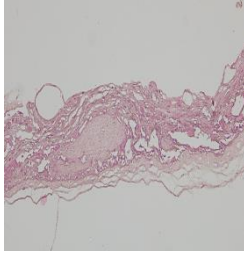
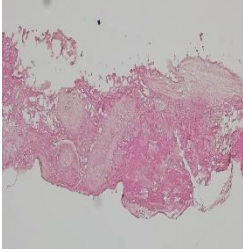
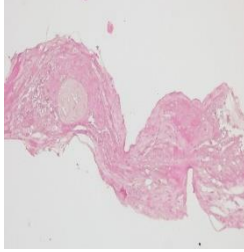
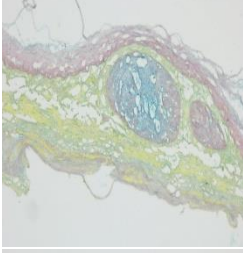
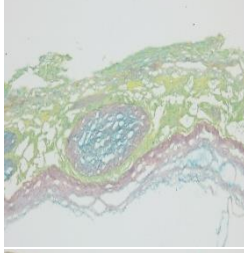
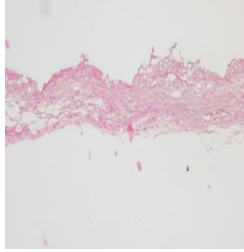
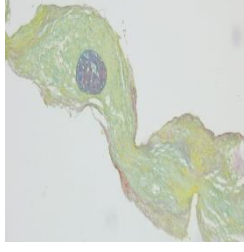
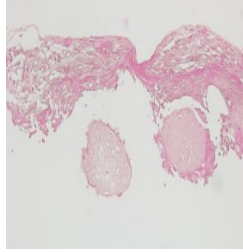
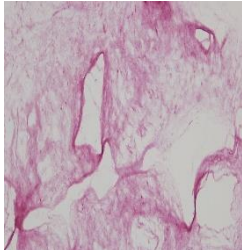
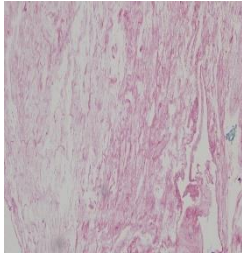
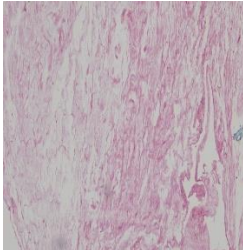
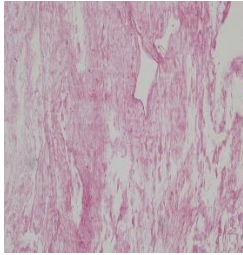
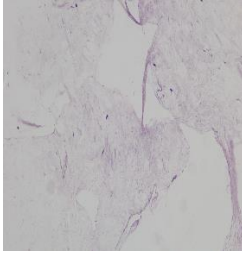
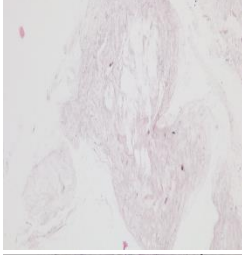
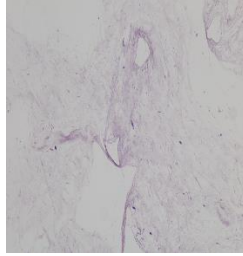
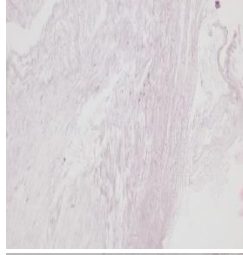
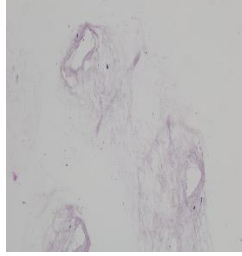

| | <i>H&E</i> | | <i>PSR-AB</i> | |
|--|---|---|--|--|
| | Native | Decellularized | Native | Decellularized |
| |  |  | | |
| |  |  |  |  |
| | |  | |  |
| | |  | | |

Table B.0.3 – Microscopy images of stained spongy layer.

SL

| | <i>H&E</i> | |
|---------------|---|---|
| | Decellularized | Native |
| <i>PSR-AB</i> |  |  |
| |  |  |
| |  |  |
| |  |  |
| |  |  |

ANNEX C

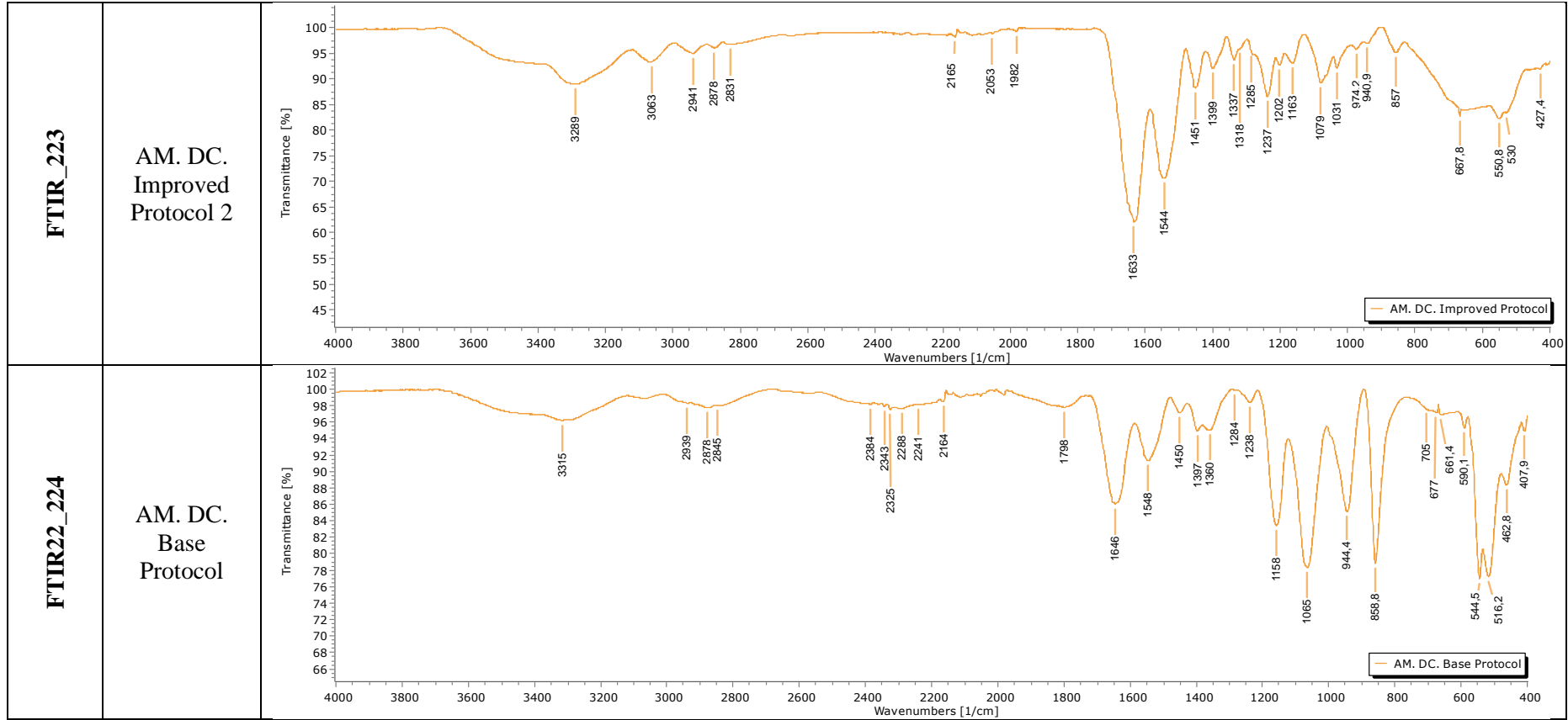
Annex C

Table C.0.1 – FTIR spectra of the fetal membranes.

| Name | Description | FTIR Plot |
|----------|-----------------------------|---|
| FTIR_221 | AM. Native | <p>FTIR spectrum for AM. Native. The plot shows Transmittance [%] on the y-axis (45 to 100) and Wavenumbers [1/cm] on the x-axis (4000 to 400). Key peaks are labeled with their wavenumbers: 3431, 3288, 3072, 2830, 2875, 1634, 1544, 1454, 1400, 1338, 1316, 1284, 1238, 1204, 1159, 1079, 1032, 974, 941, 848.3, 654.5, and 557.1.</p> |
| FTIR_222 | AM. DC. Improved Protocol 1 | <p>FTIR spectrum for AM. DC. Improved Protocol 1. The plot shows Transmittance [%] on the y-axis (65 to 100) and Wavenumbers [1/cm] on the x-axis (4000 to 400). Key peaks are labeled with their wavenumbers: 3288, 3064, 2945, 2877, 2828, 2287, 2165, 2114, 1982, 1629, 1543, 1450, 1399, 1338, 1318, 1285, 1238, 1210, 1168, 1080, 1037, 975.5, 944, 856.4, 668.2, and 547.5.</p> |

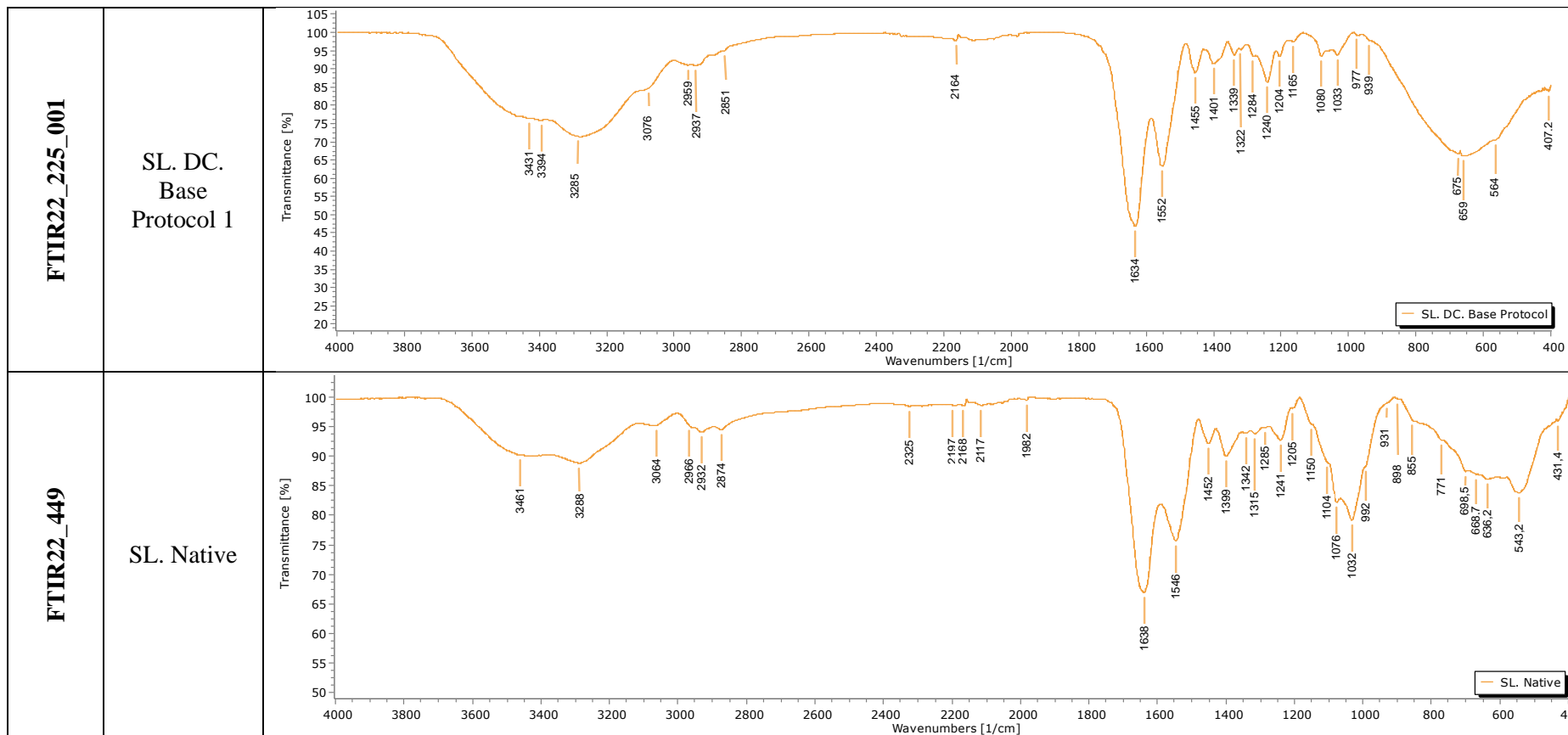
Cont.

Cont...



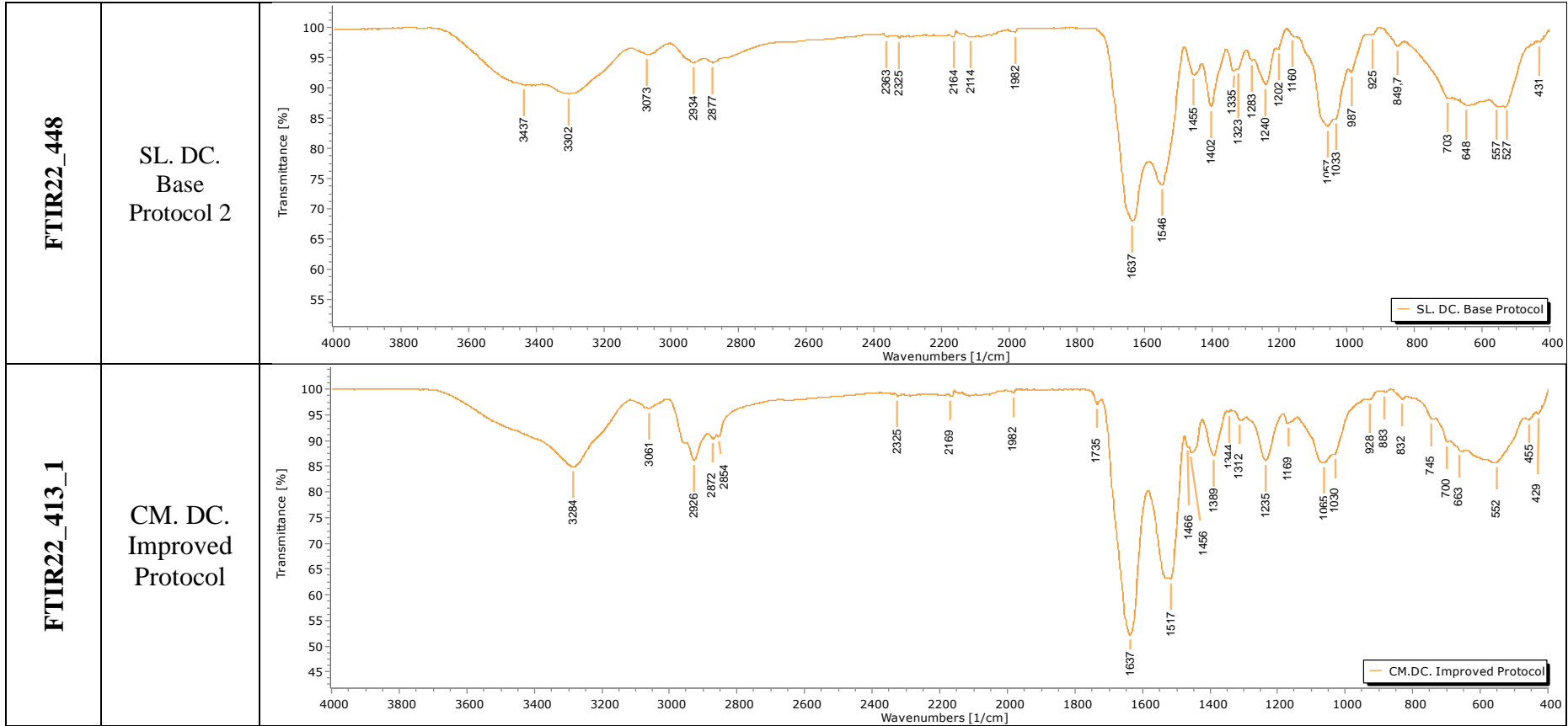
Cont.

Cont...



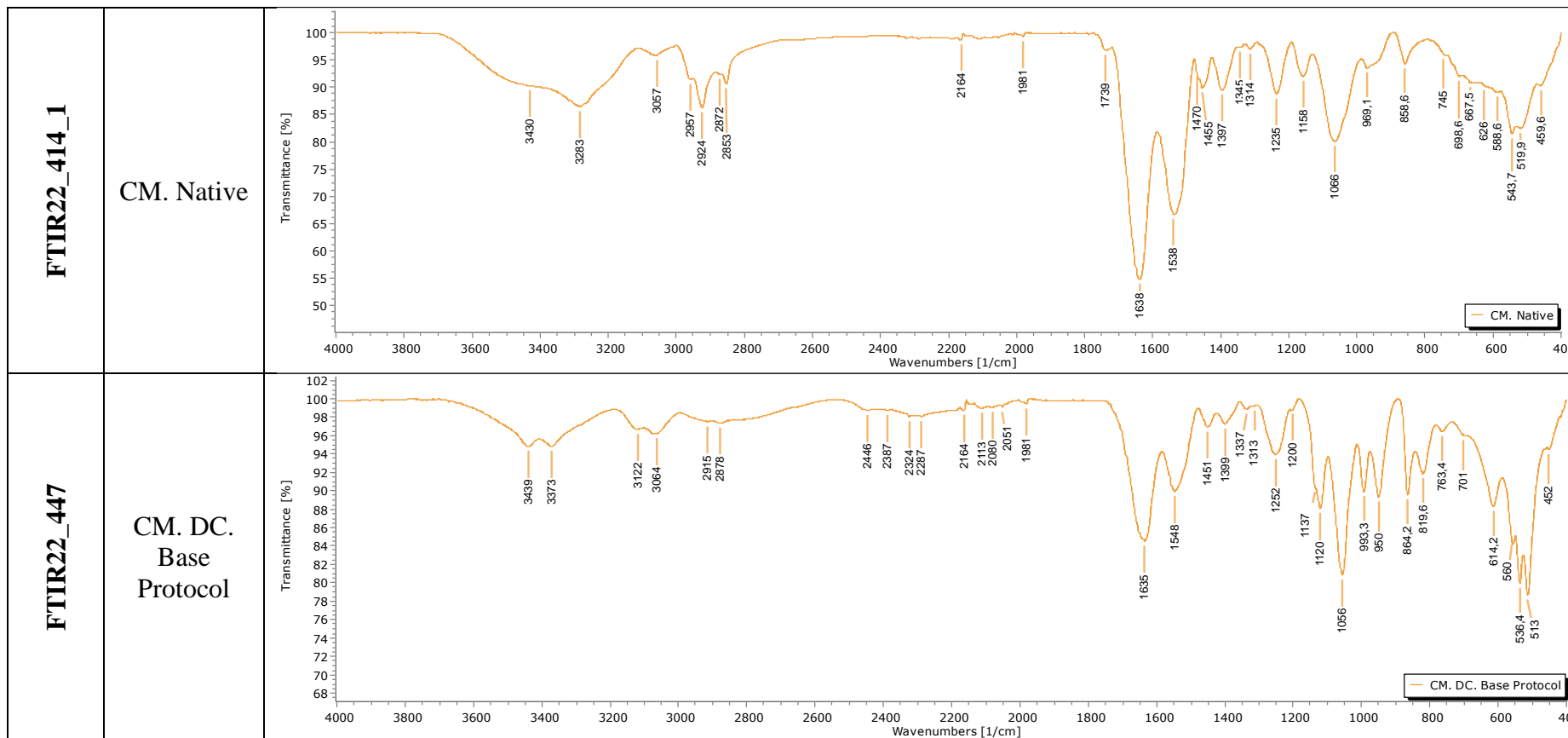
Cont.

Cont...



Cont.

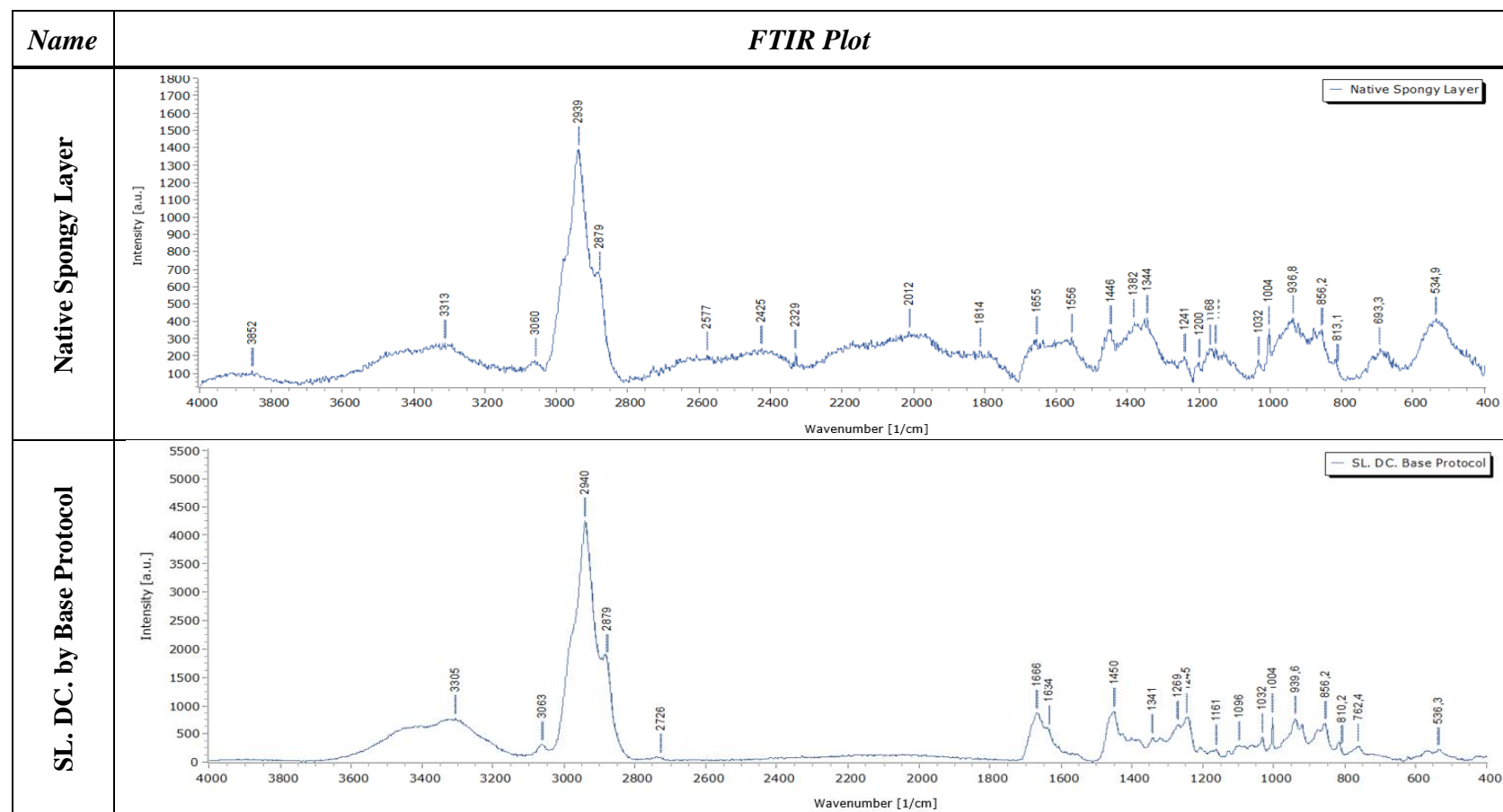
Cont...



ANNEX D

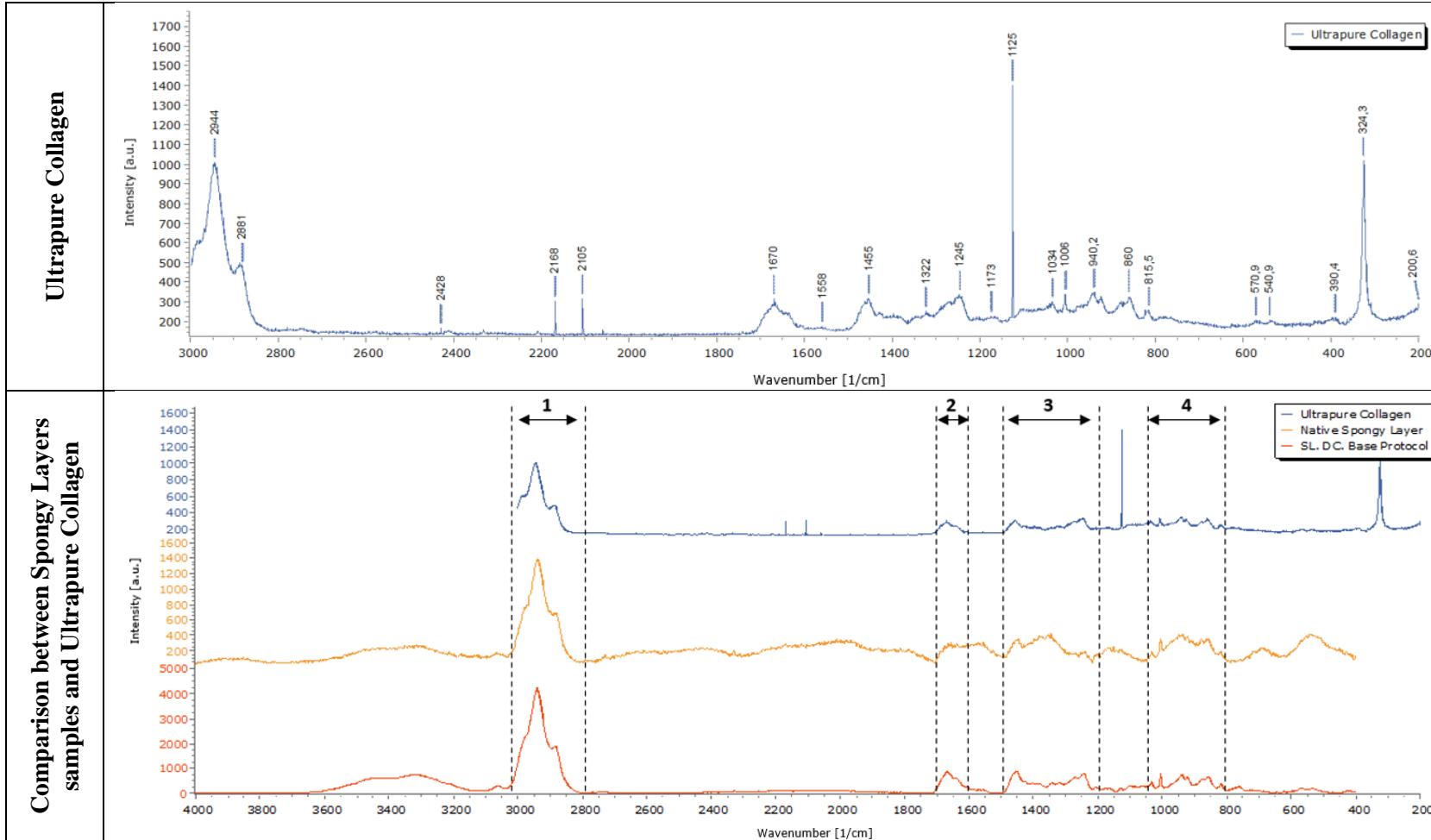
Annex D

Table D.0.1 – Confocal Raman spectra of native and decellularized spongy layer.



Cont.

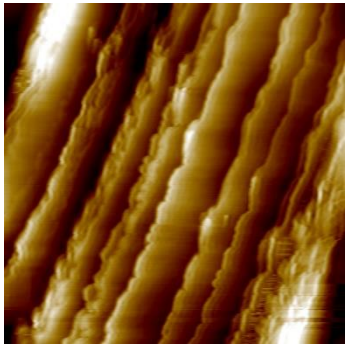
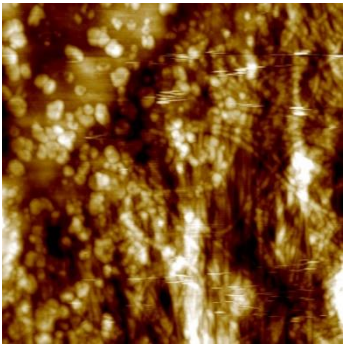
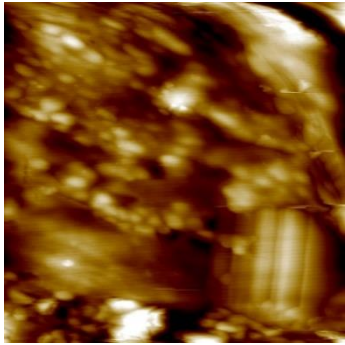
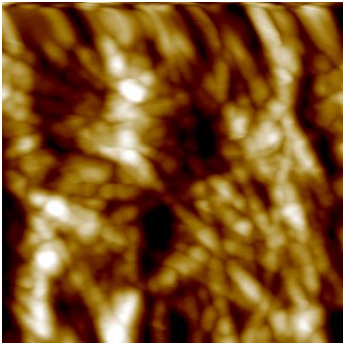
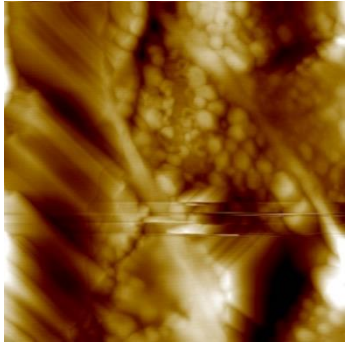
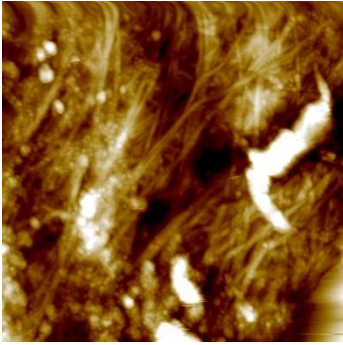
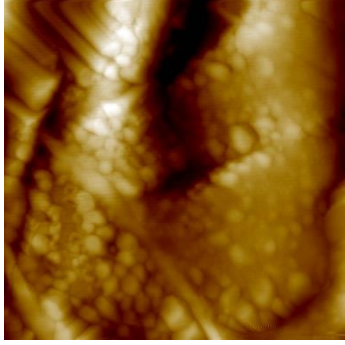
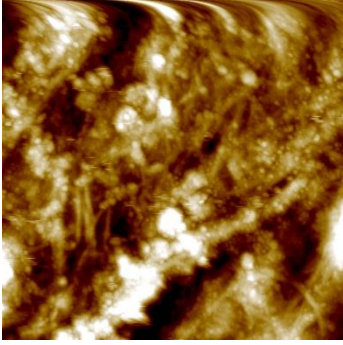
Cont...



ANNEX E

Annex E

Table E.0.1 – AFM images of Spongy Layer topography.

| <i>Name</i> | <i>Native Spongy Layer</i> | <i>Name</i> | <i>Decellularized Spongy Layer by Base Protocol</i> |
|----------------|---|----------------------------|--|
| MVS22_012_A_R1 |  | MVS22_013_A_R1 |  |
| MVS22_012_A_R2 |  | MVS22_013_A_R2_zoo m R1 |  |
| MVS22_012_A_R3 |  | MVS22_013_A_R3 |  |
| MVS22_012_A_R4 |  | MVS22_013_A_R4 |  |